UNIVERSITY OF OKLAHOMA

GRADUATE COLLEGE

MESOCYCLONE AND MICROPHYSICAL EVOLUTION IN SIMULATED SUPERCELL STORMS WITH VARYING WIND AND MOISTURE PROFILES

A DISSERTATION

SUBMITTED TO THE GRADUATE FACULTY

in partial fulfillment of the requirements for the

Degree of

DOCTOR OF PHILOSOPHY

By

MATTHEW SCOTT VAN DEN BROEKE
Norman, Oklahoma
2011

MESOCYCLONE AND MICROPHYSICAL EVOLUTION IN SIMULATED SUPERCELL STORMS WITH VARYING WIND AND MOISTURE PROFILES

A DISSERTATION APPROVED FOR THE
SCHOOL OF METEOROLOGY

BY

Dr. Jerry Straka, Chair

Dr. Michael Biggerstaff

Dr. Erik Rasmussen

Dr. Mark Yeary

Dr. Guifu Zhang

Acknowledgements

Many have contributed to this research in countless ways over the years, whether by providing direction, offering suggestions, or giving encouragement, and I wish to sincerely thank all who have been supportive of me and this project.

Thanks to my Ph.D. committee, and especially to my advisor, Dr. Jerry Straka. He has supported this work throughout, and most importantly, has helped me mature as a scientist by providing excellent feedback on my work and ideas, and through his tireless effort providing direction to my oft-wandering research focus. I have much appreciated his allowing me to teach while working on the Ph.D., and to attend and present at a conference. In many challenges during the research process, Dr. Straka has helped me along and made sure I had the tools to succeed, even while leaving me much independence to seek solutions. To the others on my committee I am also grateful—to Dr. Erik Rasmussen for his probing questions and helpful criticisms, and for many comments on my writing; to Dr. Michael Biggerstaff for my introduction to Cloud Physics at the graduate level and helpful discussions about microphysics; to Dr. Guifu Zhang for his excellent radar polarimetry course and our discussions of microphysical properties and processes in storms; and to Dr. Mark Yeary, my external member, for his interest in my progress toward the degree and my growth as a scientist.

Several other scientists have also provided excellent feedback in the process of preparing my research results. My wife Cynthia, also a meteorologist, often patiently listened to my ideas and reviewed my presentations, providing excellent insight into possible reasons behind my research findings and vastly improving my presentations. Dr. Kathy Kanak at the University of Oklahoma provided helpful feedback on several of my simulations with varying wind profiles, and was supportive along the way. Dr. Matthew Gilmore at the University of Illinois discussed the possible importance of warm rain in supercell evolution. Dr. Adam Houston at the University of Nebraska provided some excellent questions for me to think about related to my results, and pointed out a few additional processes for me to consider. Les Lemon at the Warning Decision Training Branch provided helpful conversation about supercell microphysics related to radar observations. Matthew Kumjian, working on his Ph.D. at OU, has also provided helpful discussion about radar signatures in supercells and what they might mean microphysically.

Sincere thanks to the Oklahoma Supercomputing Center for Education and Research (OSCER), and especially to Dr. Henry Neeman, for providing support while I was completing many large simulations. Thanks for their patience while I reduced the space I was taking up on their system, and for helping me work through related difficulties. Also, thanks to Dr. Mark Laufersweiler in the School of Meteorology for his computing support.

I must acknowledge Drs. Bart Wolf and Teresa Bals-Elsholz at Valparaiso University, where I first studied meteorology, for their enthusiasm and encouragement. VU provided an excellent environment for learning to appreciate the atmosphere, and also allowed freedom to learn about topics of personal interest. It was there that my love of severe convection was fostered, and there that some personal curiosities explored in this dissertation first arose.

My graduate studies at OU were funded from several sources. Thanks to National Science Foundation grants ATM-0733539 and ATM-1036237, which funded

my time as a Research Assistant. The American Meteorological Society funded the first year of my graduate studies with a graduate fellowship—I am thankful for this support, because it allowed me to choose a project of personal interest and ultimately steered me toward the interests which would become this dissertation. Finally, the University of Oklahoma provided funding for several semesters as a Teaching Assistant. Thanks to OU for allowing me this time teaching—it was one of the most rewarding aspects of my graduate experience, and has directed me toward what I hope to be a lifelong interest in sharing the amazing atmosphere with others. Also, I thank all the students I have had the opportunity to teach at OU, and have appreciated their feedback as I have sought to become a better instructor.

As important as anything thus far mentioned, I gratefully acknowledge the enduring love and support of my family. My wife Cynthia, in addition to often talking through my ideas and findings, patiently put up with me frequently being busy with research-related tasks at late hours and on weekends. Her support has been essential to my success in this undertaking, and I thank her for her dedicated love. My parents, through the years, have always been incredibly supportive, have provided me with an excellent education along the way, and have encouraged me to pursue my interests in college. Their willingness to introduce me to the wonders of the natural world at a young age is, to a large extent, why I have followed these interests and ultimately undertaken research in atmospheric science. My hope is that their dedication has been fruitful, and that this and future research will serve to increase our understanding of atmospheric processes in a way beneficial to society.

Table of Contents

List of Tables

List of Figures

Abstract

As a high-impact convective mode, supercell thunderstorms have frequently been studied observationally and numerically. Two areas of study have focused on understanding mesocyclone evolution given a varying environmental wind profile, and learning about microphysical distributions within supercells. In the research presented here, simulations are run over a broad parameter space of wind profiles, and with a smaller number of profiles representative of environmental drying at mid and upper levels. Mesocyclone evolution is compared across the parameter space of wind profiles, and between simulations with liquid and ice microphysics. Effects of the wind profile and moisture variations are explored on microphysical distributions. Subsequently, possible effects of these microphysical variations on supercell evolution are considered.

When using detailed ice microphysics with this particular choice of thermodynamic profile, mesocyclone evolution is shown to be more frequently non-occluding cyclic with no steady non-cycling storms. Storms with detailed ice microphysics are shown to have warmer cold pools, and to more rapidly concentrate vertical vorticity at low levels. The single feature found to most influence low-level mesocyclone structure was an RFD westerly surge proceeding from the echo appendage and moving eastward into the updraft region. This westerly surge often produced a new or strengthened updraft pulse, often caused a cycling process to ensue, and was the southern limit of the primary near-surface vertical vorticity maximum. Quantity and spatial distribution of warm rain and hail from frozen drops may affect downdraft temperature and thus strength of this RFD surge. Associations are explored between maximum warm rain mixing ratio and variables related to RFD intensity and near-

surface vertical vorticity. Mid- and upper-level drying reduced content of small ice particles and warm rain, while increasing content of hail from frozen drops. Bursts of warm rain and hail from frozen drops were often associated with increasing near-surface vertical vorticity, apparently related to an intensified RFD westerly surge.

1. Introduction and Goals of this Study

Supercell thunderstorms represent one of the most significant convective modes, producing many hazards ranging from flooding rainfall and large hail to severe straight-line wind and tornadoes. Many observational and modeling studies have thus sought to understand these storms, with goals of providing accurate warnings to the public and determining in advance what storm evolution may be expected for a given environment. Recent modeling studies are beginning to delve into important questions about controls on supercell evolution, especially microphysical distributions and related sensitivities.

Most supercell modeling studies have historically used liquid microphysics. A recent study showed significant differences in updraft strength, surface precipitation outcome, and cold pool strength in simulations identical except for choice of microphysics (Gilmore et al. 2004b). Ice-inclusive microphysics produced stronger updrafts due to greater latent heat release. As expected from past studies (e.g. Srivastava 1987), cold pool strength was also greater, which may have nontrivial effects on mesocyclone longevity. These differences in simulated storm evolution given choice of microphysics suggest a need for careful comparison with observations, and for great caution when interpreting any simulation results. One important goal of this study will be to show differences in storm evolution and microphysical distributions in simulations identical except for choice of microphysics, across a broad spectrum of wind profiles.

Microphysical distributions in supercell storms are poorly known; this study seeks to shed light on this problem from a modeling perspective. Distributions of liquid and ice hydrometeors will be explored in supercell storms simulated using a variety of wind profiles, and speculation will be presented as to why variation exists. In particular, the distributions of hail, graupel, and warm rain will be examined to see what effects these hydrometeors may have on strength of the near-surface cold pool and the magnitude of the rear-flank downdraft (RFD) westerly component. Given differences, possible connections will be suggested between low-level mesocyclone evolution and microphysical distributions. Storm ability to concentrate vertical vorticity near the surface will also be examined, and microphysical associations sought. Thus, this work represents an attempt to link microphysical distributions in supercells with their evolution on large and small scales, and to link the environmental wind profile to microphysical variations. As such, this work is an important step toward understanding supercell microphysics, and serves as a baseline study with which future modeling and observational studies may be compared.

A number of observational studies have previously examined the effects of varying environmental moisture on deep convection. These studies typically focus on low-level moisture, often in the lowest km. In this dissertation, a modeling sensitivity study will be presented exploring the effects of mid- and upper-level drying on simulated supercell microphysics and evolution, an area about which little has been written. Specifically, the spatial and temporal distributions of seven hydrometeor species are compared in the storms simulated using a control (moist) profile and in simulations with varying degrees of drying at mid and upper levels. Comparisons will also be made between evolution of the mesocyclone and low-level vertical vorticity field given drying. Given associations between the moisture profile and microphysical distributions, insight may be gained as to why certain environments seem to produce particular storm evolution and structure.

Chapter 2 provides the theoretical framework and previous research background for this study. External data used is discussed in Chapter 3. Terminology as used through this dissertation is introduced in Chapter 4, along with an overview of the methodology. Results are introduced beginning in Chapter 5, where mesocyclone evolution is compared between liquid and ice simulations, and several characteristics of mesocyclone evolution are examined. In Chapter 6, microphysical variations are discussed across the parameter space of wind profiles, and associations are presented between the microphysical variables and low-level storm evolution. The effects of drying at mid and upper levels are explored in Chapter 7, with a focus on microphysical variables and subsequent variability in low-level storm evolution.

2. Background

Much prior research has contributed significantly to this dissertation—it is a project which requires and extends the work of many scientists. In this section, previous observational and modeling studies will be discussed, and their relationship to the current study briefly noted.

a. Mesocyclone Cycling: Observational and Modeling Studies

The environmental wind profile is of paramount importance in determining mode of storm development. One group of hodographs, typically those with significant cyclonic curvature, produces the supercell mode of storms. Supercells can also be produced in an environment with a straight-line hodograph (Weisman and Klemp 1982). These storms contain a rotating, often long-lived updraft called the mesocyclone, and are associated with a large percentage of severe weather reports. Rasmussen and Blanchard (2002) explored the parameter space for non-supercell, supercell non-tornadic, and tornadic supercell storms. They concluded that several wind variables were important in determining storm outcome. Supercell storms were distinguished reasonably well from non-supercell storms by the magnitude of boundary layer to 6 km wind shear, though this parameter had little ability to distinguish between tornadic and non-tornadic supercells. Thus, development of a mesocyclone seems partially reliant on the presence of moderate to strong vertical wind shear from the surface to midlevels. Wind variables with some ability to distinguish tornadic and non-tornadic mesocyclones, in their study, were storm-relative helicity (related to hodograph curvature), and more weakly, mean shear over the lowest 4 km and storm-relative upper-tropospheric wind speed (Rasmussen and Blanchard 1998). This suggests that the development of intense low-level vortices is more closely related to near-ground shear and the shape of the vertical wind profile. Dowell and Bluestein (2002a) note that a supercell may modify the wind profile at low levels and midlevels within approximately 30 km, though such environmental modification is not the focus of this study. Rather, effects of a differing initial environmental wind profile are sought on the behavior of a simulated mesocyclone and the support of intense low-level vortices.

Rotational properties of the mesocyclone have been found, in prior modeling work, to be strongly related to the storm-relative environmental helicity (SREH) and therefore to the shape of the wind profile relative to storm motion (Droegemeier et al. 1993). In another study, updrafts were found to be more intense and last longer in highly-sheared environments, because of an increased perturbation pressure gradient force (Brooks and Wilhelmson 1993). These studies point to a fundamental control on mesocyclone evolution rooted in the environmental wind profile.

Supercell mesocyclones often change in repeatable, cyclic ways through their existence. Observational studies have shown real storms which exhibit varying cyclic behavior (e.g. Dowell and Bluestein 2002b). Cyclic behavior of the supercell mesocyclone has been studied numerically. Adlerman et al. (1999) present a five-stage mesocyclone lifecycle, which was also largely found to well-describe the simulated storms described herein. In their model, the mesocyclone first reaches low levels (below 500 m), then the RFD surges eastward and initiates a second updraft pulse to the east of the initial updraft. Next, an occlusion downdraft rapidly forms and merges with the

RFD, supporting a third updraft pulse and substantially increasing low-level mesocyclone vorticity. The RFD surges around the mesocyclone, cutting off its supply of unstable inflow and promoting weakening. The downshear updraft pulse then develops further and becomes the dominant mesocyclone, eventually initiating new near-ground development of mesocyclone-strength vorticity (Adlerman et al. 1999).

From this initial model, subsequent studies have looked further at mesocyclone sensitivity to model setup and environmental modifications. Adlerman and Droegemeier (2002) found that the cycling behavior of a simulated supercell depended on model horizontal and vertical resolution, and on parameterizations of diffusion and surface friction. For a vertical grid spacing of 250 m, fairly uniform cycling behavior was observed. This grid spacing is consistent with the simulations discussed in this dissertation.

In a series of simulations, Adlerman and Droegemeier (2005) examined the effects of varying wind profiles on the behavior of a simulated mesocyclone given a constant thermodynamic environment. Mesocyclones were found to be non-cyclic, cyclic but non-occluding, or cyclic and occluding. Hodograph shapes chosen ranged from straight-line to full circle, with a variety of half-, quarter-, and three-quarter-circle shapes with a number of shear magnitudes for each. Full-circle hodographs were always found to yield non-cycling storms, while straight-line hodographs always yielded cyclic but non-occluding storms. Other hodograph shapes were found to yield different mesocyclone behaviors depending on shear magnitude (Fig. 2.1). These simulations were completed using liquid microphysics (Adlerman and Droegemeier 2005).

b. Microphysical Distributions in Supercell Storms

Microphysical distributions have been poorly studied in supercell thunderstorms. A few studies have reported such measurements obtained from aircraft. Brandes et al. (1995) sought to correlate hydrometeor distributions and polarimetric observations in a Colorado supercell. Entering the storm from the south just above the melting level, the aircraft encountered mostly graupel. A differential reflectivity (Z_{dr}) bright band was thought to be caused by graupel with a liquid coating, and increasing Z_{dr} below was attributed to melting graupel. As expected, a Z_{dr} minimum in the storm core was found to contain a high concentration of hail, and hail greater than 10 mm in diameter was limited to regions with reflectivity factor exceeding 50 dBZ. Small concentrations of large drops were located along the storm's forward flank. Liquid water content (LWC) and drop size distribution (DSD) were recorded on transects through an Oklahoma supercell (Loney et al. 2002). An updraft warm anomaly was associated with high LWC, and shedding was speculated to be a possible cause of high numbers of small drops along the western updraft periphery. Comparison of in-situ hydrometeor measurements with polarimetric radar observations showed reasonable agreement.

Polarimetric radar has also been used to study microphysical distributions in supercell storms. Though there are limitations to applying scattering theory such as the T-matrix model to the real atmosphere, reasonable agreement between expected hydrometeor species and aircraft observations yields confidence that polarimetric radar observations are a useful source of additional microphysical information. Columns of liquid drops, known as Z_{dr} columns, have been found extending above the freezing level in the updraft (e.g. Hubbert et al. 1998). Loney et al. (2002) found a column of liquid drops upwind from the updraft and attributed their presence to shedding from melting hail. Signatures consistent with melting graupel were found near the environmental melting level. Repeatable supercell polarimetric signatures were first presented in Ryzhkov et al. (2005). The Z_{dr} column was found and again attributed to large liquid drops lofted in the updraft. Low correlation coefficient in the updraft was attributed to lofted debris. Finally, a band of high Z_{dr} values was repeatably found along the supercell forward flank and attributed to large drops. In a later study this band was named the Z_{dr} arc (Kumjian and Ryzhkov 2008), and other repeatable features including rings of Z_{dr} and correlation coefficient around the updraft region were described. Repeatable polarimetric features of Southern Plains tornadic supercells were presented in Van Den Broeke et al. (2008) along with preliminary speculation about microphysical meanings of the signatures. Frame et al. (2009) discussed the frequent ‘winged’ appearance of many supercells, and concluded it was present for microphysical rather than dynamical reasons.

Other supercell observational studies provide insight into their microphysics. General rain and hail distributions in several classes of supercells were presented by Moller et al. (1994). Browning (1965) observed a fall of large hail just prior to tornadogenesis in two right-moving Oklahoma storms, likely supercells, and found evidence of a stronger turn to the right when large hailfall was occurring. In Browning’s study, however, there was no speculation about a possible link between hailfall and tornadogenesis. In a small sample of tornadic Southern Plains supercells, a region of polarimetrically-inferred hailfall was found most commonly around the time of tornadogenesis (Van Den Broeke et al. 2008). Given a larger sample of tornadic and non-tornadic warm-season Southern Plains supercells, another study found that the hail characteristics of a supercell remain relatively constant from the pre-tornado to the tornado time (Kumjian and Ryzhkov 2008). This study did, however, note a more persistent, less-cyclic polarimetric hail signature in non-tornadic storms than in tornadic storms. This difference may indicate some microphysical control on supercell downdraft evolution, which in turn may vary with the environment. Rasmussen et al. (2006) and Kennedy et al. (2007) discuss the descending reflectivity core (DRC), a small region of descending precipitation in the RFD region. Amount of evaporative cooling in this region, determined by the quantity and type of evaporating hydrometeors, may have important implications for downdraft strength and thus on mesocyclone evolution. Higher rain rates have generally been associated with stronger downdrafts (e.g. Kamburova and Ludlam 1966), but the phase of hydrometeors is also an essential consideration (e.g. Srivastava 1987). In a study of forward-flank downdraft (FFD) characteristics, melting of graupel was speculated to be more important in determining outflow temperature than the amount of evaporative cooling (Shabbott and Markowski 2006), suggesting the importance of understanding supercell microphysics if modeling attempts are to produce reasonable results for correct reasons.

c. Microphysical Controls on Supercell Evolution

Microphysical processes are also thought to play an important role in supercell evolution, including mesocyclone behavior, since the energy budget is affected via latent heating effects. Observational studies have pointed to associations between microphysical distributions and supercell evolution. Mesocyclone sustenance may be aided by generation of baroclinic vorticity along the FFD. The degree of baroclinicity present is related to the temperature difference between environmental inflow and rain-cooled outflow, and this difference is partially controlled by microphysical processes in the downdraft. The FFD was found to average slightly warmer in tornadic storms, with less baroclinic vorticity generation (Shabbott and Markowski 2006). Convergence along the RFD likely plays an important role in concentrating low-level vorticity under the updraft, and thus in tornadogenesis. RFD characteristics seem important in determining whether or not a tornado forms (e.g. Markowski et al. 2002), and to a large degree, these characteristics may be determined by the microphysics involved in its development. Thus, the choice of a liquid-only vs. ice microphysical parameterization in a supercell simulation may be critical in determining behavior of the simulated storm. The hail distribution also appears to be critical in determining mesocyclone behavior. Polarimetric observations of supercell storms have indicated a more persistent, less cyclic polarimetric hail signature in non-tornadic storms than in tornadic storms (Kumjian and Ryzhkov 2008). This difference may indicate a microphysical control on supercell downdraft evolution, which in turn should affect updraft structure. Past modeling attempts have shown inclusion of the ice phase to produce storms with colder area-averaged outflow, due to more melting and evaporative cooling (Gilmore et al. 2004b).

Several modeling studies have examined sensitivities of supercell evolution to the microphysical parameterizations chosen. Cold pools may be stronger when the ice phase is included, due to melting of small ice particles (e.g. Srivastava 1987). Even the hailstone distribution chosen may affect storm evolution as much as whether or not a given storm has ice or not (van den Heever and Cotton 2004). Simulated storms in which ice microphysics was used were found to more rapidly produce a first cycle. Inclusion of ice microphysics was found to increase updraft strength by 10% due to additional latent heat release. Quicker cycling occurred initially, but the entire cycling process was not sped up (Adlerman and Droegemeier 2002). Overall, modeling has indicated that supercells which form in a strongly-sheared environment seem less sensitive to changes in hodograph shape and model resolution than storms simulated in less-sheared environments (Gilmore et al. 2004a).

A few past modeling studies have explored the role of microphysics in supercell storms. Conway and Zrnić (1993) calculated hailstone trajectories. They found hailstone sources to include melted hydrometeors falling from the anvil and recirculated into the updraft, and growth within the updraft by freezing. More precipitation is generated given higher environmental shear, but is spread over a larger area (Gilmore et al. 2004b).

Comparisons have been made between supercells modeled with liquid versus ice-inclusive microphysics (Gilmore et al. 2004a). When the ice phase was included, the stratiform precipitation region was larger, and there was 40% greater surface precipitation accumulation. These effects were attributed to stronger updrafts and the ability of ice-phase particles to fall out farther from the updraft. Greater latent heat release was present when the ice phase was included, leading to stronger updrafts and greater updraft volume. The cold pool also averaged larger and stronger due to more melting, sublimation, and evaporative cooling (Gilmore et al. 2004a).

Van den Heever and Cotton (2004) examined the effects of varying hail distributions on supercell evolution by varying mean hail diameter between 3 mm and 1 cm. In storms with the largest mean hail diameter, the right-moving updraft was more steady and persistent. As mean hail diameter was reduced, downdrafts became stronger due to more melting and evaporational cooling, and less ice reached the surface. Cold pool depth increased, and cold pools propagated more rapidly. This more rapid motion was found to initially strengthen the storm by promoting a new updraft pulse, but the cold pool soon outran the updraft and the storm weakened. When hail of large mean diameter was present, the cold pool and updraft remained in close proximity, promoting storm longevity. There was greater vorticity generation along the FFD in storms with smaller average hail size, since cold pools were stronger in these storms. Storm structure was found to most closely resemble a classic supercell when mean hail diameter was small, and to resemble a high-precipitation (HP) supercell when mean hail diameter was large (van den Heever and Cotton 2004). Differences between these simulated storms were as great as between storms with and without hail. A study with varying graupel distribution found similar results: as mean graupel diameter became smaller, storms had greater updraft volume and colder area-averaged outflow (Gilmore et al. 2004b).

d. Effects of Varying Moisture on Supercell Evolution

Supercell storms have been shown to affect the moisture distribution of their nearby environment. The well-studied Del City, Oklahoma, tornadic supercell (1977), for instance, was shown to increase the low-level mixing ratio by 2 g kg^{-1}, producing a

0.4-km (40 mb) lowering of the lifted condensation level (LCL) height (Johnson et al. 1987). This effect on the nearby environment could in turn affect tornadogenesis potential, since lower LCLs have been associated with increased tornado likelihood (e.g. Rasmussen and Blanchard 1998). A modified near-storm environment might also affect the storm's microphysics, and thus indirectly modify the cold pool strength and subsequent mesocyclone evolution. One goal of this work will be to study how cold pool strength and mesocyclone evolution differ with a variable environmental moisture profile, with a focus on microphysical differences. One process not considered in depth is the advection of hydrometeors from one storm to another (Browning 1965). This process undoubtedly affects supercell microphysics, especially when the environmental wind shear is strong and particles are readily advected between storms.

Several observational studies have elucidated the role of environmental moisture in supercell structure and evolution. Many of these studies have focused on moisture in the lowest km, generally below cloud base. Long-lived supercells have been found to move parallel to an axis of enhanced low-level moisture (Bunkers et al. 2006); the moister environment can prolong the life of the supercell even when wind shear is not especially favorable. Greater moisture in the lowest km, manifest as a lower LCL height, has been shown to discriminate fairly well between nontornadic and tornadic supercells (e.g. Rasmussen and Blanchard 1998, Markowski et al. 2002, Thompson et al. 2003). Lower LCL heights may favor tornadogenesis by reducing the amount of stretching required for a vortex to reach from cloud base to the ground, or more importantly, may signal a moister local environment favoring weaker hydrometeor evaporation and thus warmer downdrafts (e.g. as suggested in Markowski et al. 2002).

Finally, an observational study of High Plains storms showed that moister air below cloud base resulted in less cooling due to evaporation, leading to less-intense downdrafts (Knupp 1988). Given the vital importance of downdraft strength on supercell evolution, changes in environmental moisture are likely to have significant repercussions.

Fewer observational studies have looked at the role of midlevel moisture in the supercell environment. Pre-existing midlevel moisture has not been found to discriminate between days with and without deep convection (Weckwerth 2000). This result makes sense, since initiation of supercell or other deep convection requires parcels to reach their level of free convection (LFC), so some lifting mechanism must also be present. In the context of the research presented herein, deep convection is supposed to already exist, having been forced by a warm bubble in low levels. Once convection has initiated, then, the results of environmental moisture variations on convective evolution are explored.

Type of convective storm favored in a given environment may be sensitive to moisture characteristics. In an early study of low-precipitation (LP) versus classic supercell storms, the depth of the low-level moist layer was found to average the same for each class of storms. Quantity of moisture within this moist layer, however, was quite different: in environments producing LP storms, mean water vapor mixing ratio averaged 1.6 g kg^{-1} lower (Bluestein and Parks 1983). Precipitable water and mean humidity in this layer were also less by a statistically significant amount. This association makes sense—differing amounts of condensation should affect the storm's energy budget, with probable microphysical effects as well. Some microphysical effects of environmental drying are presented here.

In a study of many tornadic and nontornadic storms, development of the RFD was explored. Tornadic storms were found to contain warmer RFDs on average, while nontornadic RFDs tended to contain cooler, more stable air (Markowski et al. 2002). This is consistent with the results of this study, which shows supercells with cooler RFDs including storms simulated with liquid-only microphysics to contain smaller average near-surface vertical vorticity values. One possible reason for this difference would be a lesser importance of dry midlevel air entrainment in tornadic storms. It is also possible that storms with a moister midlevel environment, and thus entraining moister air, might experience less cooling of the RFD, increasing tornado potential.

Few studies have specifically examined the effects of dry midlevel and upper-level air on supercell storms, though a few studies have looked at effects of dry air on downdrafts. In an idealized study, entrainment of dry environmental air was found to weaken downdrafts via decreased precipitation loading (Srivastava 1985). If moister air is present to be entrained, it is possible that downdrafts might be strengthened, but this should depend on the DSD. Increased near-surface vertical vorticity observed and simulated in moister environments, then, may be related to the presence of a stronger RFD. In a follow-up study, Srivastava (1987) found that inclusion of small ice particles led to lower average mixing ratio and relative humidity at low levels around a simulated downdraft. Thus the microphysics of a downdraft are likely to affect moisture characteristics of the surrounding environment at low levels.

An early modeling study looked at the effects on updraft longevity of environmental moisture in the lowest 2.8 km. As low-level moisture increases, updrafts were found able to persist under increasing vertical wind shear (Schlesinger 1973). This modeling result matches observations of storms which often struggle on dry days, and may be related to the increased CAPE of environments with increasing low-level moisture. Tropical convective systems have been found to produce less precipitation when the mid and upper levels are dry (Ridout 2002), though the applicability of these results to midlatitude supercell convection is uncertain. Supercell characteristics, including maximum updraft velocity and outflow temperature, have been found to vary substantially when the LCL and LFC height is varied (McCaul and Cohen 2002).

In a modeling study with liquid-only microphysics, the effects of midtropospheric drying on supercell evolution were explored (Gilmore and Wicker 1998). Generally, storms in environments with greater midlevel drying were found to contain stronger outflow. In moderate-shear environments this strong outflow tended to lessen unstable inflow and ultimately weaken the updraft, though if strong shear was present, surging outflow was less likely to weaken the updraft. In their simulations, Gilmore and Wicker found storms tending to split about 40 min from initialization. After this initial split, updrafts were consistently weaker in storms with a drier midlevel environment. From 50 – 90 min, low-level mesocyclones were stronger in storms with midlevel drying. This was attributed to greater convergence of vertical vorticity along the surging gust front in these simulations, and to increased baroclinic generation along these storms' stronger forward-flank temperature gradients.

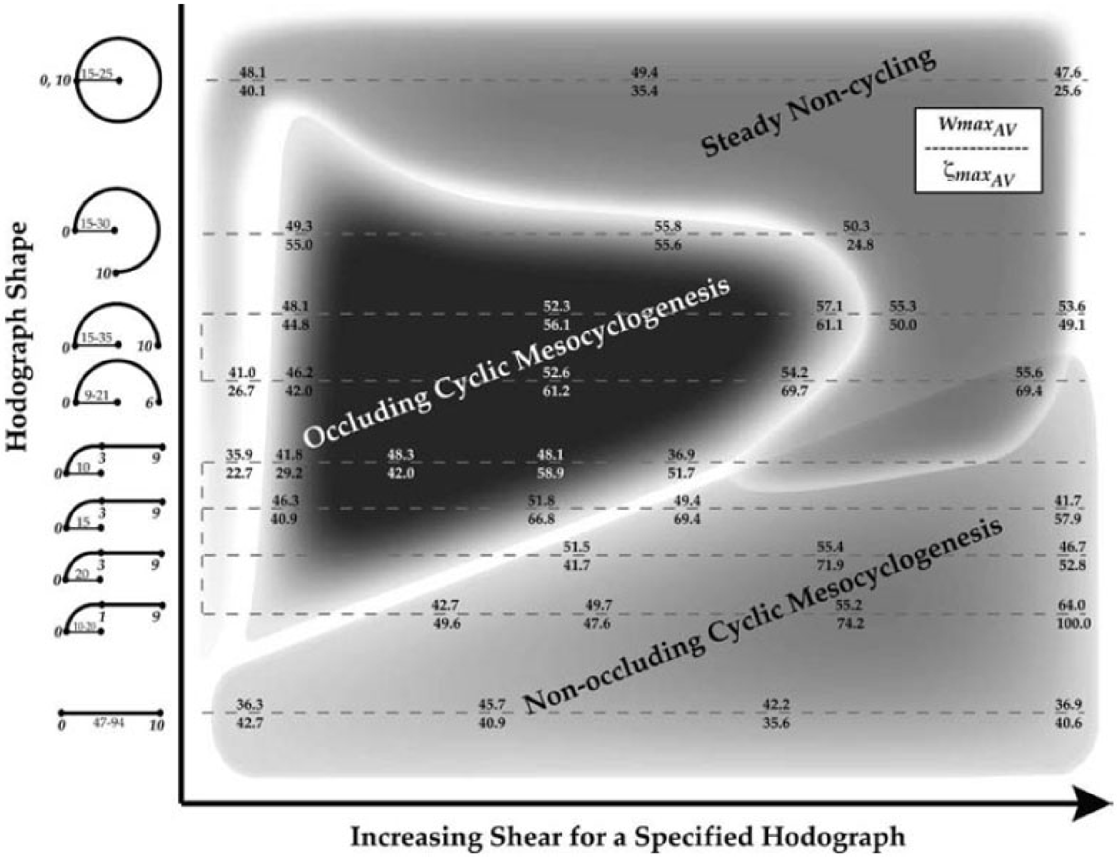

Figure 2.1: Adlerman and Droegemeier's wind profile parameter space (2005). Hodograph shape is depicted on the left side of the figure. Shading represents the three types of mesocyclone evolution seen in their study and this study. Each set of numbers represents one wind profile used in Adlerman and Droegemeier's study. Numbers represent maximum upward motion (top) and vertical vorticity in the lowest 2 km x 10^3 (bottom). These maxima were for anywhere in the model domain, and were anytime between 3600 s and 14400 s past model initialization.

3. Data

The thermodynamic sounding used in these simulations was first presented in Weisman and Klemp (1982). It was created via a set of equations and represents a typical supercell environment, including a well-mixed boundary layer, moderate midlevel instability for a parcel ascending moist adiabatically, and a low cloud base (Fig. 3.1). Weisman and Klemp tested additional wind profiles with this thermodynamic profile, including half-circle profiles with shear magnitude ranging from 10 to 50 m s^{-1} in the lowest 5 km, with constant wind above 5 km (1984). This study used liquid-only microphysics. Numerous other modeling studies have also used this thermodynamic profile, which is known for producing a supercell which appears realistic and can give rise to intense low-level vortices.

One figure is presented which shows polarimetric radar data from the Norman, Oklahoma, dual-polarized Doppler radar (KOUN). The radar was experimental when these data were collected, and was in the process of being upgraded to operational polarimetric specifications. Background information on the experimental setup of KOUN can be found in Zrnić et al. (1999) and Doviak et al. (2002).

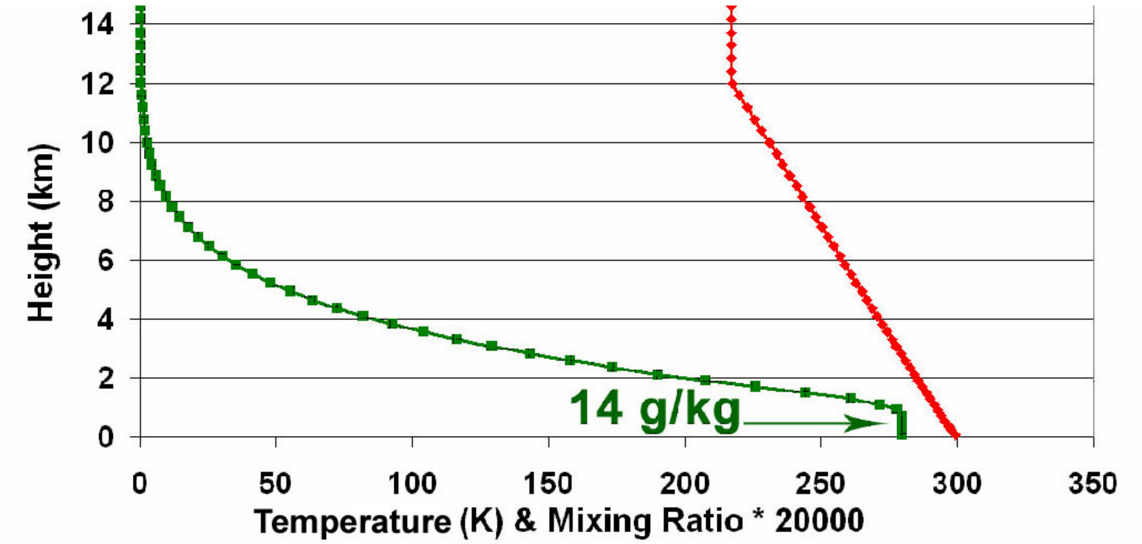

Figure 3.1: Thermodynamic profile of Weisman and Klemp (1982). Green line represents the mixing ratio in g kg^{-1} multiplied by a scaling factor of 20000, and red line represents the temperature in Kelvin.

4. Terminology and Methodology

This work was undertaken in several distinct but closely-related stages, which are described in this section. First, experiments with varying wind profiles are described, followed by experiments with mid- and upper-level drying. Key terminology as defined for the sake of this study is introduced.

a. Experiments with Varying Wind Profiles

In this study, the thermodynamic profile of Weisman and Klemp (1982), described above under Section 3, was used. The wind profile was replaced with a number of hodograph shapes and shear magnitudes. The chosen wind profiles replicate some of those used in Adlerman and Droegemeier (2005), who used the Del City composite thermodynamic profile (Klemp et al. 1981). Thus, the work presented here builds on that of Weisman and Klemp (1984) by testing additional hodographs and studying the effects of including ice microphysics, and builds on that of Adlerman and Droegemeier (2005) by testing differences in ice-inclusive simulations and extending the experiments to a different thermodynamic profile. This thermodynamic profile is characterized by greater stability than the sounding used in Adlerman and Droegemeier (2005), possibly leading to differences in cycling behavior as discussed later.

Adlerman and Droegemeier (2005) simulated supercells using 57 different hodographs ranging over the full parameter space from straight-line to full circle. A subset of 22 of these hodographs was chosen which cover the parameter space reasonably well (Table 4.1). Wind profiles near the edge of two mesocyclone cycling types in Adlerman and Droegemeier's study were favored. For each hodograph, one simulation was run with liquid-only microphysics and one simulation with ice microphysics as described below. In each simulation, mesocyclone behavior was classified as steady (non-cyclic), cyclic occluding, or cyclic non-occluding. Diagrams of mesocyclone behavior with varying shear were constructed following Adlerman and Droegemeier (2005), with the intent of seeing how repeatable the behavior was between the two models, and how the liquid and ice-phase simulations compared.

The three modes of mesocyclone cyclicality (Fig. 4.1) were defined in the same way as in Adlerman and Droegemeier (2005). These modes agreed completely with the modes observed when completing the research presented herein. Such agreement between model-produced types of mesocyclone cyclicality raised confidence in the ability of the Straka Atmospheric Model (SAM) to produce evolution similar to that seen in prior modeling studies. The three modes of mesocyclone evolution are defined as:

1) Steady (non-cycling): a westerly surge develops along the west-central updraft edge associated with an RFD. This configuration of updraft region and RFD westerly surge remains relatively constant through time once developed. Vertical vorticity of the highest magnitude at 1000 m is typically located just north of the westerly surge, with another maximum possible to its south (Fig. 4.1a). Magnitude of the RFD westerly surge may vary, though its location remains relatively constant relative to the updraft region. An example of a storm demonstrating this cycling mode, from a half-circle simulation (I1), is presented in Fig. 4.2.

2) Occluding cyclic: starting from a configuration containing an RFD westerly surge and updraft region as described above, the westerly surge continues eastward and cuts off much of the updraft's unstable inflow before diminishing. This weakening is generally associated with decreasing cyclonic curvature of the echo appendage. The region of enhanced vertical vorticity expands to cover most of the central updraft region. At some later time, a new RFD westerly surge again deforms the updraft region and vertical vorticity becomes concentrated in a narrow region to its north Fig. 4.1b). An example of a storm demonstrating this cycling mode, from a simulation with a quarter-circle turn in the lowest km (I16), is presented in Fig. 4.3.

3) Non-occluding cyclic: starting from a configuration as described under the steady mode above, the RFD westerly surge wraps northward into the updraft region but never cuts off the unstable inflow. Strongest surface vertical vorticity typically occurs just west of this feature at the edge of a very cyclonically-curved region of updraft. Eventually the RFD surge diminishes, and the updraft region develops northward toward the supercell's forward flank. Vertical vorticity has typically decreased, but begins to increase again in association with the new, stronger area of updraft to the north. Finally a new RFD surge proceeds eastward from the echo appendage, which has typically reformed northward. Strongest vertical vorticity quickly wraps around the new RFD surge. A remaining region of enhanced vertical vorticity is often present marking the past location of the RFD surge (Fig. 4.1c). An example of a storm demonstrating this cycling mode, produced

using a wind profile with a quarter-circle turn in the lowest 3 km (I21), is presented in Fig. 4.4.

The model used was the three-moment, non-hydrostatic, three-dimensional, compressible SAM with a time step of 1 s and horizontal resolution of 250 m. It has open side boundaries and free-slip upper and lower boundaries. This model has been utilized before in numerical studies of deep convective storms including supercells (Gilmore et al. 2004a, 2004b; Johnson et al. 1993), microbursts (Straka and Anderson 1993), and thunderstorm electrification (Straka and Mansell 2005). Vertical resolution stretched from 155 m near the surface to 520 m at 20 km, with a lowest level 75 m above the surface. A 3 K spheroidal warm bubble was used to initiate convection. Model output files were generated every 5 min.

Conservation of momentum, mass, and energy were assumed. Momentum conservation followed the compressible Navier-Stokes equations of motion in a rotating reference frame:

$$\begin{aligned}\frac{\partial u_i}{\partial t} &= -\frac{1}{\rho}\frac{\partial \rho u_j u_i}{\partial x_j} + \frac{u_i}{\rho}\frac{\partial \rho u_j}{\partial x_j} + \frac{1}{\rho}\frac{\partial \tau_{ij}}{\partial x_i} + \varepsilon_{ijk} u_j f \\ &\quad - \frac{1}{\rho}\frac{\partial p'}{\partial x_i} + \delta_{i3} g \left[\frac{\theta'}{\overline{\theta}} + \frac{Q_v'}{0.6078 + \overline{Q_v}} - \gamma \frac{p'}{\overline{p}} - \frac{Q_v' + \sum_m^M Q_m}{1 + \overline{Q_v}} \right]\end{aligned} \qquad 4.1$$

where u_i denotes the velocity components, g = gravitational acceleration, $\gamma = c_v/c_p$ where c_p=1004 J Kg^{-1} K^{-1} and c_v = 717J Kg^{-1} K^{-1}, and f is the Coriolis force which is a function of latitude and Earth's rotation rate. The stress tensor $\tau_{ij} = \rho K_m D_{ij}$ where ρ is the density of moist air which is a function of pressure and mixing ratio, K_m is the eddy mixing coefficient and D_{ij} is the deformation tensor. Quasi-compressible mass conservation was used. Conservation of energy was given in terms of potential temperature (θ):

$$\frac{\partial \theta}{\partial t} = -\frac{1}{\rho}\frac{\partial \rho u_i \theta}{\partial x_j} + \frac{\theta}{\rho}\frac{\partial \rho u_i}{\partial x_i} + \frac{\partial}{\partial x_i}\left(\frac{1}{\rho}K_h\frac{\partial \theta}{\partial x_i}\right) + S\theta \qquad 4.2$$

where the symbols are as described previously, K_h is an eddy mixing coefficient, and S represents sources and sinks of potential temperature (heating and cooling).

In the model, the perturbation pressure field (p') was solved using a backwards-in-time method with the following equation:

$$\frac{dp'}{dt} = -\rho C_s^2\left[\frac{\partial u_i}{\partial x_i}\right] + \rho C_s^2\left[\frac{1}{\theta}\frac{d\theta}{dt} - \frac{1}{E}\frac{dE}{dt}\right] \qquad 4.3$$

where u_i = the velocity component, C_s is the speed of sound which is a function of temperature, and E is a function of mixing ratios. Finally, a number of variables including number concentration, mixing ratios of hydrometeor species, and reflectivity factor were solved using equations of the same general form. The equation for mixing ratio of a given hydrometeor species ‘m’ is given here as an example:

$$\frac{\partial Q_m}{\partial t} = -\frac{1}{\rho}\frac{\partial \rho u_i Q_m}{\partial x_i} + \frac{Q_m}{\rho}\frac{\partial \rho u_i}{\partial x_i} + \frac{\partial}{\partial x_i}\left(\rho K_h\frac{\partial Q_m}{\partial x_i}\right) + \frac{1}{\rho}\frac{\partial\left(\rho \overline{V}_{tQ} Q_m\right)}{\partial x_3} + SQ_m \qquad 4.4$$

where all variables are as described previously, V_t represents the terminal velocity of the hydrometeor species, and S includes any number of sources and sinks for the species. Terms on the right hand side of the equation, from left to right, represent flux of the quantity of interest, divergence of the quantity of interest, mixing in turbulent eddies, a vertical flux term representing fallout of hydrometeors, and a term representing any additional sources or sinks (Straka and Mansell 2011).

Scalars were solved using a forward-in-time first-order difference. For any scalar φ:

$$\varphi^{n+1} = \varphi^{n} - u\Delta t(\partial\varphi / \partial x) \qquad 4.5$$

where Δt is the time step. A value for $u(\partial\varphi/\partial x)$ is obtained using a sixth-order Crowley scheme:

$$\begin{aligned} u(\partial\varphi / \partial x) &= (au / \Delta x)(\varphi_{i+3} - \varphi_{i-3}) + (bu / \Delta x)(\varphi_{i+2} - \varphi_{i-2}) \\ &+ (cu / \Delta x)(\varphi_{i+1} - \varphi_{i-1}) \end{aligned} \qquad 4.6$$

where {a, b, c} are coefficients. Velocity components were solved using a leapfrog scheme:

$$\varphi^{n+1} = \varphi^{n-1} - 2u^{n}\Delta t(\partial\varphi^{n} / \partial x) \qquad 4.7$$

Microphysics were either liquid-only (Kessler 1969), as in Soong and Ogura (1973) and Klemp and Wilhelmson (1978), and identical to the scheme used in Adlerman and Droegemeier (2005), or ice-inclusive. The ice scheme included fifteen hydrometeor species summarized in Table 4.2. Graupel, frozen drops, hail, and ice crystal aggregates were allowed to have varying density described by a power law relationship. Mass and terminal fall velocity were also written as power-law relationships which are a function of diameter. The microphysical distributions were specified by gamma distributions, and the slope, intercept, and shape parameters were solved using a triple-moment scheme including number concentration, LWC, and reflectivity factor. Using a triple-moment scheme should provide a better representation of varying microphysical distributions in a simulation with many precipitation regimes (Gilmore et al. 2004b).

Numerous microphysical processes were allowed in the SAM ice microphysics parameterization. One growth pathway led to warm rain production. In this case, condensation on cloud condensation nuclei (CCN) leads to the formation of a cloud droplet, which may grow further by vapor diffusion. Collection is allowed to begin once cloud droplets are of sufficient size. Once these droplets cross over the threshold of 82 μm, they are transferred to drizzle via autoconversion. Drizzle droplets may grown via further collection, and when they cross the 500 μm threshold, are classified as warm rain. Warm rain can grow further by collection. Ice nuclei within a raindrop can become activated, causing immersion freezing and the formation of hail from frozen drops (Straka and Mansell 2011).

Ice-inclusive processes are more complex and numerous. Once an ice nucleus is activated, an ice crystal may form. These crystals may take the form of plates, columns, dendrites, or bullet rosettes. Once an ice crystal exists, it can begin collecting other hydrometeors. These hydrometeors may be liquid (riming) or ice (collection). Plates are restricted to only collect liquid droplets if their radius is between 150 and 3000 μm, and column riming is restricted to column diameters of 25 – 3000 μm. Once the ice particle reaches a diameter of 500 μm and has lost its ice crystal character, it is classified as graupel. Further riming may result in formation of hail from graupel once the particle diameter crosses 5000 μm, where wet growth begins. Once the hailstone diameter exceeds 9000 μm, liquid droplets can be shed whose most common radius is 1000 μm; these drops are classified as rain from shedding. A melted hailstone or graupel particle would be classified as rain from melting (Straka and Mansell 2011).

Ice crystals can also collect other ice crystals, leading to the formation of snow aggregates. Once a snow aggregate has formed, it is allowed to grow further by collection. Ice crystals or snow aggregates can be collected, leading to continued classification as a snow aggregate but generally decreasing particle density. Aggregates are allowed to melt, forming rain from melting. An aggregate can also collect supercooled cloud droplets via riming, increasing the aggregates' density. Once a diameter of 500 μm is reached, the particle is classified as graupel, with the same progression to hail from graupel possible as described above (Straka and Mansell 2011).

SAM output files were visualized using iMRV, an IDL iTool for meteorological visualization created and supported by Erik Rasmussen at Rasmussen Systems. Visualizations were constructed at 5 min intervals containing vertical velocity and vertical vorticity at 1000 m, and changes in updraft and vorticity distributions were used to determine if the mesocyclone was steady, cyclic occluding, or cyclic non-occluding. Maximum surface vertical vorticity at each interval in association with the mesocyclone was recorded, and at the time of simulation maximum surface vertical vorticity, plots were constructed of surface potential temperature distribution and the vertical and horizontal wind components. Various wind and vorticity characteristics of the simulations were plotted on the wind profile parameter space.

For each wind profile, one liquid-only and one ice-inclusive simulation was run and analyses completed from 3000s – 9000s. At the time of maximum vertical vorticity at the lowest model level in each simulation, the hail, graupel, frozen drop, and rain distributions were plotted over color-filled contours of reflectivity factor. The maximum value of each hydrometeor type was also recorded for each simulation at the time of maximum near-surface vertical vorticity. Calculations were completed representing the ratio of maximum mixing ratios of hail from graupel to hail from frozen drops, maximum graupel to frozen drops mixing ratios, and maximum warm rain mixing ratio as a percentage of summed maximum rain mixing ratios. These variables were then plotted on the wind profile parameter space.

b. Experiments with Varying Moisture Profiles

A control profile was chosen which produced a long-lived, isolated, classic supercell (profile 11 from Table 4.1). It was characterized by a half-circle turn over the lowest 10 km with a radius of 25 m s^{-1}. Its midlevels were defined as the layer from 3.14 – 6.28 km, while upper levels were defined as 6.28 – 12 km. Drying was applied to the midlevels, and to mid and upper levels (3.14 – 12 km; referred to as the ‘deep layer’). At midlevels, a maximum of 1 g kg^{-1} (*moderate midlevel drying*) or 2 g kg^{-1} (*significant midlevel drying*) was applied. When mid and upper levels were dried, a maximum of 63.25% of the mixing ratio (*moderate deep-layer drying*) or 83.67% of the mixing ratio (*significant deep-layer drying*) was applied. This maximum drying was applied at the center of the layer, with amount of drying tapering off to zero at the edges of the layer using a sine curve. No modifications were made to the moisture profile outside the appropriate layer, and no modifications were made to any field other than the mixing ratio. For each altered moisture profile, a liquid-only and ice-inclusive simulation was run. Table 4.3 summarizes the 10 variable-moisture simulations.

Setup for the variable-moisture simulations was identical to that described above. Output files were again created every 5 min from 3000 s – 9000 s (50 min – 2.5 hrs) and visualized with iMRV. At each 5-min output step, maximum 1000-m mixing ratio was recorded for graupel, frozen drops, hail from graupel, hail from frozen drops, rain from shedding, rain from melting, and warm rain, along with maximum near-surface vertical vorticity associated with the mesocyclone (hereafter ‘vertical vorticity’). In liquid-only simulations, only maximum near-surface vertical vorticity was recorded. ‘Near-surface,’ in this case, is defined as the lowest model level (75 m). From these values, time series were constructed for each microphysical variable and vertical vorticity. These time series were compared with the control simulations and across the parameter space of moisture variations, and associations were sought between vertical vorticity and the microphysical variables.

Table 4.1: Summary of the 22 wind profiles used to simulate supercell storms in this study. Columns include the simulation number, a description of the wind profile, the CAPE value in J kg^{-1}, the 0 – 6 km bulk Richardson number (BRN) shear, and the BRN calculated over the 0 – 6 km layer.

Profile #	Description	CAPE (J kg^{-1})	BRN shear (0 - 6 km)	BRN (0 - 6 km)
1	Half-circle in lowest 6 km; radius = 18 m s^{-1}	2200	18	13.6
2	Half-circle in lowest 6 km; radius = 9 m s^{-1}	2200	9	54.3
3	Half-circle in lowest 6 km; radius = 11 m s^{-1}	2200	11	36.4
4	Half-circle in lowest 6 km; radius = 15 m s^{-1}	2200	15	19.6
5	Full circle in lowest 10 km; radius = 15 m s^{-1}	2200	16.1	17.0
6	Full circle in lowest 10 km; radius = 19 m s^{-1}	2200	20.4	10.6
7	Full circle in lowest 10 km; radius = 25 m s^{-1}	2200	26.9	6.1
8	Three-quarter circle in lowest 10 km; radius = 15 m s^{-1}	2200	14.2	21.8
9	Three-quarter circle in lowest 10 km; radius = 19 m s^{-1}	2200	18	13.6
10	Three-quarter circle in lowest 10 km; radius = 25 m s^{-1}	2200	23.7	7.8
11	Half-circle in lowest 10 km; radius = 25 m s^{-1}	2200	17.7	14.0
12	Half-circle in lowest 10 km; radius = 30 m s^{-1}	2200	21.2	9.8
14	Straight-line hodograph with tail length = 47 m s^{-1}	2200	11.6	32.7
16	Quarter-circle 0 - 1 km with r = 10 m s^{-1}; 1 - 9 km tail length = 20 m s^{-1}	2200	13.2	25.3
17	Quarter-circle 0 - 1 km with r = 15 m s^{-1}; 1 - 9 km tail length = 20 m s^{-1}	2200	17.8	13.9
18	Quarter-circle 0 - 1 km with r = 20 m s^{-1}; 1 - 9 km tail length = 20 m s^{-1}	2200	22.4	8.8
19	Quarter-circle 0 - 3 km with r = 10 m s^{-1}; 3 - 9 km tail length = 20 m s^{-1}	2200	10.4	40.7
20	Quarter-circle 0 - 3 km with r = 15 m s^{-1}; no tail above 3 km	2200	13.3	24.9
21	Quarter-circle 0 - 3 km with r = 15 m s^{-1}; 3 - 9 km tail length = 20 m s^{-1}	2200	14.8	20.1
22	Quarter-circle 0 - 3 km with r = 15 m s^{-1}; 3 - 9 km tail length = 40 m s^{-1}	2200	16.4	16.4
23	Quarter-circle 0 - 3 km with r = 15 m s^{-1}; 3 - 9 km tail length = 60 m s^{-1}	2200	18	13.6
24	Quarter-circle 0 - 3 km with r = 20 m s^{-1}; no tail above 3 km	2200	17.7	14.0

Table 4.2: Fifteen hydrometeor species included in the SAM ice microphysics parameterization.

Cloud Droplets	4 - 82 microns
Drizzle	82 - 500 microns
Rain from Shedding	500 - 8000 microns
Rain from Melting	500 - 8000 microns
Warm Rain	500 - 8000 microns
Frozen Cloud Droplets	Variable density
Frozen Raindrops	Variable density
Graupel	500 - 5000 microns
Hail from Frozen Drops	5000 - 51000 microns
Hail from Graupel	5000 - 51000 microns
Plates	Variable density
Columns	Variable density
Dendrites	Variable density
Bullet Rosettes	Variable density
Snow Aggregates	Variable density

Table 4.3: Summary of the ten variable-moisture profiles used in this study. All simulations had the same wind profile, characterized by a half-circle turn in the lowest 10 km with radius 25 m s^{-1}.

Profile #	Name	Microphysics	Description
1	Moderate Midlevel Drying	Ice-inclusive	Max 1 g/kg subtracted, 3.14 - 6.28 km
2	Moderate Midlevel Drying	Liquid-only	Max 1 g/kg subtracted, 3.14 - 6.28 km
3	Significant Midlevel Drying	Ice-inclusive	Max 2 g/kg subtracted, 3.14 - 6.28 km
4	Significant Midlevel Drying	Liquid-only	Max 2 g/kg subtracted, 3.14 - 6.28 km
5	Moderate Deep-layer Drying	Ice-inclusive	Max 63.25% of w subtracted, 3.14 - 12 km
6	Moderate Deep-layer Drying	Liquid-only	Max 63.25% of w subtracted, 3.14 - 12 km
7	Significant Deep-layer Drying	Ice-inclusive	Max 83.67% of w subtracted, 3.14 - 12 km
8	Significant Deep-layer Drying	Liquid-only	Max 83.67% of w subtracted, 3.14 - 12 km
9	Control--Ice	Ice-inclusive	No drying applied
10	Control--Liquid	Liquid-only	No drying applied

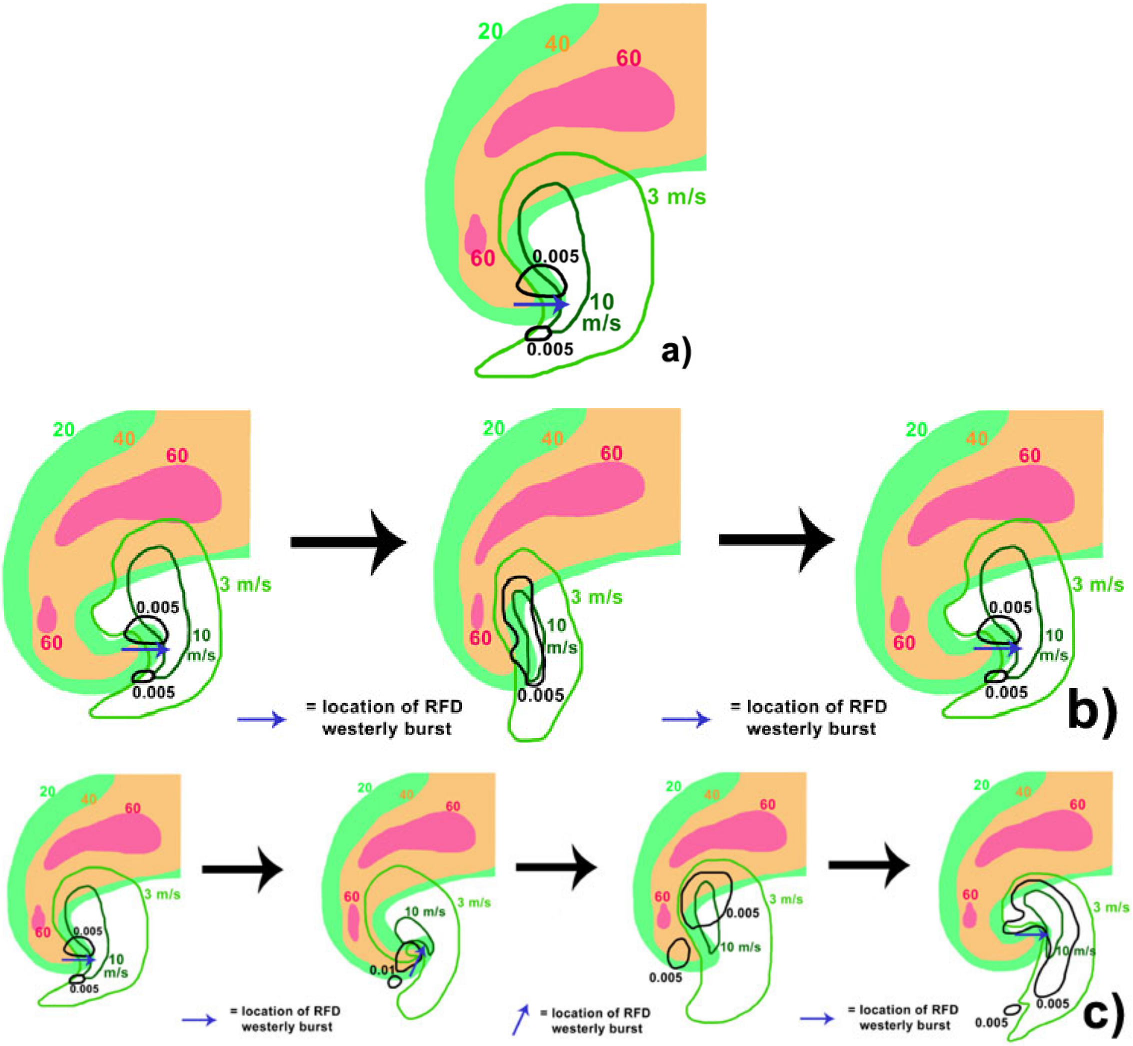

Figure 4.1: Idealized schematics of cycling modes observed in simulated storms, corresponding to the three modes observed by Adlerman and Droegemeier (2005) : a) steady mode, b) occluding cyclic mode, and c) non-occluding cyclic mode. Color shading represents 1000-m reflectivity factor (dBZ), green contours represent 1000 m updraft of 3 and 10 m s^{-1}, and black contours represent 1000 m vertical vorticity of 0.005 s^{-1}. For step two of the non-occluding cyclic process, black contour is 1000 m vertical vorticity of 0.01 s^{-1}. In all schematics, arrows show the location of a westerly surge associated with the RFD.

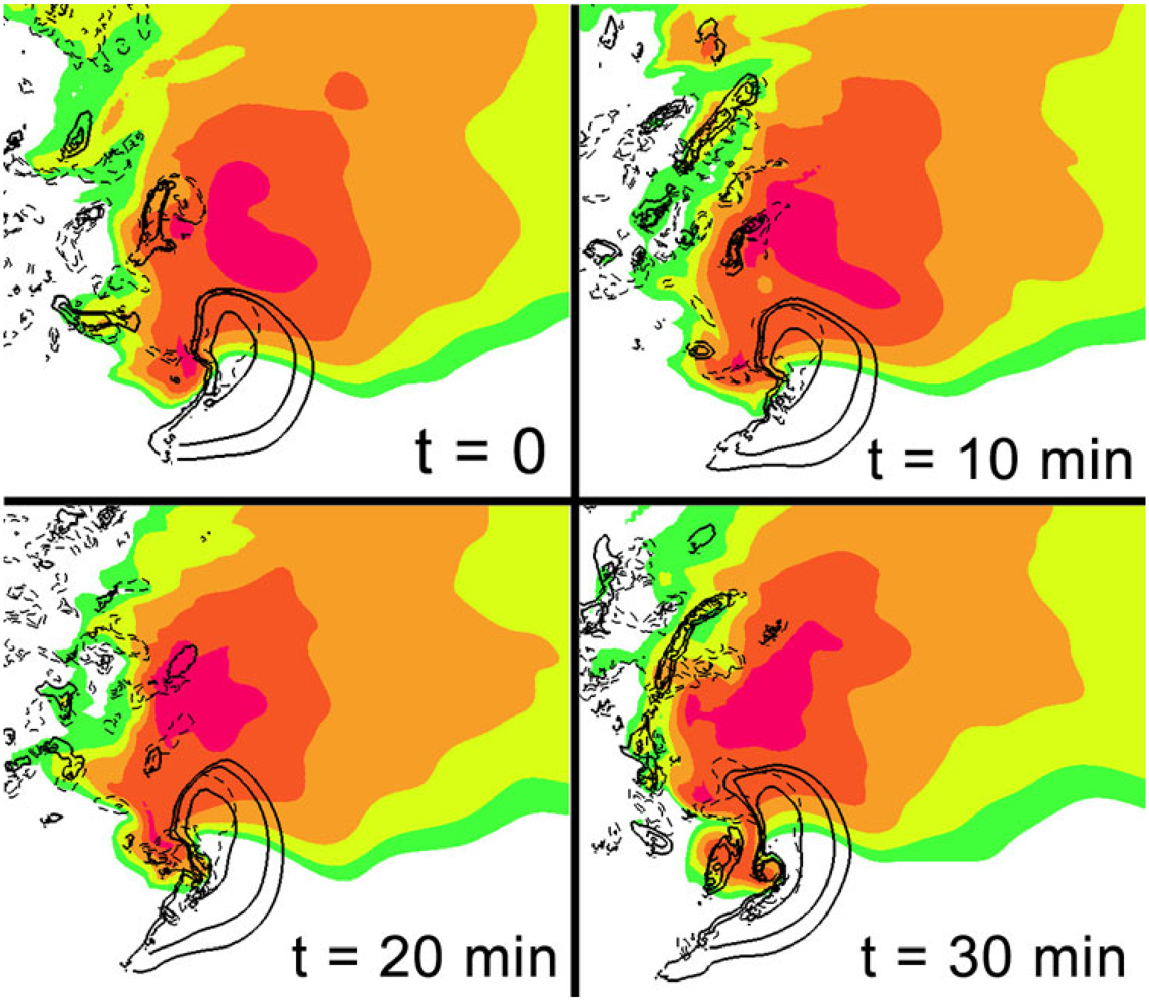

Figure 4.2: Steady mode of mesocyclone behavior, taken from the simulation using wind profile 1. Sequence starts at 4800 s (1 hr 20 min) past model initialization in (a), with following images taken from 10 min following (panel b), 20 min following (panel c), and 30 min following (panel d). Color-filled contours represent reflectivity factor of 20, 30, 40, 50, and 60 dBZ. Solid contours represent 1000 m updraft of 3, 5, and 10 m s^{-1}. Dashed contours represent 1000 m vertical vorticity of 0.005 and 0.01 s^{-1}.

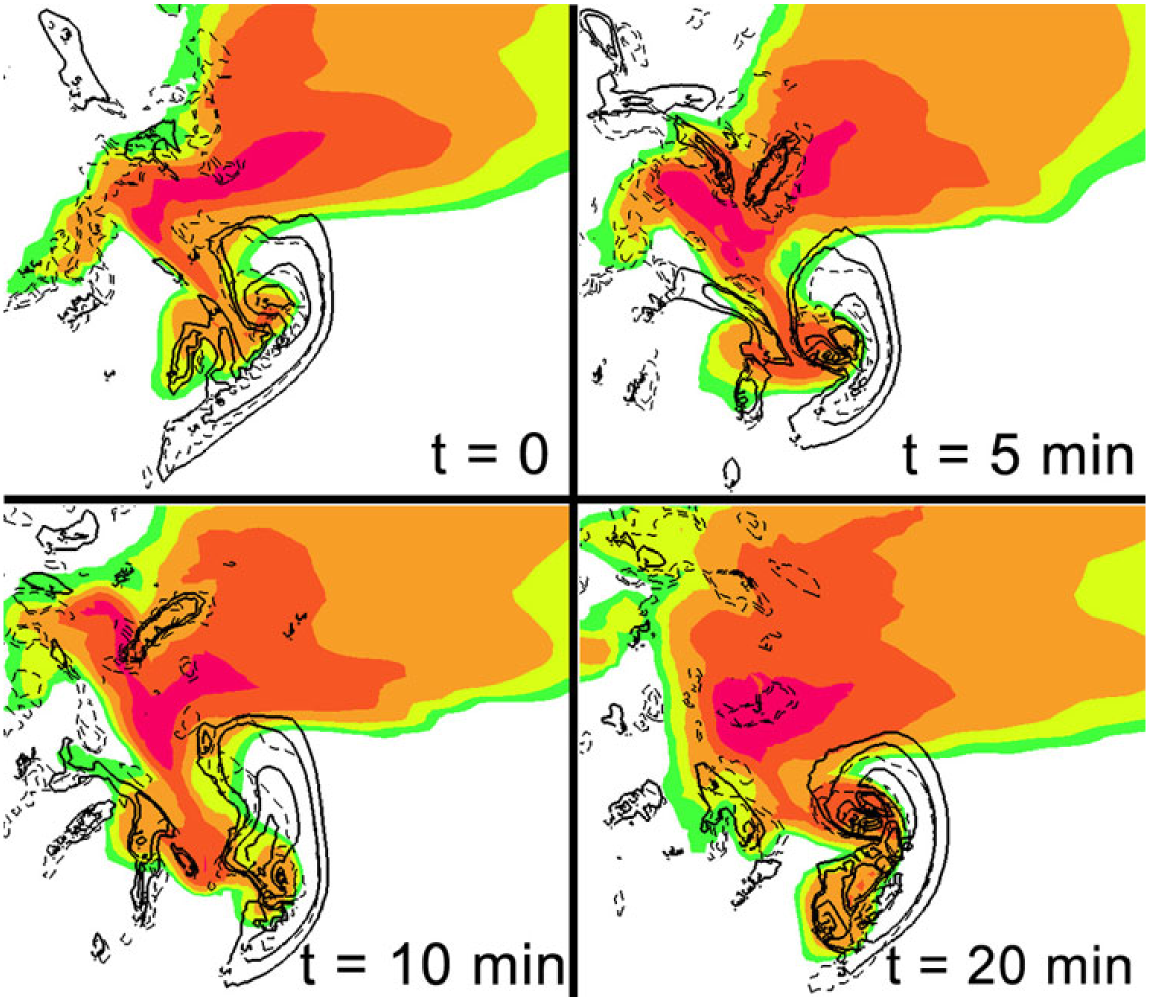

Figure 4.3: Occluding cyclic mode of mesocyclone behavior, taken from the simulation using wind profile 16. Sequence starts at 5700 s (1 hr 35 min) past model initialization in (a), with following images taken from 5 min following (panel b), 10 min following (panel c), and 20 min following (panel d). Features are the same as described for Fig. 4.2.

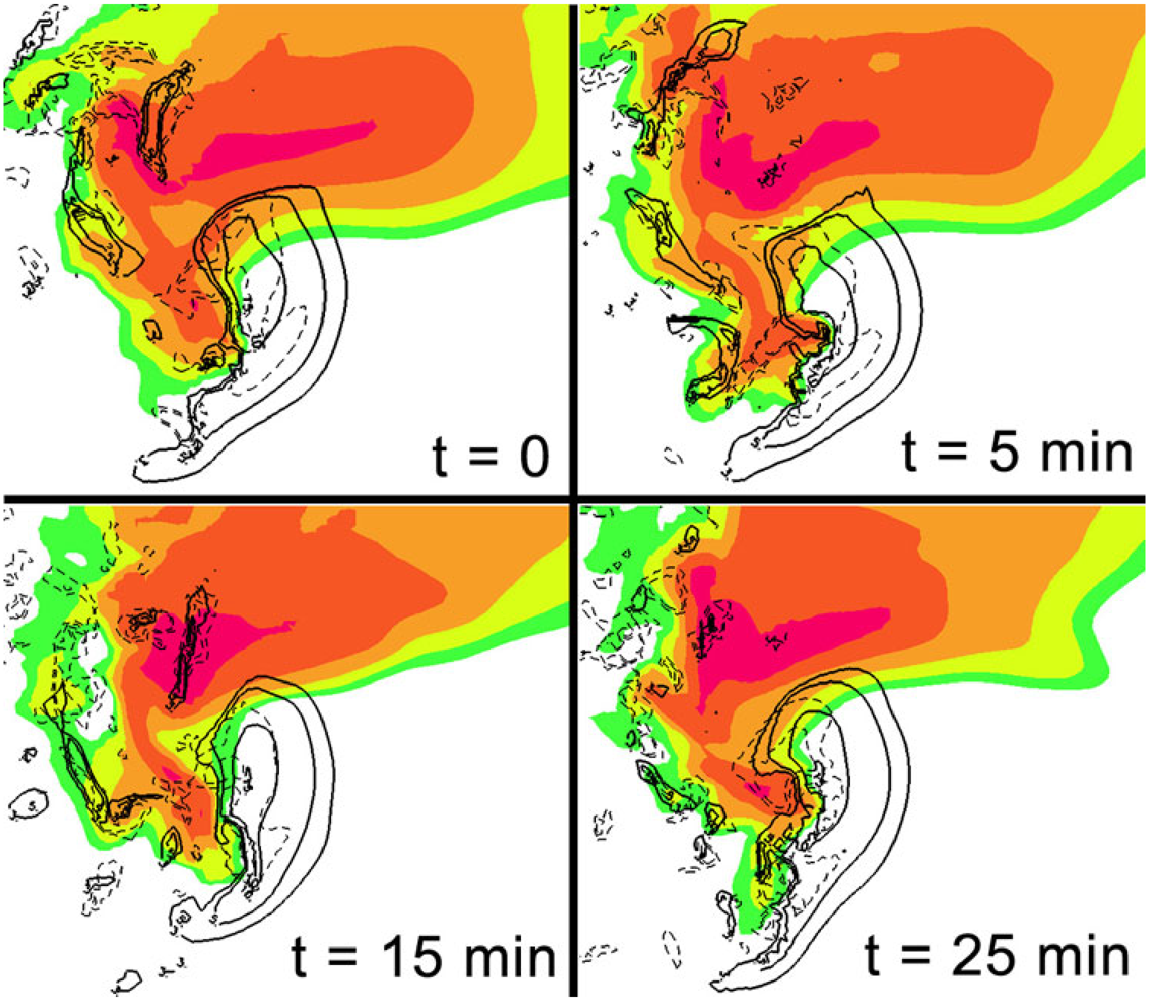

Figure 4.4: Non-occluding cyclic mesocyclone behavior, taken from the simulation using wind profile 21. Sequence starts at 4500 s (1 hr 15 min) past model initialization in (a), with following images taken from 5 min following (panel b), 15 min following (panel c), and 25 min following (panel d). Features are the same as described for Fig. 4.2.

5. Mesocyclone Evolution with Varying Wind Profiles

Evolution of the mesocyclone was explored across the chosen subset of wind profiles, and was defined as described under Terminology and Methodology above. First, it was confirmed that the SAM was producing mesocyclone evolution similar to that seen in prior research, which used liquid microphysics. Then comparisons were made with the results from a detailed ice-inclusive microphysics package. Mesocyclone evolution was assessed via the larger scale (e.g. how the collocated area of updraft and strong vertical vorticity evolved) and on the smaller scale using the RFD westerly surge and near-surface vertical vorticity.

a. Mesocyclone Cycling with Ice and Liquid Microphysics

1) Comparisons with Prior Studies

These results were compared with previous work from the literature to ensure the SAM was producing consistent results. Since these wind profiles were taken from Adlerman and Droegemeier (2005), mesocyclone behavior was compared to their results. Simulations with liquid-only microphysics were compared, as these were most similar to those of Adlerman and Droegemeier's study. Modes of mesocyclone cyclicality were as defined under Terminology and Methodology.

Mesocyclone cycling modes are shown on the parameter space of wind profiles for Adlerman and Droegemeier's study (Fig. 5.1) and for the liquid-only simulations in this study (Fig. 5.2a). These results compare quite well. The significant difference was an expansion of the area of occluding cyclic mesocyclogenesis with the SAM—one wind profile producing a steady mesocyclone in Adlerman and Droegemeier's study produced an occluding cyclic mesocyclone in the SAM, while several simulations changed from non-occluding cyclic to occluding cyclic.

Though these results and those of Adlerman and Droegemeier (2005) agreed relatively well, reasons were sought as to why the SAM may have produced more cyclic occluding storms. Given an identical wind profile between compared simulations, varying instability was thought to be important. CAPE was 3777 J kg^{-1} in Adlerman and Droegemeier's (2005) simulations, but only approximately 2200 J kg^{-1} in this work. All else equal, lower CAPE should produce weaker updrafts, which would reduce total hydrometeor mass fallout from the updraft (e.g. Gilmore et al. 2004b). This may somewhat reduce cold pool strength via less precipitation loading, and possibly via less melting and evaporation. Given the tendency of liquid-only microphysics to produce unrealistically strong cold pools (e.g. compared to observations, as in Markowski et al. 2002), a slightly warmer cold pool (via less melting/evaporation) or slightly lesser downward motion in downdrafts (via less precipitation loading) could be expected to produce different interactions between inflow and outflow near the boundary of these, e.g. under the mesocyclone. Since the balance between unstable storm-relative inflow and surging cold outflow determines much about mesocyclone behavior, a 40% decrease in environmental CAPE may produce genuine differences in mesocyclone behavior.

For wind profiles 4, 10, and 19, the low-level mixing ratio was increased to yield total CAPE near that used in Adlerman and Droegemeier's study (2005). Simulations were completed with these high-CAPE thermal profiles using ice microphysics, and the mesocyclone cycling results compared with lower-CAPE simulations using the same wind profile. While cycling type was the same regardless of CAPE for wind profiles 4 and 10, for wind profile 19 the supercell was occluding cyclic at high CAPE and non-occluding cyclic at lower CAPE. Thus, there may be some differences in results depending on choice of CAPE. The key result, however, is that these liquid-only simulations produced cycling results very similar to those of Adlerman and Droegemeier. Liquid and ice simulations for each wind profile were run using the same CAPE, so these simulations are directly comparable.

2) Results with Ice Microphysics

Liquid and ice microphysics produced different patterns of mesocyclone cyclicality. For this choice of CAPE, non-cyclic storms did not occur with ice-inclusive microphysics (Fig. 5.2b), while non-occluding cyclic storms, which had not previously occurred in this subset of Adlerman and Droegemeier's parameter space, became the dominant mode of mesocyclone behavior. Occluding cyclic storms occupied a regime characterized by low shear and another at high shear.

The most prominent difference between liquid and ice microphysics occurred with full-circle hodographs (Fig. 5.2). In liquid-only simulations, storms were only briefly supercellular and possessed steady non-cycling mesocyclones. After a short time, the cold pool of these storms surged eastward, resulting in extensive walls of updraft and a rapid transition to squall lines. When ice-inclusive microphysics were run, however, storms were maintained as supercells with a usually continuous mesocyclone containing strong collocation of strong updraft and enhanced vertical vorticity. These storms' mesocyclones tended to build northward along RFD outflow, with a new surface center of vertical vorticity eventually developing northward of its initial location. This was consistent with non-occluding cyclic behavior, and occurred given all quantities of wind shear tested.

Supercells in environments with three-quarter-circle wind profiles consistently exhibited occluding cyclic mesocyclones with liquid-only microphysics. While this was also true under weak environmental shear using ice-inclusive microphysics, a transition to non-occluding cyclic behavior occurred as shear increased. This transition seemed to occur with a hodograph radius of approximately 19 m s^{-1}. The mesocyclone of the storm simulated with this wind profile exhibited distinct periods of time in which each occluding and non-occluding cyclic behavior were dominant.

Using liquid-only microphysics, most supercells given half-circle wind profiles produced occluding cyclic mesocyclones except at very weak shear. Half the simulations with ice-inclusive microphysics produced the same occluding cyclic behavior, while the remaining half contained non-occluding cyclic mesocyclones. Non-occluding cyclic behavior was generally dominant for moderate environmental shear. Simulations with very weak and strong shear produced better-focused westerly surges in the RFD, leading to occlusion as the unstable inflow was cut off.

b. Vertical Vorticity Evolution with Varying Wind Profiles

Several variables related to updraft strength and the timing and efficiency of vertical vorticity concentration were plotted on the wind profile parameter space. These fields were compared between ice and liquid simulations, and attempts were briefly made to explain differences.

Simulations were examined from 3000s – 9000s (50 min – 2.5 hrs). Thus twenty-one output steps were available for each simulation, since model output was produced each 5 min. Number of these steps with updraft magnitude > 15 m s^{-1} at 1000 m above the surface was plotted on the parameter space for ice and liquid (Fig. 5.3). Most notable overall was the larger number of steps with strong updraft in liquid-only simulations. This difference seemed related to stronger cold pools, causing cool outflow to surge eastward and strengthen updrafts into which they moved. Updraft tended to be more intense in full-circle simulations, in which storms rapidly evolved into squall lines with strong updraft regions along their leading edges. For other hodograph shapes, more liquid-only simulations had some steps with updraft exceeding 15 m s^{-1}. This also seemed related to a stronger cold pool with liquid microphysics, leading to a markedly stronger RFD westerly surge.

Time of the first strong vertical vorticity maximum at the lowest model level (75 m) was plotted on the parameter space (Fig. 5.4a), along with the difference between ice and liquid simulations (Fig. 5.4b). A strong maximum was defined as a temporal maximum at least half as strong as the simulation's maximum vertical vorticity value. Both sets of simulations showed a trend toward increasing time to concentrate vertical vorticity at the surface as shear increased; this trend was most obvious in liquid-only simulations. Similar slowing of mesocyclone cycling has been observed in past research as shear increases (e.g. Brooks et al. 1994). Ice-inclusive simulations showed this trend more weakly. The difference field between ice and liquid simulations clearly showed less time for ice-inclusive simulations to concentrate surface vertical vorticity with high shear, though it took slightly longer at low shear. The mesocyclones of supercells in ice-inclusive simulations tended to more quickly develop strong RFDs, especially with strong shear. These RFDs formed zones of strong vertical vorticity to their north.

Average time between successive surface vertical vorticity maxima was calculated, and the difference field between ice and liquid simulations was plotted on the parameter space (Fig. 5.5). For hodograph shapes examined in this study, ice microphysics produced storms which cycled faster relative to liquid-only storms as shear increased. As shear increased, ice-inclusive storms continued to produce mesocyclones with periodic strong RFD surges, though storms produced in liquid-only simulations tended toward linear structures, leading to fewer surface vertical vorticity maxima.

The difference field of maximum surface vertical vorticity was plotted on the parameter space (Fig. 5.6). Magnitude of maximum vorticity was typically larger for ice-inclusive simulations—these storms produced stronger surface vortices for a given shear. This seemed to result from better-developed mesocyclones in the ice-inclusive simulations, consisting of well-defined updraft and RFD regions collocated with enhanced midlevel vertical vorticity. The magnitude of this difference typically increased as environmental shear increased, suggesting the ice-inclusive storms may better utilize increasing environmental shear to develop and maintain intense surface vortices.

To measure each storm’s efficiency at repeatably concentrating surface vertical vorticity, maximum vertical vorticity at the surface was summed across the twenty-one model output times. A difference field of this variable was plotted on the wind profile parameter space (Fig. 5.7). Neither microphysics parameterization repeatably produced higher summed surface vorticity. Readily apparent, however, was a trend toward higher relative summed vorticity in ice-inclusive simulations given higher shear. This reinforces a previous conclusion—ice-inclusive storms seem better able to utilize increasing shear in the processes that generate and maintain surface vortices.

c. RFD Characteristics across the Parameter Space of Wind Profiles

RFD strength varied considerably across the parameter space, so some quantitative comparisons were made between RFD temperature and wind variables. In the following discussion, the RFD was defined as the small-scale region of downdraft closely associated with the mesocyclone, typically located on the south or southwest side of the mesocyclone in or near the echo appendage.

Near-surface vertical vorticity maxima, in all simulations but especially in ice-inclusive simulations, were associated with an RFD westerly surge just south of the surface vortex. This westerly surge was evident as a small-scale region of storm-relative westerly flow generally in the southwest portion of the mesocyclone. Magnitude of westerlies in the RFD surge was approximated for each simulation and the difference field plotted on the wind profile parameter space (Fig. 5.8). A stronger RFD westerly component was often present in liquid-only simulations. This stronger component seemed to be the result of liquid-only storms having stronger cold pools west of the updraft. A notable exception was with full-circle hodographs, in which ice-inclusive supercells often contained a stronger RFD surge. This resulted from the more defined mesocyclone structure in these storms, with distinct updraft and RFD regions collocated with enhanced midlevel vertical vorticity. The full-circle hodograph with strongest shear was the exception—the liquid-only simulation produced a powerful squall line with an RFD westerly surge of 50 m s^{-1} behind the outflow boundary. This was the strongest westerly surge in any simulation.

Maximum potential temperature gradient across the RFD boundary near the westerly surge was plotted on the wind profile parameter space (Fig. 5.9). This gradient averaged twice as strong for liquid-only storms. The RFD tended to be uniformly cool in most liquid-only simulations, with a few warmer cases among half-circle hodographs. In ice-inclusive storms, full-circle and half-circle hodographs tended to produce relatively cool RFDs, while three-quarter-circle hodographs produced warmer RFDs relative to the full parameter space.

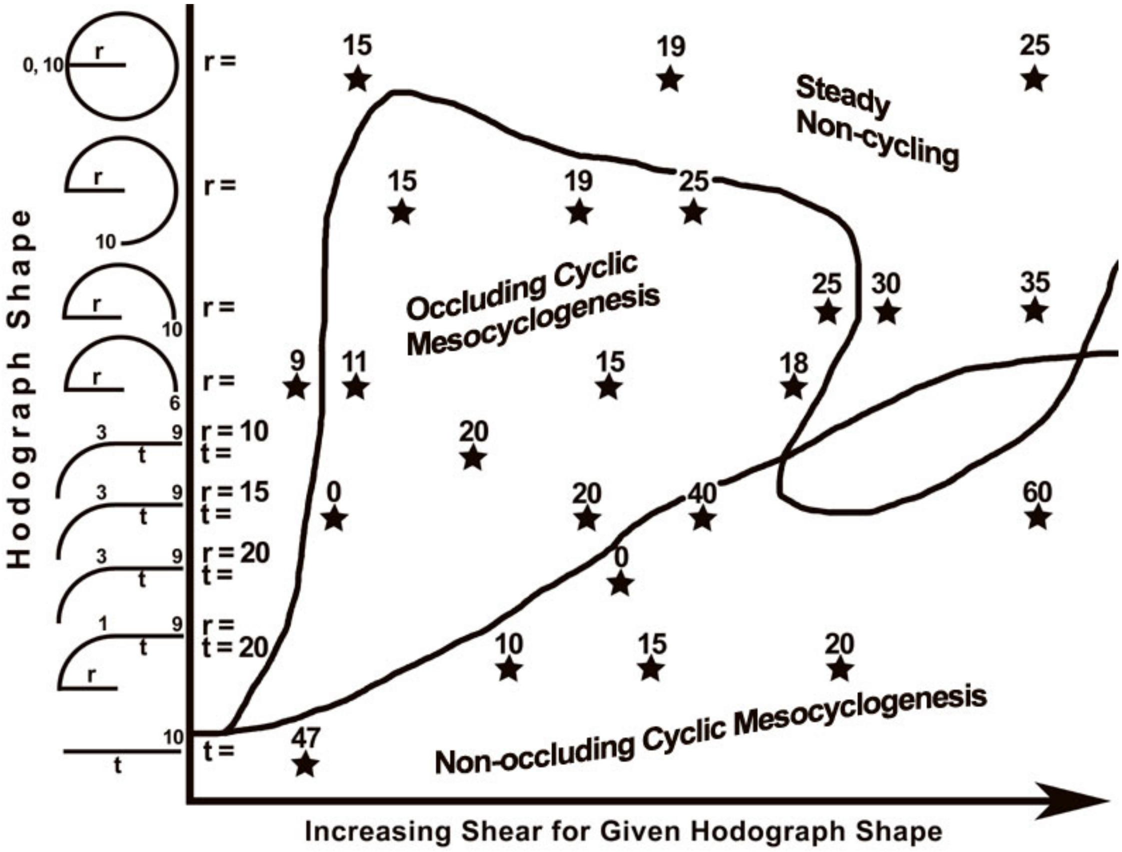

Figure 5.1: Mesocyclone cycling modes observed in the study of Adlerman and Droegemeier (2005). Approximate boundaries between cycling modes are denoted by black lines. Hodograph shapes are on the left side of the diagram. Each star represents one simulation, and the number above the star represents either the radius of curvature or the tail length of the wind profile, as denoted by the r (radius) or t (tail length) to the left.

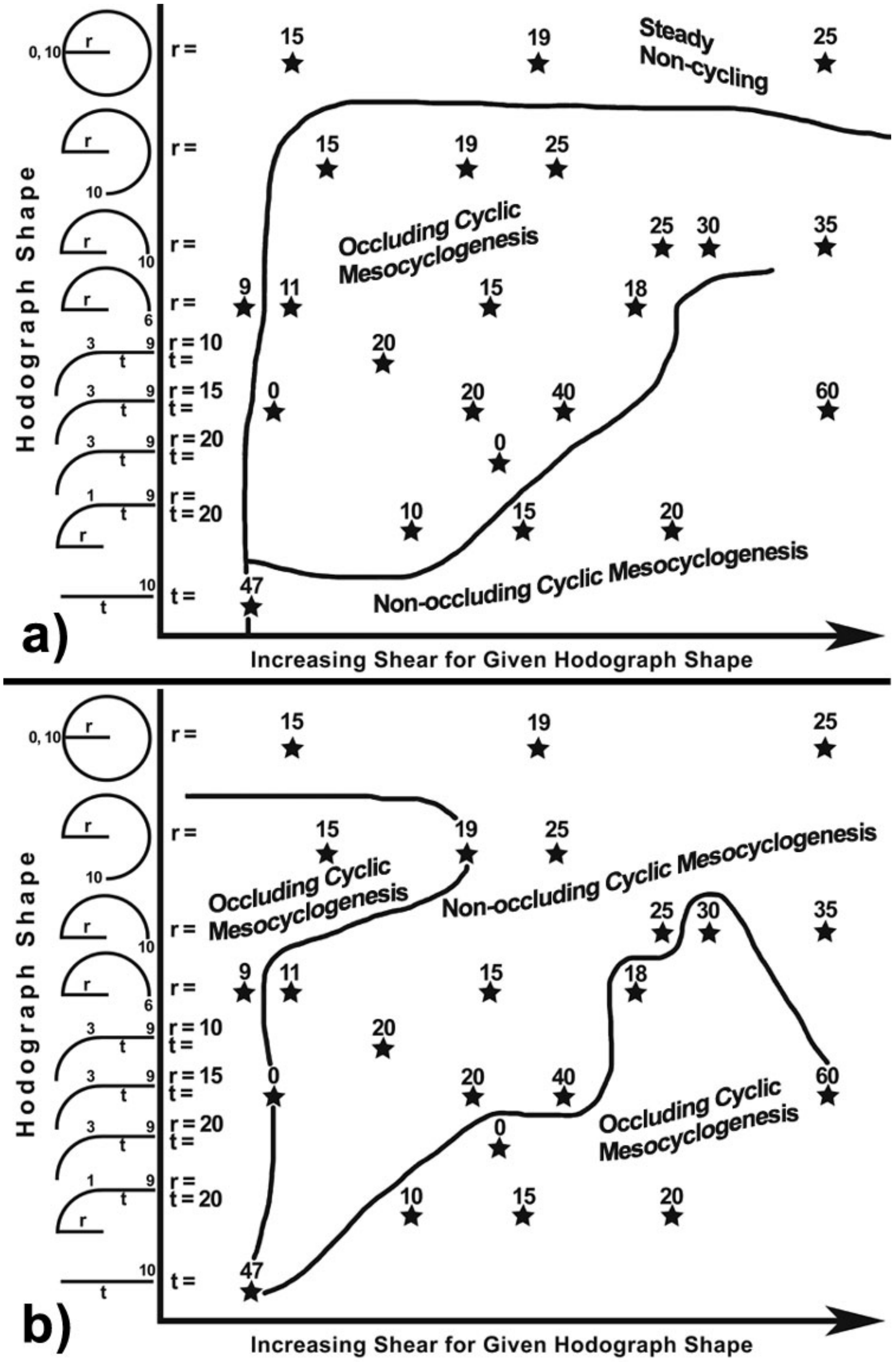

Figure 5.2: Mesocyclone cycling modes observed in this study, with a) liquid-only microphysics and b) ice-inclusive microphysics. Simulations are labeled on the parameter space as described in Fig. 5.1. Lines denote approximate boundaries of observed cycling types, presented in Fig. 4.1 of Terminology and Methodology.

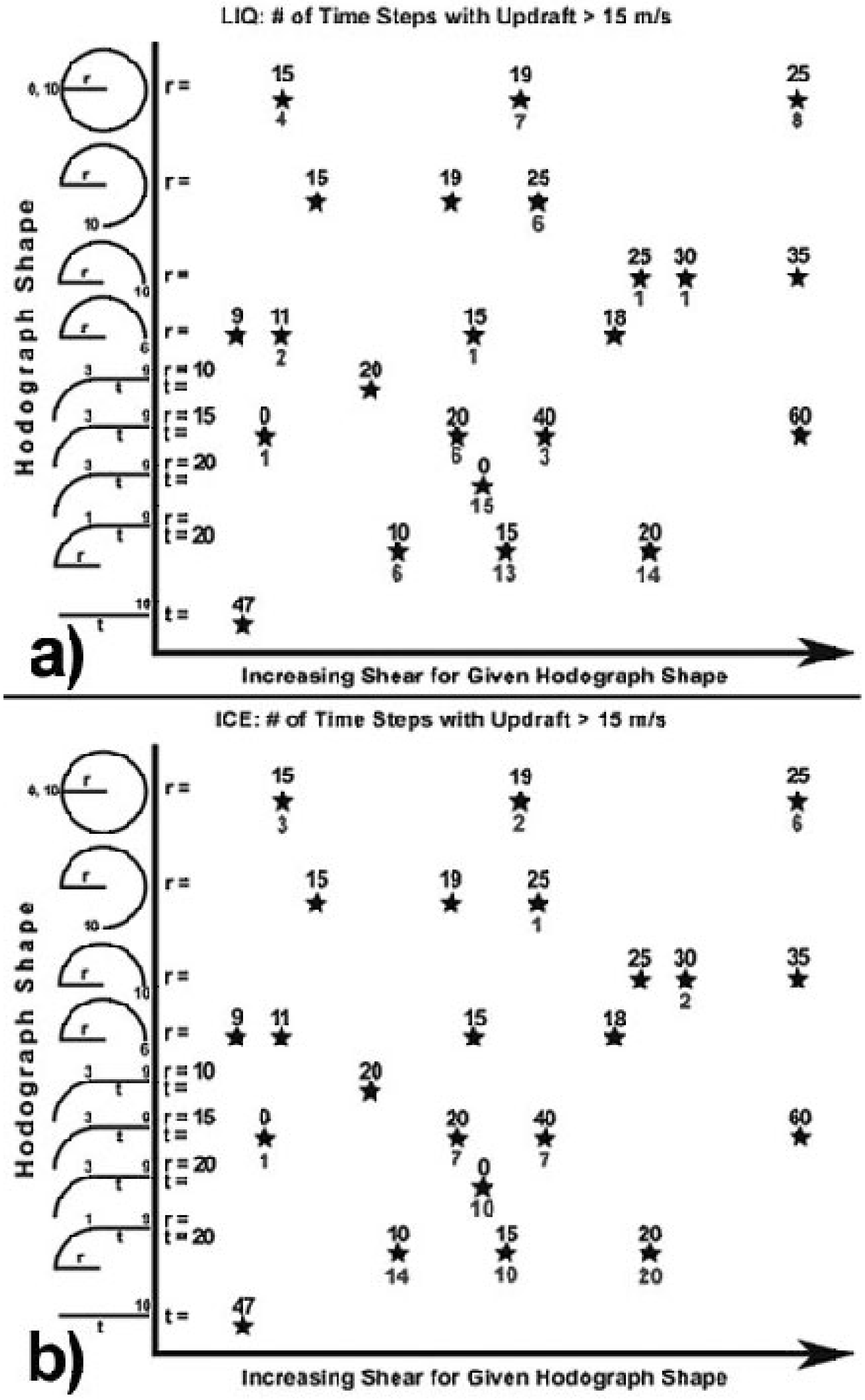

Figure 5.3: Number of model output steps with maximum 1000 m updraft of at least 15 m s^{-1} for a) liquid-only simulations, and b) ice-inclusive simulations. Simulations are denoted as described in Fig. 5.1, and number of steps is shown by the number below each star. If no number is present, no steps contained an updraft this strong at 1000 m.

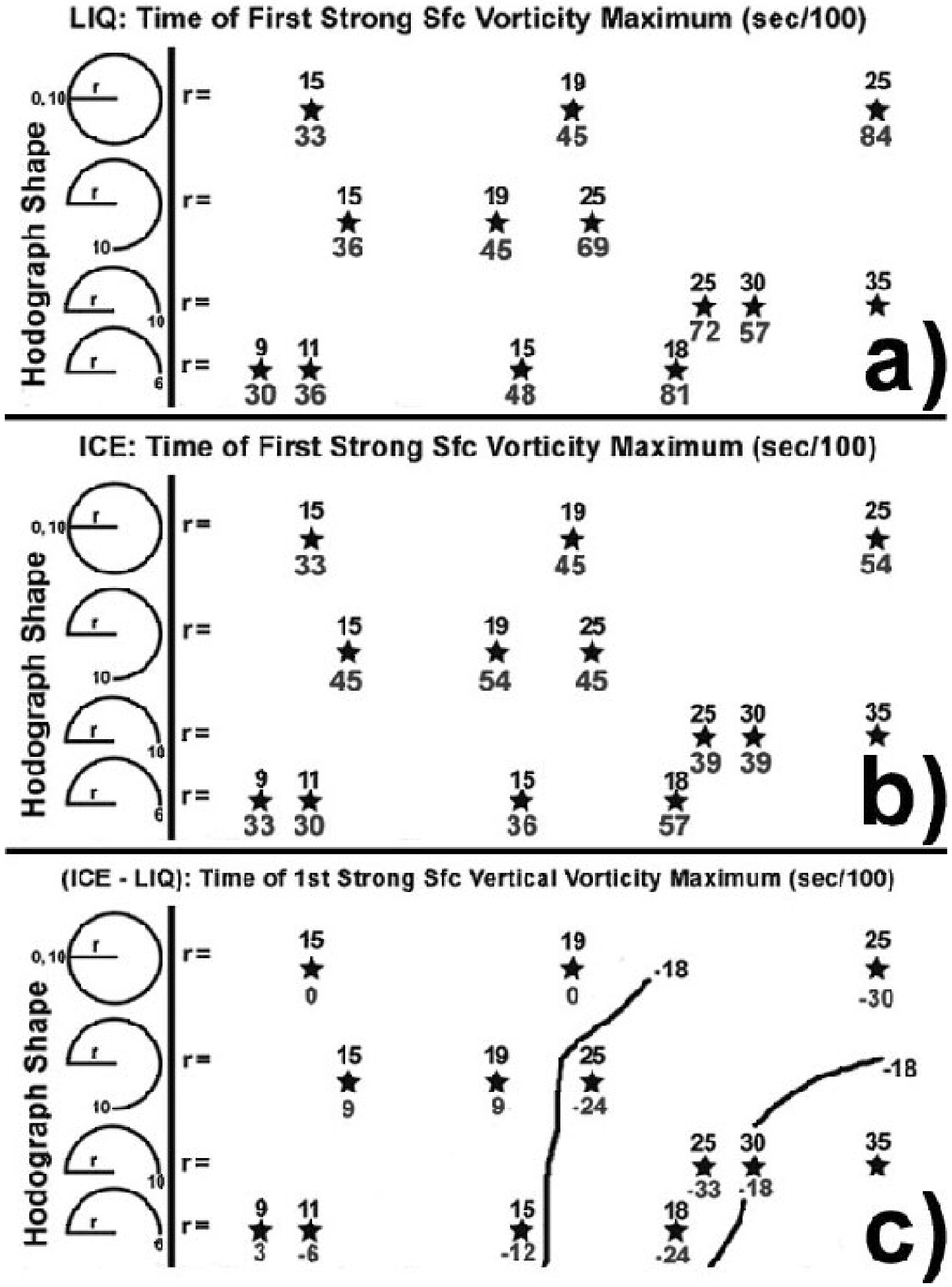

Figure 5.4: Time of the first surface vertical vorticity maximum with magnitude at least 50% of the simulation maximum for a) liquid-only simulations, and b) ice-inclusive simulations. c) shows the difference field (ice minus liquid) for this variable. Times, under each star, are seconds from model initialization divided by 100 (e.g. 3300 s = 33). The -1800 s contour is highlighted in (c).

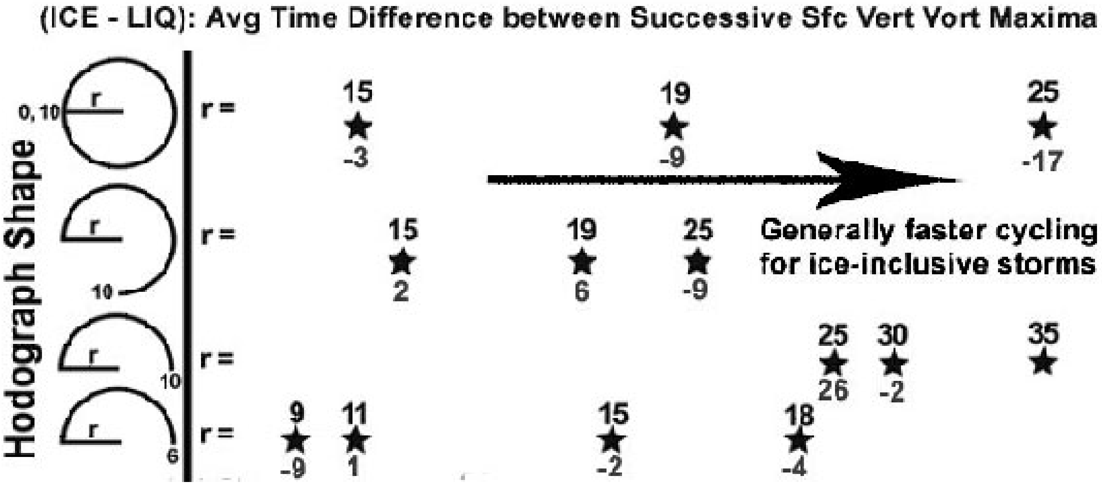

Figure 5.5: Average time difference between successive surface vertical vorticity maxima, calculated as ice minus liquid value. The number below each star represents this difference in minutes.

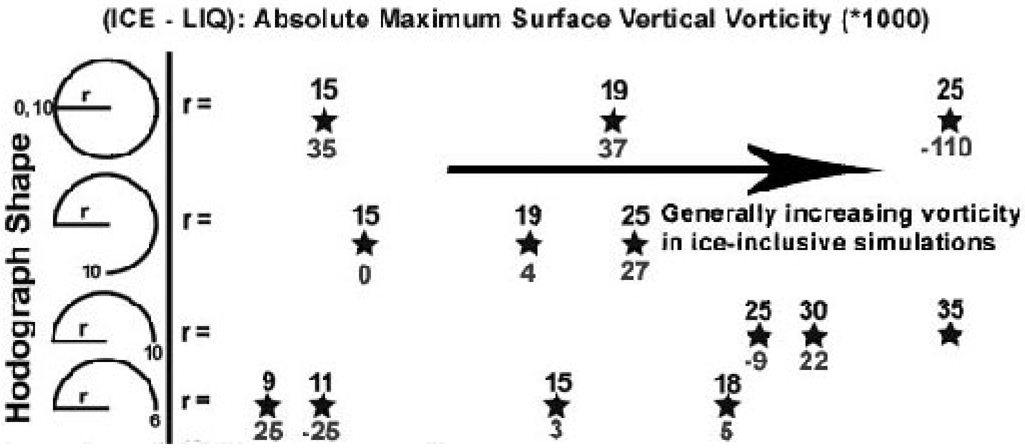

Figure 5.6: Difference in maximum surface vertical vorticity, calculated as ice minus liquid. The number below each simulation represents this difference multiplied by 1000 (e.g. 35 = 0.035).

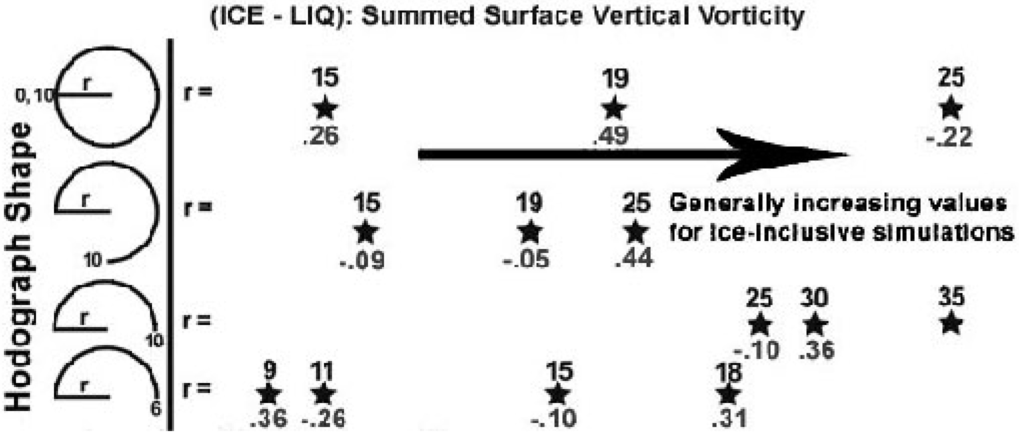

Figure 5.7: Maximum surface vertical vorticity difference, calculated as ice minus liquid, summed across the twenty-one model output steps in each simulation. Numbers below this star represent this difference in units of s^{-1}.

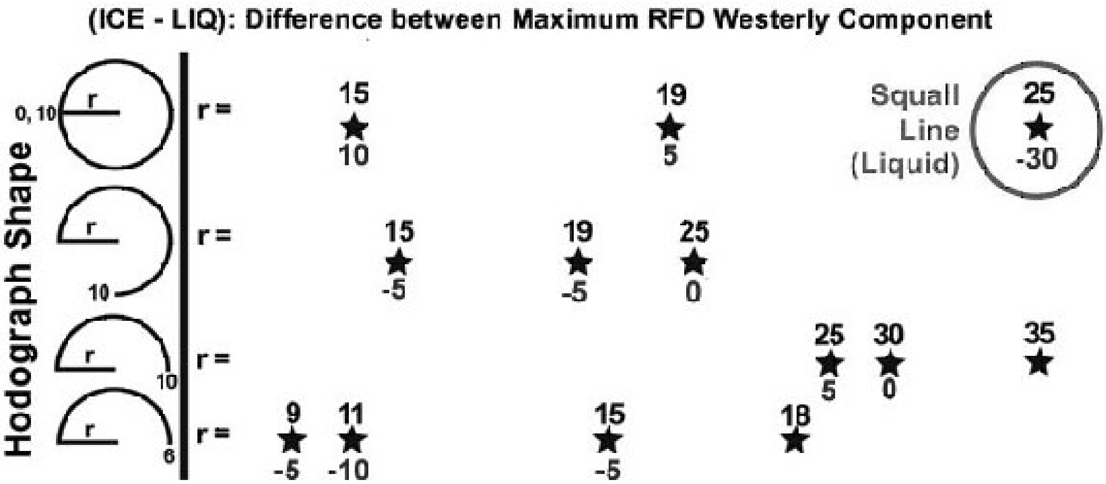

Figure 5.8: Approximate difference (to the nearest 5 m s^{-1}) of the strongest westerly component in the RFD, calculated as ice minus liquid value, at the time of maximum surface vertical vorticity. Number below each star represents this difference in m s^{-1}.

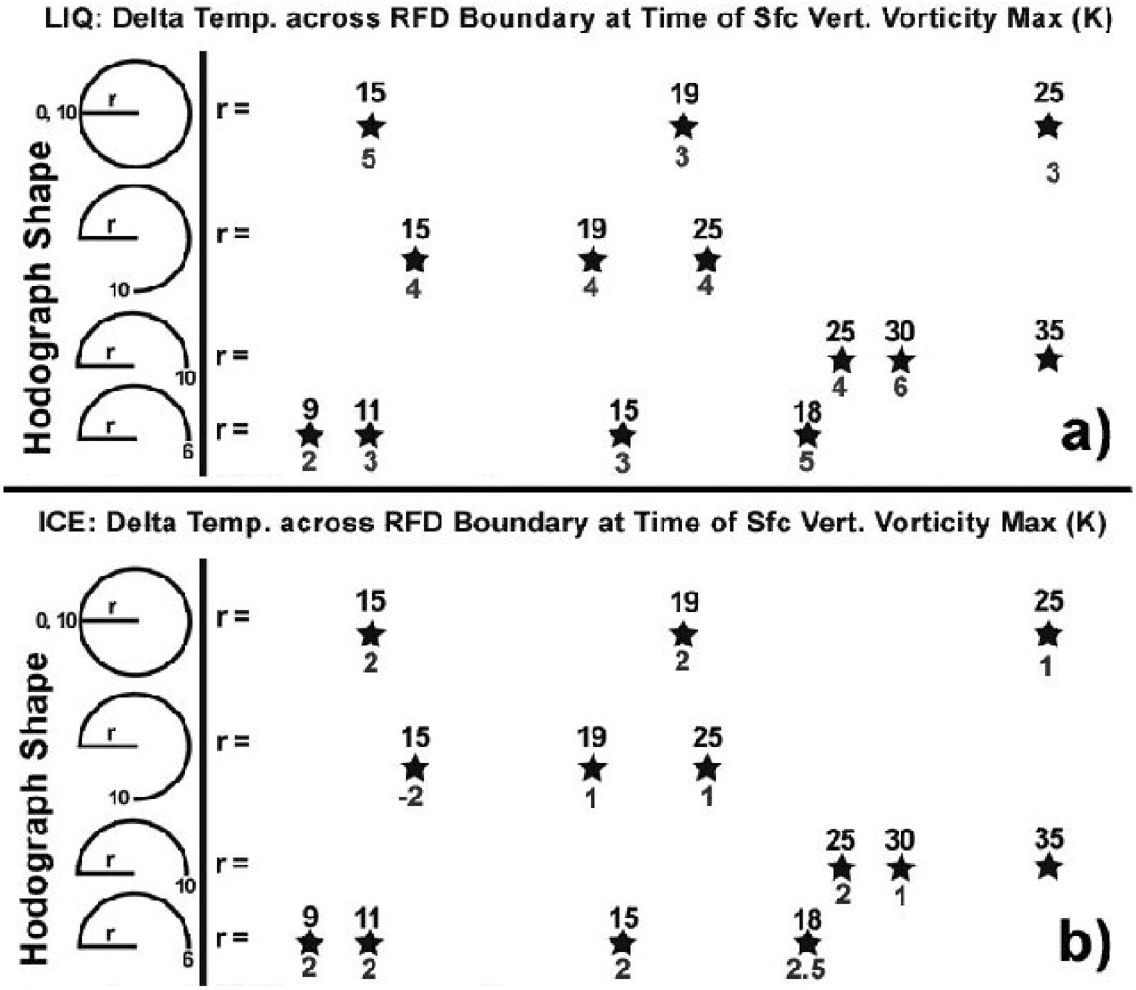
LIQ: Delta Temp. across RFD Boundary at Time of Sfc Vert. Vorticity Max (K)

ICE: Delta Temp. across RFD Boundary at Time of Sfc Vert. Vorticity Max (K)

Figure 5.9: Maximum temperature difference across the RFD boundary, calculated as environmental temperature minus minimum RFD temperature near the RFD boundary. (a) is for liquid-only simulations, while (b) is for ice-inclusive simulations. Numbers below each star represent this temperature difference in Kelvin.

6. Microphysical Variation with Varying Wind Profiles

Given striking differences in mesocyclone evolution across the wind profile parameter space, it would be beneficial to understand reasons for this variability. Much of this variability may be dynamically-induced, though some portion is likely due to microphysical effects. Any microphysical effect should be greater when there is less vertical wind shear. The goal of this chapter is to explore varying microphysics across the parameter space of wind profiles, and to speculate about possible effects of this microphysical variation on low-level supercell evolution.

a. Microphysical Distributions

Across the wind profile parameter space, microphysical distributions were seen to vary significantly. Here are documented variability in the quantity and spatial distributions of several hydrometeor types.

1) Quantity and Spatial Distribution of Hail Variables

In the SAM, two mechanisms were allowed to generate hail. Either graupel accreted supercooled cloud droplets, drizzle, or rain to eventually become a hailstone (referred to here as hail from graupel), or liquid drops froze to become a hail embryo (referred to here as hail from frozen drops). All hail analyses were completed when the simulation-maximum vertical vorticity was occurring at the model's lowest level (75 m).

Quantity of hail from graupel varied by a factor of eleven across the wind profile parameter space (Fig. 6.1a). Hail quantity varied in two primary ways. First, more hail from graupel was produced on average with higher wind shear. While the eight simulations with lowest shear had an average maximum hail from graupel mixing ratio of 1.26 g kg^{-1}, the eight highest-shear simulations had an average value of 2.19 g kg^{-1}. This finding is consistent with more robust updrafts and development of more precipitation particles with greater wind shear, and agrees with prior research which has found greater precipitation fallout at higher shear (Gilmore et al. 2004a). Also, greater production of hail from graupel was found with strongly-curved hodographs. Average maximum mixing ratio of hail from graupel was 2.23 g kg^{-1} over six simulations representing full- and three-quarter-circle hodographs, but only 1.25 g kg^{-1} over the four simulations with least-curved hodographs. Greater production of hail from graupel with strongly-curved hodographs was attributed to seeding potential—with a strongly-curved hodograph, ice particles are more likely to remain in the updraft vicinity, and ice fragments can then serve as nuclei for further ice particle growth. The most strongly-curved hodographs (full circles) also contained the highest average concentration of hail from graupel.

Maximum values of hail from frozen drops at the time of simulation-maximum near-surface vertical vorticity showed less-clear patterns (Fig. 6.1b). The quantity of hail from frozen drops was smaller on average, and varied across the wind profile parameter space by a factor of thirty-four. The eight lowest-shear simulations had an average maximum mixing ratio of 0.65 g kg^{-1}, while the eight highest-shear simulations had a maximum value of 1.02 g kg^{-1}. This 57% increase in mixing ratio is smaller than the 74% increase seen with hail from frozen drops, but both results are thought to represent a meaningful difference. Only a slight difference is seen between average values of the six most strongly-curved and four least-curved hodographs. The distribution of frozen drops is likely more reliant upon the updraft’s temperature profile than on the presence of ice crystals for seeding.

Taking the ratio of hail from graupel to hail from frozen drops, calculated by a simple division of the two maximum mixing ratios, a pattern emerges of relatively more hail from graupel with strongly-curved hodographs (Fig. 6.1c). While the simulations with the six most strongly-curved hodographs produced an average ratio of 3.8, simulations with the four least-curved hodographs produced an average ratio of only 2.6. The sole straight-line hodograph, however, represented a significant exception to this pattern. Assessing differences between high- and low-shear simulations, the average ratio among the eight lowest-shear profiles was 3.3, while for the eight highest-shear simulations was only 2.5. Thus, storms with strongly-curved hodographs and low wind shear tended to produce relatively more hail from graupel, while minimally-curved profiles with strong shear tended to produce relatively high quantities of hail from frozen drops.

Hail spatial distributions at 1000 m were slightly variable depending on wind profile. Full-circle hodographs had the most obviously different distributions, with hail typically oriented somewhat north-south through the storm precipitation core and tending to wrap southward around the west side of the mesocyclone, becoming much closer to the low-level vortex. In contrast, most other simulations contained hail cores oriented more west-east and typically farther from the low-level vortex. This difference makes sense, since a strongly-curved hodograph should promote precipitation fallout relatively near the particle source location. Two simulations with strongly-sheared wind profiles (simulations 12 and 20) also contained relatively high amounts of hail wrapping around the west side of the mesocyclone in a way that might be able to affect the RFD. It is unknown why strongly-sheared storms would produce more hail nearer the west side of the mesocyclone. One possibility is an extra particle source from upstream storms given strong shear.

The distribution and quantity of hail may be important to low-level storm evolution. An idealized study found ice-inclusive downdrafts to become stronger and colder than their liquid-only counterparts (Srivastava 1987), so the quantity of hail may affect supercell downdraft strength. In storms with high hail content, assuming most hail was falling out downwind from the mesocyclone, the FFD might be colder, leading to a stronger temperature gradient along the forward flank (e.g., as speculated in Shabbott and Markowski 2006). In storms with hail able to wrap around the mesocyclone, some effect may be observed as a cooler RFD temperature. Spatial distribution of the hail would determine what fraction of the storm's total hail content would contribute to cooling which downdraft, with more RFD cooling possibly occurring in strongly-curved hodographs and with high shear.

2) Quantity and Spatial Distribution of Graupel and Frozen Drops

Frozen drops and variable-density graupel were included in the SAM. Quantity and spatial distribution of each were investigated across the wind profile parameter space at the time of simulation-maximum vertical vorticity at the lowest model level. Quantity of these smaller ice particles was much more variable across the wind profile parameter space than for hail, varying by a factor of several hundred (for graupel) to ten thousand (for frozen drops). Though most graupel particles and frozen drops were likely melting substantially by the time they reached 1000 m, quantitative analysis was completed at this level to assess effects of relatively near-surface melting on downdraft strength. For graupel, weak trends were observed over the parameter space (Fig. 6.2a). Strongly-curved hodographs tended to produce storms with higher maximum graupel mixing ratios at 1000 m. The six simulations with strongest hodograph curvature had an average maximum graupel mixing ratio of 0.65 mg kg^{-1} at 1000 m, while the three simulations with least hodograph curvature only had an average value of 0.25 mg kg^{-1}. This difference is again attributed to seeding, since environments with strongly-curved hodographs should allow precipitation particles to remain relatively near their formation location, on a horizontal plane. A bias toward more graupel was observed with stronger shear. The seven simulations with weakest wind shear had an average maximum graupel mixing ratio of 0.07 mg kg^{-1}, while the seven strongest-shear simulations had an average value of 0.64 mg kg^{-1}. Increasing graupel with increasing wind shear was most evident given strongly-curved hodographs, with some relatively straight hodograph shapes showing little trend in graupel quantity as shear changed.

Frozen drops showed similar trends (Fig. 6.2b). Mixing ratio of frozen drops generally increased as shear became stronger; this trend was most readily observed with high-curvature wind profiles. While a few strongly-curved hodographs produced storms with exceptionally high frozen drop mixing ratio, this was not universally true—many weakly-curved profiles produced storms with similar frozen drop content to their strongly-curved counterparts. The ratio of maximum graupel to frozen drop mixing ratio showed generally little pattern across the wind profile parameter space, except the three simulations with full-circle hodographs contained higher ratios (e.g. relatively more graupel) than any of the other simulations. This difference is likely related to how each of these particles originate in the SAM. Frozen drops are liquid hydrometeors that freeze, while a graupel particle is an ice crystal that has accreted supercooled droplets. Given a full-circle hodograph with particles more likely to remain in the updraft vicinity, more small supercooled droplets may be present to encourage accretion and graupel growth.

Spatial distributions of graupel and frozen drops were similar across the parameter space, with most of these particles occurring on the north side of the mesocyclone well-removed from the echo appendage. Two exceptions occurred with full-circle hodographs, in which some frozen particles wrapped around the west side of the mesocyclone. In these simulations, melting of small ice particles may have more readily contributed to RFD characteristics, but in other simulations, melting small ice particles would have contributed most to FFD temperature. The possible role of graupel and frozen drops in low-level storm evolution should be similar to that of hail, with effects on the FFD and RFD depending on the quantity and spatial distribution. Effects of graupel and frozen drops may be more prominent than those of hail, however, since the quantity of these particles varied much more than hail quantity.

3) Quantity and Spatial Distribution of Rain Variables

The SAM contains three formation mechanisms for rain. One source of raindrops is melting of ice particles (referred to here as rain from melting). Another source is shedding of liquid droplets from larger melting ice particles such as hail (referred to here as rain from shedding). Finally, rain is allowed to form via warm-rain processes as collision-coalescence produces droplet growth starting from a drizzle regime (referred to here as warm rain). Given variable distributions of ice-phase particles as described above, the distributions and roles of these types of rain also vary depending on the wind profile. Most significantly, the warm rain distribution seems highly dependent on wind shear and may be a significant contributor to downdraft characteristics.

At 1000 m, rain from shedding typically dominated the total rain content. Typical maximum mixing ratios of rain from shedding ranged from 5 – 7 g kg^{-1}, with little pattern across the wind profile parameter space (Fig. 6.3a). Quantity of rain from shedding seemed similar between high and low shear cases, and between simulations with strongly- and weakly-curved hodographs. Maximum values of rain from melting were typically only 2 – 4 g kg^{-1}, with a distinct bias of higher values toward the most strongly-curved hodographs (Fig. 6.3b). Values were less than 3 g kg^{-1} for all lower-curvature cases except two simulations at high shear, while for full-circle and three-quarter circle hodographs, values were nearly all 4 g kg^{-1} or higher. This tendency to produce more rain from melting with strongly-curved hodographs may be related to higher concentrations of graupel particles and frozen drops in those simulations.

Unlike rain from melting and shedding, which varied by only a factor of two across the wind profile parameter space, warm rain varied by a factor of nearly ten thousand (Fig. 6.3c). Most noticeable was the strong bias toward little warm rain with strongly-curved hodographs—warm rain increased quickly as the wind profile became less curved. Average maximum warm rain mixing ratio was 0.00011 g kg^{-1} for simulations with full-circle hodographs, 0.052 g kg^{-1} with three-quarter circle hodographs, 0.161 g kg^{-1} for half-circle hodographs, and 0.273 g kg^{-1} with all other wind profiles. This striking difference was attributed to seeding potential. With strongly-curved hodographs, small ice particles formed in upper portions of the updraft would likely remain nearby, and provide opportunities for seeding and rapid transition to ice-inclusive precipitation growth processes. With fairly straight wind profiles, however, ice particles would be advected away from the updraft region, and less ice would be available to contaminate the upwind updraft column, leading to dominance of a collision-coalescence process there. For some hodograph shapes, warm rain production increased markedly as shear increased. Though this was not universal across the parameter space of wind profiles, it is thought that higher shear should more effectively advect ice particles away from the updraft, allowing less seeding. This should be most true for strongly-curved hodographs, excluding full-circle profiles. Indeed, this effect was most pronounced with three-quarter and half-circle hodographs.

When warm rain was present, it was located on the upshear (typically southwest or west) side of the echo appendage (Fig. 6.3d). This spatial distribution was consistent across the wind profile parameter space, and has been noted in a past modeling study (M. Gilmore, personal communication). This distribution makes sense, because for an isolated storm without microphysical influence from upshear storms, the most upshear portion of the updraft should be least contaminated by ice crystals formed in upper portions of the updraft, which should advect downstream. Warm rain has also been inferred in this location using polarimetric radar data from the 10 May 2010 Oklahoma outbreak (Fig. 6.4). Signatures consistent with warm rain include collocation of moderate reflectivity factor (40 – 45 dBZ), lower differential reflectivity consistent with nearly-spherical drops (0.5 – 1 dB), high correlation coefficient (0.98 – 0.99), and moderate LWC inferred from specific differential phase (Straka et al. 2000).

At the time of maximum near-surface vertical vorticity, maximum mixing ratios of the three rain types were summed, and the contribution from warm rain found as a percentage of the total (Fig. 6.3e). This field is meant to give a sense of relatively how dominant the warm rain process is in the echo appendage region. As expected, warm rain made up a very small percentage of the rain with full- and three-quarter circle hodographs, but for other hodograph shapes, warm rain made up several percent of the total rain. Implications of warm rain quantity on downdraft characteristics will be discussed later in this chapter.

b. Relationships between Microphysical Variables and RFD Characteristics

In this section, associations are assessed between microphysical variables and outflow strength. Focus will be on the RFD, which appears to have the most direct implications for tornadogenesis. RFD strength is examined via maximum theta gradient across the RFD boundary and maximum strength of the RFD westerly surge. All analyses are completed at the time of simulation maximum near-surface vertical vorticity. Microphysical variables considered were maximum mixing ratios of hail from graupel, hail from frozen drops, total hail, graupel, frozen drops, rain from melting, rain from shedding, and warm rain, and warm rain percentage of total maximum rain mixing ratios.

1) Microphysical Associations with the Cross-RFD Theta Gradient

Maximum theta gradient across the RFD boundary near the south side of the mesocyclone was not well-correlated with other variables related to low-level storm evolution such as average cycling time and maximum near-surface vertical vorticity. For this and following investigations, Pearson’s correlation, hereafter correlation, was computed between a given RFD characteristic and microphysical variable. Pearson’s correlation is defined as

$$r = \frac{\sum_{i=1}^{n} x_i y_i - \frac{1}{n}\sum_{i=1}^{n} x_i \sum_{i=1}^{n} y_i}{\sqrt{\sum_{i=1}^{n} x_i^2 - \frac{1}{n}\left(\sum_{i=1}^{n} x_i\right)^2}\ \sqrt{\sum_{i=1}^{n} y_i^2 - \frac{1}{n}\left(\sum_{i=1}^{n} y_i\right)^2}} \qquad 6.1$$

where x_i and y_i are the individual elements of a given data point and n is the number of data points over which correlation is being computed.

The best-correlated microphysical variable with cross-RFD theta gradient was warm rain mixing ratio (correlation = 0.31), which explained about 10% of the cross-RFD theta gradient. A higher warm rain mixing ratio was weakly associated with a stronger cross-RFD theta gradient. This may be related to more rapid evaporation of the small drops characteristic of warm rain, leading to additional cooling relative to a distribution dominated by drops of larger median diameter.

Associations were weak between cross-RFD theta gradient and mixing ratios of frozen particles, most likely because hail, graupel, and frozen drops in most simulations fell out downstream from the updraft and did not significantly affect the RFD region. In a supercell with significant hail or smaller ice particles falling into the RFD region, a stronger cross-RFD theta gradient might be expected due to melting.

2) Microphysical Associations with RFD Westerly Surge Strength

Maximum storm-relative westerly component in the RFD was a more important control on low-level storm evolution than maximum cross-RFD theta gradient. This was expected, since the strength of the RFD westerly surge should be a primary control on mesocyclone cycling and magnitude of vertical vorticity in its vicinity. This feature, hereafter referred to as the ‘westerly surge,’ is a storm-relative surge of westerly momentum moving generally eastward out of the echo appendage region. Moderate correlation was found between maximum RFD westerly component and the number of model output steps with 1000-m updraft magnitude > 10 m s^{-1} (correlation = 0.59), and between maximum RFD westerly component and maximum near-surface vertical vorticity (correlation = 0.51). Storm evolution at the lowest model level typically includes an RFD westerly surge moving eastward within the echo appendage, accompanied by an updraft pulse to its east and development of a region of enhanced vertical vorticity to its north. Thus, these correlations statistically confirm what is typically observed. These processes should also occur in real storms. As a surge of stronger westerly outflow moves into the updraft, there should be an enhanced burst of updraft in response. Also, analogous to flow in a river or in the jetstream, a zone of enhanced cyclonic vertical vorticity should exist on the northern periphery of the stronger flow.

Given these associations, it would be beneficial to identify microphysical contributors to the strength of the RFD westerly surge. Over the entire wind profile parameter space, significant correlations were not found with any particular microphysical variables. The strongest association was with maximum frozen drop mixing ratio (correlation = 0.29). This lack of strong associations seems to be caused by strongly non-linear relationships between updraft evolution and microphysical variables.

Dividing the parameter space into storms with strong vs. weak RFDs, much stronger associations were found. ‘Strong’ RFDs were defined as those having a maximum RFD westerly component of greater than 15 m s^{-1}, while storms with maximum RFD westerly component of 15 m s^{-1} or less were said to have a relatively ‘weak’ RFD. Only six storms had ‘strong’ RFDs, leaving sixteen storms with ‘weak’ RFDs. Among the weak RFD cases, stronger associations emerged with microphysical variables. Strongest correlations were with maximum mixing ratio of hail from frozen drops (0.51; Fig. 6.5a), maximum warm rain mixing ratio (0.56; Fig. 6.5b), and warm rain as a percentage of total maximum rain mixing ratio (0.57; Fig. 6.5c). As mixing ratio of hail increases, cooling due to melting and sublimation should increase, leading to colder outflow (Gilmore et al. 2004a) and presumably a stronger outflow surge as was seen. As warm rain increases in quantity and as a percentage of total rain mixing ratio, the DSD becomes biased toward smaller drops, increasing evaporative potential and leading to colder and stronger outflow (e.g. Srivastava 1987). Thus, both an increasing mixing ratio of warm rain and hail from frozen drops should lead to stronger RFD westerly surges, if these hydrometeors are spatially distributed in such a way that they affect the RFD.

Greatest usefulness of these associations among weaker-RFD cases is theoretically consistent. Processes within supercells, including the formation of the RFD westerly surge, have both dynamical and microphysical components. When the dynamical component is most dominant, RFD surges are likely to be strongest, while a weaker dynamical component should lead to more subtle changes in RFD strength and RFD surges of smaller magnitude. In these weakly-dynamic cases, microphysical effects should be more pronounced. This is what has been observed in this study, given much stronger associations between RFD strength and microphysical variables for storms in which RFD surges are weaker.

c. Relationships between Microphysical Variables and Vertical Vorticity

Vertical vorticity at the lowest model level was highly cyclic and occasionally reached near tornado-strength magnitude. Though with a 250 m grid it is not possible to truly resolve a tornado vortex, the strong concentration of vorticity surrounding the vortex seems well-resolved, and was observed to occur at the location where a tornado would be expected. Here some associations are noted between vertical vorticity and the microphysical variables.

1) Associations with Time to First Strong Vertical Vorticity Maximum

For each simulation at each model output step, maximum vertical vorticity within the mesocyclone at the lowest model level was recorded. The time was recorded at which vertical vorticity first reached at least half the simulation-maximum value. In some cases, the first significant vertical vorticity maximum was the simulation maximum; such cases were not treated differently. The earlier in the simulation this ‘half-maximum’ value was reached, the easier it was thought to be for the supercell to concentrate vertical vorticity at low levels.

Strongest microphysical association with production speed of half-maximum near-surface vertical vorticity was with maximum mixing ratio of hail from frozen drops (correlation = 0.38). Strength of this association remained moderate but was slightly weaker for total maximum hail mixing ratio. This is an expected result. Downdrafts containing ice particles become stronger due to melting and sublimation (e.g. Srivastava et al. 1987), so depending on whether the hail was able to influence the downdraft, may act to produce more rapid surface spin-up and occlusion. This association is not strong enough to allow conclusions, however, and a similar association was not found with graupel or frozen drop mixing ratios. The variables descriptive of storm evolution best-associated with speed of half-maximum vertical vorticity development were simulation-maximum vertical vorticity (correlation = 0.31) and number of model output steps with updraft exceeding 10 m s^{-1} at 1000 m (correlation = 0.54). Thus, whether a storm is able to quickly concentrate vertical vorticity near the surface seems to most depend on whether the storm can quickly develop and sustain a strong updraft column. This association is likely related to vorticity convergence under the updraft and stretching of vertical vorticity within the updraft.

2) Associations with Simulation-Maximum Vertical Vorticity

Simulation-maximum vertical vorticity at the lowest model level was recorded. Though most simulations produced nearly tornado-strength near-surface vertical vorticity, those with larger values are inferred to have been more likely to produce a tornado given much smaller horizontal grid spacing, or to have produced a more significant tornado. Associations were sought at the time of maximum near-surface vertical vorticity between the vorticity values and possible microphysical contributors.

Maximum near-surface vertical vorticity was associated most closely with maximum mixing ratio of hail from frozen drops (correlation = 0.37) and with total maximum hail mixing ratio (correlation = 0.34). Vertical vorticity may be associated with hailfall because storms containing relatively large quantities of hail have colder downdrafts and more pronounced RFD westerly surges, leading to intensification of near-surface vertical vorticity north of the westerly surge. Rain from melting and shedding were also moderately correlated with maximum near-surface vertical vorticity, though these correlations were of opposite sign. Overall, predictability of simulation-maximum near-surface vertical vorticity was substantially less from a microphysical perspective.

3) Associations with Summed Vertical Vorticity

Maximum vertical vorticity in association with the mesocyclone was recorded for each of the twenty-one model output steps in each simulation, and these values were summed to yield simulation-total summed vertical vorticity (hereafter summed vorticity). Because it contains information about evolution of maximum near-surface vertical vorticity in the mesocyclone region through time, this index is thought to represent how easily and repeatably the supercell is able to concentrate vertical vorticity at low levels.

Summed vorticity was found to be most strongly associated with maximum warm rain mixing ratio and maximum warm rain mixing ratio as a percentage of total maximum rain mixing ratios (correlation = 0.36 for each). Hail from frozen drops was also moderately associated (correlation = 0.32). These associations may be related to downdraft strength. Increased warm rain leads to colder area-averaged outflow via greater evaporation, while more hail should also cause colder downdrafts through melting and sublimation. Though summed vorticity was not found to depend on maximum cross-RFD theta gradient, it was associated with the maximum RFD westerly component (correlation = 0.34) and with the number of model output steps containing updraft > 10 m s^{-1} (correlation = 0.40). Thus, a storm's ability to repeatably concentrate vertical vorticity near the surface may depend on the presence of a vorticity-rich zone to the north of an RFD westerly surge, and a strong updraft overhead to produce convergence and stretching of this vorticity. Notably, maximum mixing ratios of rain from melting and shedding seemed much less significant than maximum mixing ratio of warm rain.

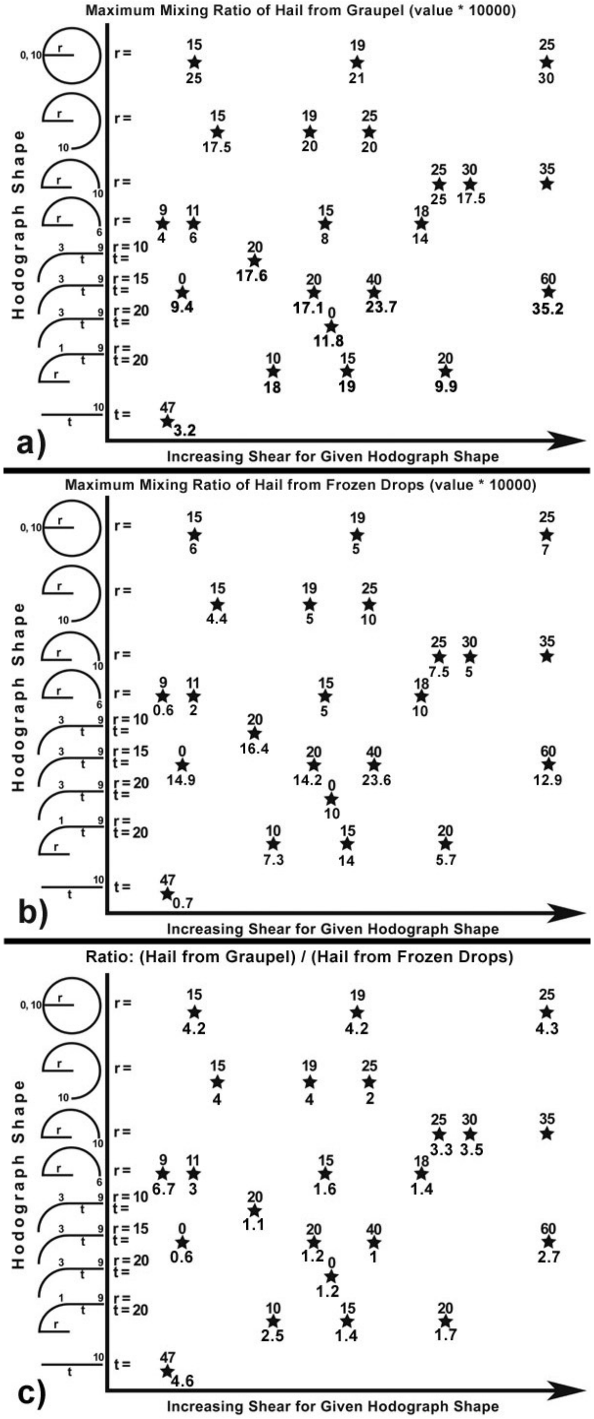
Maximum Mixing Ratio of Hail from Graupel (value * 10000)

Maximum Mixing Ratio of Hail from Frozen Drops (value * 10000)

Ratio: (Hail from Graupel) / (Hail from Frozen Drops)

Figure 6.1: Number below each star represents maximum mixing ratios at 1000 m of a) hail from graupel and b) hail from frozen drops, where values have units of g kg^{-1} times 10. c) represents maximum mixing ratio of hail from graupel divided by that of hail from frozen drops. Each star represents one simulation, as described in Chapter 4.

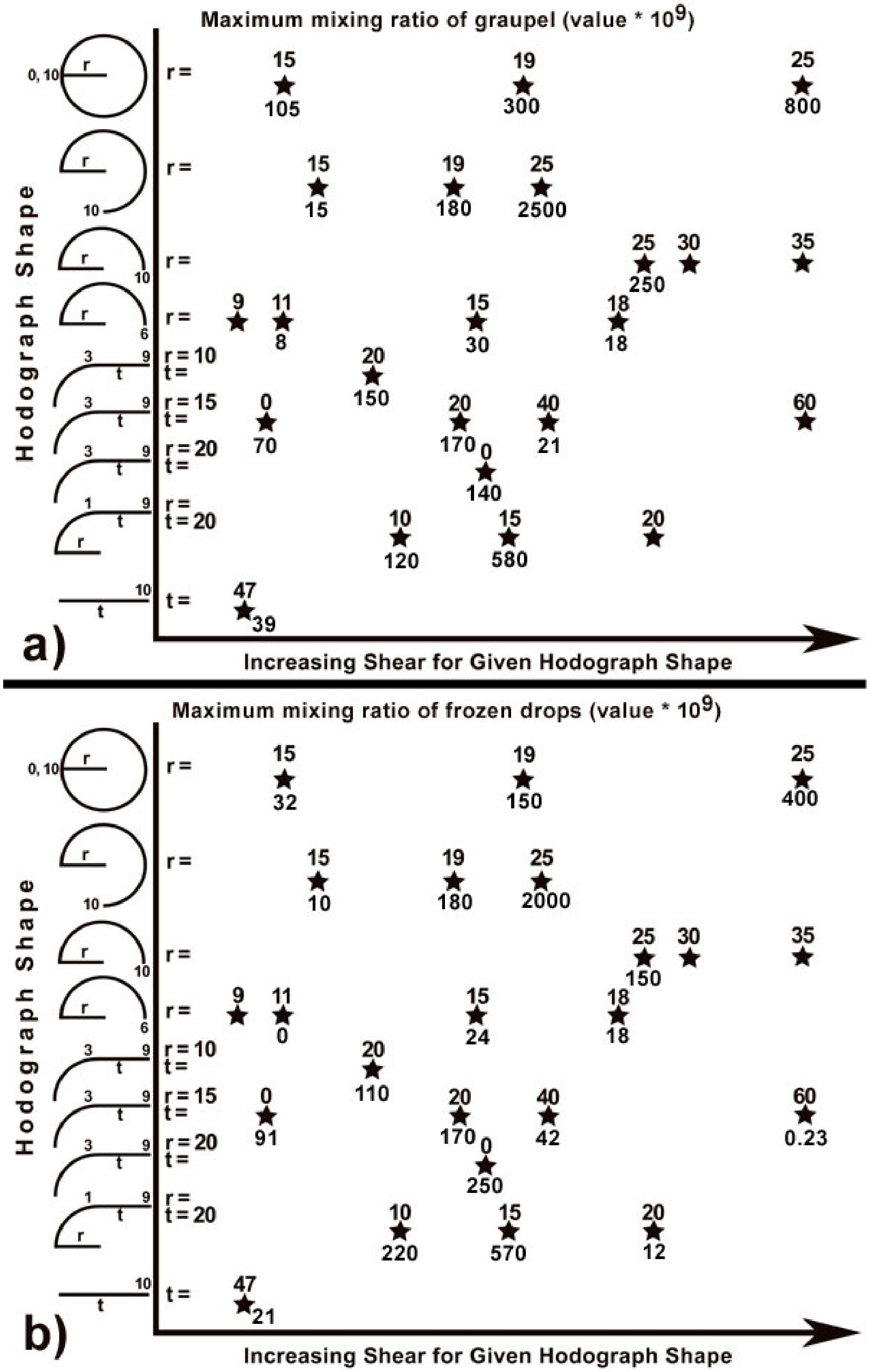

Figure 6.2: As in Fig. 6.1, except numbers below the stars here represent a) maximum graupel mixing ratio and b) maximum mixing ratio of frozen drops, each at 1000 m and in units of mg kg^{-1} divided by 1000 for scale.

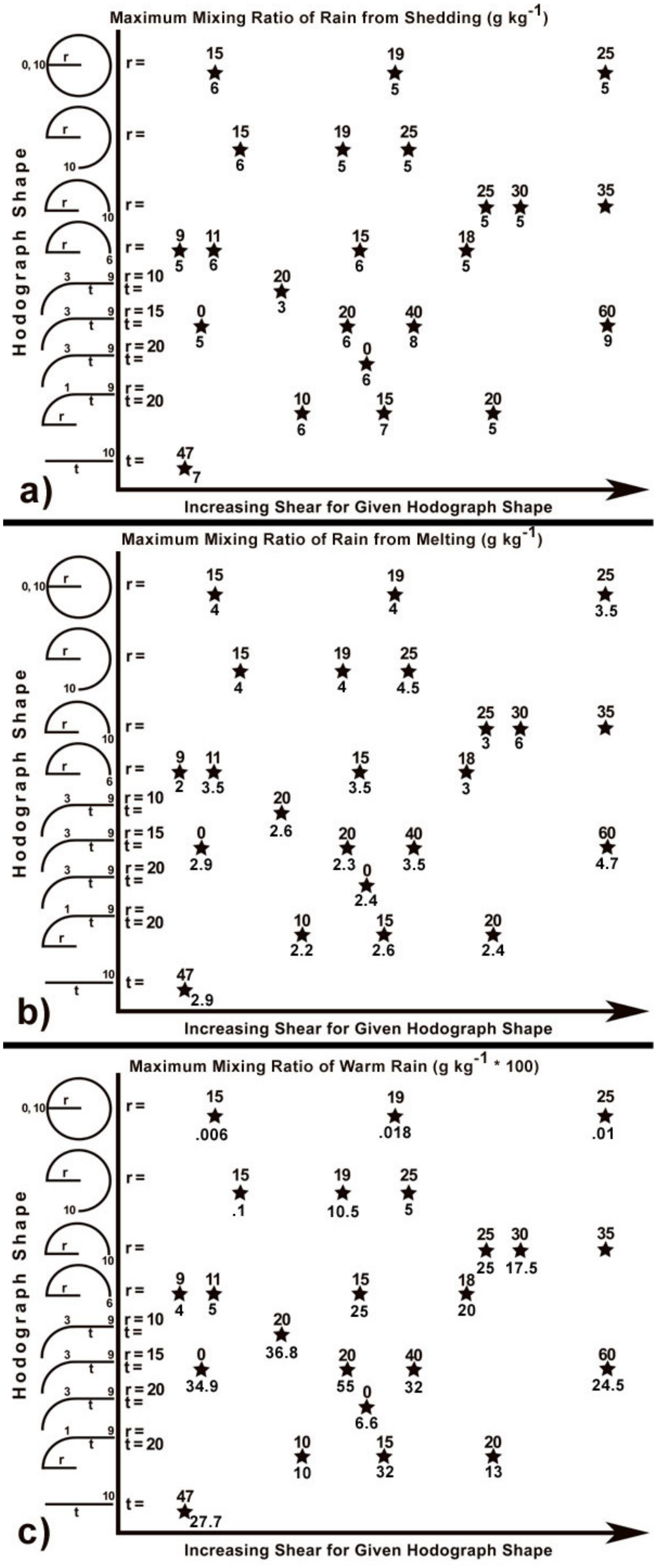

Maximum Mixing Ratio of Rain from Shedding (g kg^{-1})
Hodograph Shape
0, 10
r
10
6
3
9
t
1
r =
r = 10
t =
r = 15
t =
r = 20
t =
r =
t = 20
t =
15 6
19 5
25 5
15 6
19 5
25 5
25 5
30 5
35
9 5
11 6
15 6
18 5
20 3
0 5
20 6
40 8
60 9
0 6
10 6
15 7
20 5
47 7
a)
Increasing Shear for Given Hodograph Shape
Maximum Mixing Ratio of Rain from Melting (g kg^{-1})
15 4
19 4
25 3.5
15 4
19 4
25 4.5
25 3
30 6
35
9 2
11 3.5
15 3.5
18 3
20 2.6
0 2.9
20 2.3
40 3.5
60 4.7
0 2.4
10 2.2
15 2.6
20 2.4
47 2.9
b)
Increasing Shear for Given Hodograph Shape
Maximum Mixing Ratio of Warm Rain (g kg^{-1} * 100)
15 .006
19 .018
25 .01
15 .1
19 10.5
25 5
25 25
30 17.5
35
9 4
11 5
15 25
18 20
20 36.8
0 34.9
20 55
40 32
60 24.5
0 6.6
10 10
15 32
20 13
47 27.7
c)
Increasing Shear for Given Hodograph Shape

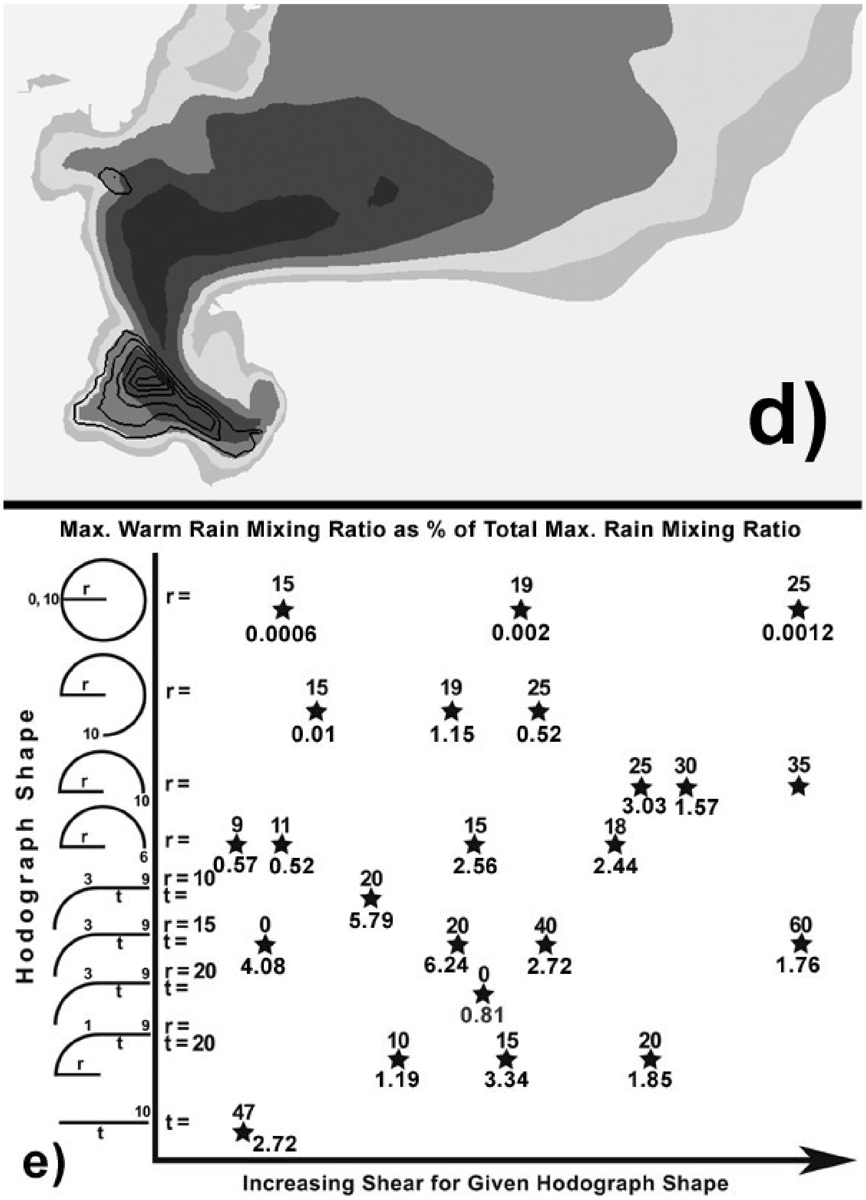

Figure 6.3: As in Figs. 6.1 and 6.2, except here the numbers below the stars represent a) maximum mixing ratio of rain from shedding at 1000 m, b) maximum mixing ratio of rain from melting at 1000 m, c) maximum warm rain mixing ratio at 1000 m, and e) maximum warm rain mixing ratio as a percentage of the total maximum rain mixing ratios at 1000 m. d) shows a typical warm rain distribution, where contours represent warm rain overlaid on grayscale-filled reflectivity factor. This example came from simulation 17 at 6900 s past model initialization.

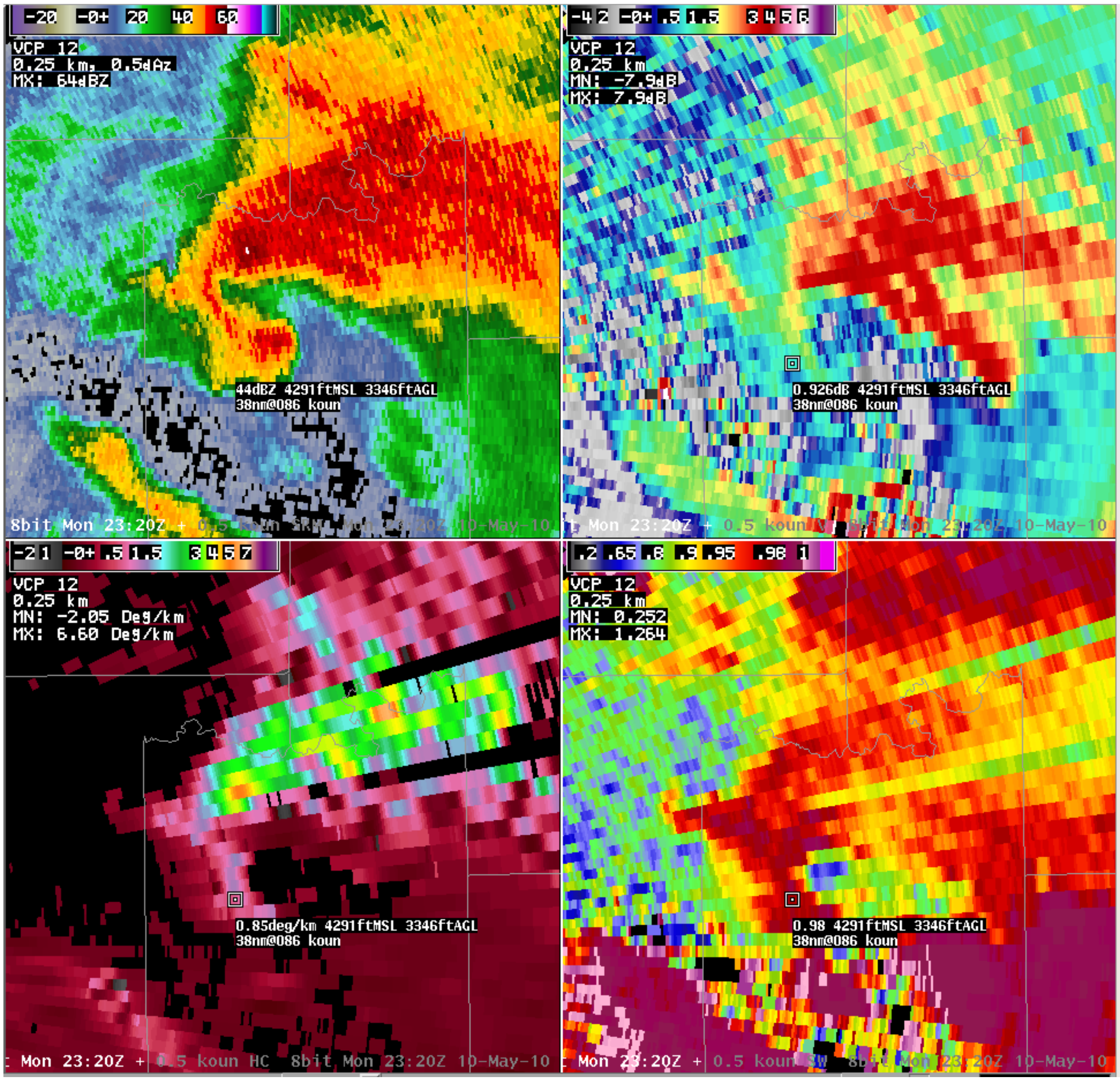

Figure 6.4: Polarimetric radar variables, displayed using AWIPS, from 23:20 UTC on 10 May 2010. Clockwise from upper left are reflectivity factor, differential reflectivity, correlation coefficient, and specific differential phase. The square shows the location of a sampled pixel, and the readout below gives the value of the specific polarimetric variable. Storm is located over northern Seminole County, Oklahoma, and was producing a large tornado in Seminole, Oklahoma, at this time.

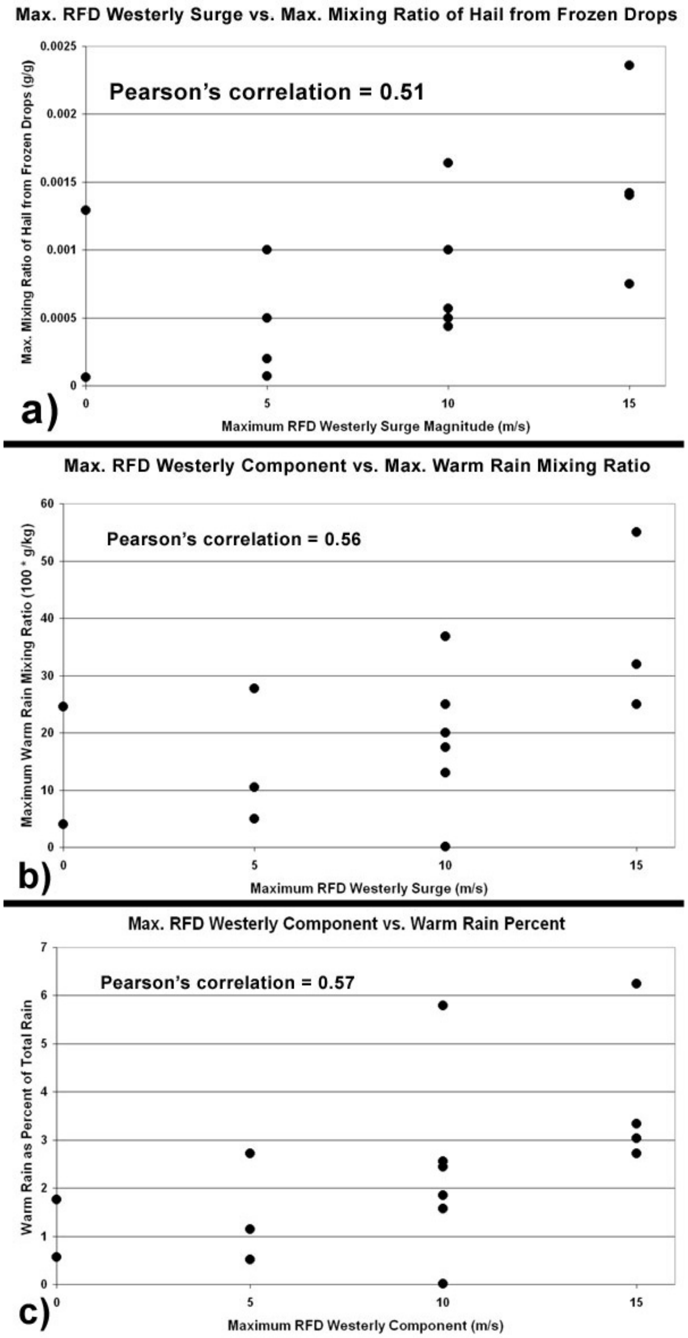

Figure 6.5: Maximum westerly component magnitude within the RFD westerly surge, plotted against a) maximum mixing ratio of hail from frozen drops, b) maximum warm rain mixing ratio, and c) maximum warm rain mixing ratio as a percentage of total maximum rain mixing ratios. Each datapoint represents the result from one simulation at its time of maximum near-surface vertical vorticity.

7. Effects of Mid- and Upper-Level Drying on Supercell Evolution

Given the differences in mesocyclone evolution and microphysical distributions described in previous chapters, another logical line of inquiry is to explore such differences given changes to the environmental moisture profile. Often storms will be observed to move into a region with different moisture characteristics than where they formed, and this environmental change often produces a change in storm character. This is, therefore, a very operationally-relevant question. In this research, environmental drying was explored as described above in Terminology and Methodology. Microphysical distributions were found to vary substantially between simulations identical except for choice of moisture profile. Similarly to what has been done in prior chapters, effects of microphysical variations on low-level supercell evolution are investigated, this time in a time series sense.

a. Spatial and Temporal Hydrometeor Distributions

First, variations of hydrometeor distributions are presented for the simulations with dried profiles.

1) Distributions of Hail Variables

Hail from graupel (HG) and hail from frozen drops (HFD) occurred in generally the same location in all simulated storms, just downwind from the updraft region. The most significant HFD maximum was often located at the upwind side of the precipitation core, nearest the updraft. HG had a slight downstream bias compared to HFD. This slightly downstream bias likely reflects the average downstream location of graupel compared to frozen drops, since graupel must grow via accretion of supercooled droplets.

The four ice-inclusive simulations produced fairly similar evolution of HFD content (Fig. 7.1). All began 3000 s past simulation initialization with a maximum value around 1.25 g kg^{-1}. In all simulations, this value dropped off rapidly toward 0.5 g kg^{-1} by 3600 s, then increased to 1 – 1.5 g kg^{-1}. After this point, maximum values of HFD diverged between simulations, though a general decrease was present to about 5100 s, followed by an increase which peaked around 6000 s, and a decrease thereafter. The cyclic nature of hail content seemed consistent with observations of real supercells, which often produce hailfall in distinct bursts.

Average maximum mixing ratio of HFD differed by only 15% between simulations. Across the spectrum of simulations, hail content was slightly greater when both mid and upper levels were dried, opposite the pattern seen for smaller ice particles. During the first peak in HFD content at 1000 m (~4500 s – 4800 s), storms with only midlevel drying contained more hail. During the second hail content peak, however (~5700 s – 6300 s), storms with deep-layer drying contained the most hail. It is possible that storms with a deeper layer of drying may require more time to become sufficiently microphysically mature to produce substantial hail, as evaporation or sublimation may have more significant impacts on the mass balance of hydrometeors. Depth of drying was again found to be more important than magnitude of drying.

Differences were greater between the HG time series (Fig. 7.2). Starting at 3000 s in all simulations, HG had a value around 1 g kg^{-1}, then increased in all simulations through about 4500 s. From this point, however, values of HG diverged between the simulations. By about 5700 s, all simulations had settled toward an average maximum value of 2 – 2.5 g kg^{-1}, where they tended to persist. All simulations exhibited cyclic bursts of greater hail production, as often seen in real supercells.

Maximum HG content averaged over all time steps with good data was around 2 g kg^{-1}, greater than for HFD (Fig. 7.2). Values ranged from about 1.7 g kg^{-1} in the case with significant midlevel drying, to 2.2 g kg^{-1} in the case with only moderate deep-layer drying. Average values were lower when more moisture was removed from the column, possibly due to less supercooled droplets surviving to produce hail via graupel. Average values seemed less dependent on the depth over which drying was applied.

Simulations with only midlevel drying often had lower HG values during the first ~5400 s of simulation, with comparable values thereafter. A reason for this pattern is not clear, but it may be related to greater evaporative cooling in the column when both mid and upper levels are dried. A cooler column would allow greater hailstone mass to survive to the 1000 m level. The importance of this cooling effect should become less as the storm ages and creates its own environment, possibly explaining the comparable values after ~5400 s. When significant midlevel drying was applied, HG content was quite low through the first 5700 s. This suggests that in an environment with significant midlevel dry air, the graupel distribution may take longer to become mature. This may limit the production of HG until later in the storm's lifecycle. Once storms are well-established, the presence of substantial midlevel dry air no longer seems important.

2) Distributions of Graupel and Frozen Drops

Frozen drops and graupel were spatially located similarly regardless of modifications to the moisture profile. Frozen drops at 1000 m were typically found just downwind from the updraft region, within the precipitation core. This was consistent with liquid drops forming in the updraft, freezing, being advected by the mean wind, and falling out downstream. Frozen drops were always observed to melt before reaching the lowest model level, and at 3 km elevation wrapped around the west side of the updraft. Graupel was typically located a bit downstream from the frozen drop maximum (typically to its northeast). This is likely the case because, in the SAM, graupel forms when an ice crystal accretes supercooled drops. The accretion process takes time, so the wind would have advected the growing graupel particles farther from the updraft. Also, ice crystals are low-mass particles relative to raindrops, so would advect farther. Thus the majority of graupel fallout should be expected a bit downstream from where the majority of frozen drops fall.

Modest similarities in frozen drop mixing ratio were present in time series from the four ice-inclusive simulations (Fig. 7.3). In all simulations, maximum mixing ratio of frozen drops was around 0.1 mg kg^{-1} though 3900 s, then increased by a factor of two to five over the next 5 min. Values by 4800 s – 5100 s had again dropped to their earlier levels. Past about 5400 s variability was higher between simulations, though most showed a series of similar varying-amplitude oscillations. The simulation with significant midlevel drying was most different, with a series of large frozen drop maxima.

Average maximum frozen drop mixing ratio varied from 0.081 mg kg^{-1} in the simulation with significant deep-layer drying to 0.166 mg kg^{-1} in the simulation with significant drying at only midlevels. Lower frozen drop content, therefore, may be attributable to sublimation of ice particles as they leave the saturated updraft region. Rain from melting and shedding had relatively high average values with this moisture profile. Thus they either were not freezing or were sublimating by the time they reached 1000 m. When only midlevels were dried, rain from melting and shedding had relatively low mixing ratios, so it was unclear why frozen drops were so much more common.

Further patterns were observed in the time series of maximum frozen drop mixing ratio. When only midlevels were dried, resultant storms contained maximum frozen drop mixing ratios approximately twice as high during the initial peak (4500 – 4800 s). During the rest of the simulation, values were more comparable with those in other simulations, though a few exceptionally high peaks occurred given only midlevel drying. With a shallower dry layer, evaporation of freezing liquid drops and sublimation of ice particles would be less significant, so it makes sense that frozen drop mixing ratios were higher. Also, ice particles would be more likely to reach midlevels since the upper levels were moister. Given drier midlevel air, more liquid drops could possibly evaporate, cooling the layer and allowing more ice-phase particles to survive. Frozen drop mixing ratio did not appear very sensitive to the magnitude of drying, but rather to the depth over which drying had been applied.

Maximum graupel mixing ratio was much more variable than for frozen drops (Fig. 7.4). All simulations exhibited similar maximum graupel mixing ratio values through 3900 s, then diverged widely. From 4200 s – 5400 s values increased by four to eight times, and were dissimilar between simulations. After 5400 s, values again became remarkably similar through 6600 s, with lesser divergence until the end of each simulation. A striking increase in graupel mixing ratio starting around 4200 s was also seen with frozen drops.

Lowest average maximum graupel mixing ratio was again seen when the deep layer was substantially dried. Sublimation may be contributing as for frozen drops, though evaporation of the required supercooled drops may be more important. When the deep layer was only moderately dried, average graupel content was very low. The simulations with only midlevel drying averaged 60% more graupel content. Thus, as for frozen drops, the depth of drying seems to be more important than the magnitude of drying, likely by influencing the amount of supercooled droplet evaporation.

3) Distributions of Rain Variables

Rain from melting (RM) and shedding (RS) occurred throughout the precipitation core of each simulated supercell. RM often had two maxima. One was just north of the echo appendage region, and often contained the maximum mixing ratio of RM at a given time step. The other occurred well north of the mesocyclone, in the central portion of the region enclosed by the maximum reflectivity contour. The first maximum may represent the melting of ice particles near the updraft, while the second likely represents a preferred fallout region for graupel particles in this wind regime. Two maxima in the RS distribution, located in the same locations, likely represent shedding from hailstones as they fall out around the updraft and droplets shed from melting graupel.

The four ice-inclusive simulations did not show strong similarities overall when looking at temporal evolution of the RM field (Fig. 7.5). Values began around 2.5 – 3 g kg^{-1}, though the distribution was bimodal. In most simulations, content of RM seemed approximately cyclic. This is probably related to the roughly cyclic production of hail and graupel in these storms. Quantity of RM depended strongly on where drying was applied, and less on the magnitude of drying—RM content was higher when a deeper layer was dried. This pattern is not readily explained, as quantities of both graupel and frozen drops were less when the deep layer was dried. Possibly, a drier environment would lead to smaller ice particles, which would melt more readily into raindrops.

Similarities and differences were generally much less pronounced in the time series for RS (Fig. 7.6). In all simulations, maximum RS mixing ratios started out at 3.5 – 4.5 g kg^{-1}, and tended to remain in the 4 – 5 g kg^{-1} range. Past 6900 s, each simulation for which there was good data showed an increasing RS trend, with values climbing above 5 g kg^{-1}. A reason for this increasing trend is unclear, but one factor may be increasing supercell microphysical maturity—greater numbers of ice particles may be present, allowing more opportunities for shedding.

Average values of maximum RS only varied by about 12% over the four simulations. The only value which seemed dissimilar from the others occurred when substantial midlevel drying was applied. Significant drying of midlevels may slow the growth of ice particles, so less would be available to melt. Also, once liquid was shed, it may evaporate more readily in a dry midlevel environment. Cooler temperatures associated with evaporation in the drier environment may decrease the amount of shedding. Overall, though, the difference between simulations was not substantial.

Warm rain (WR) occurred in a specific and repeatable location across all simulations, on the west and southwest side of the echo appendage and just west of where the RFD might be expected to originate. Regions of higher reflectivity extending westward from the appendage were often found to be strongly dominated by WR. This maximum was typically just west of a strong maximum in the field of RS. WR may be present on the west side of the appendage, where particles are beginning their ascent in the updraft, because seeding by ice particles is disfavored on the updraft's upwind side. This distribution should be less repeatable, and the amount of WR less, in cases where upshear storms spread ice crystals over a large area.

The four simulations appeared to have fairly similar WR evolution (Fig. 7.7). Maximum WR mixing ratio started around 0.3 g kg^{-1}, then the WR mixing ratio underwent a series of maxima and minima which were slightly different in each simulation. Overall, though, the broad-scale pattern was about the same, with four to five maxima in the WR time series, punctuated by deep minima when WR content dropped by 50% - 75%. These fluctuations were more significant than those in the fields of rain from melting or shedding, suggesting a more cyclic process by which WR is produced or favored in these storms. This more cyclic nature also suggests WR may be more closely associated with near-surface vertical vorticity.

Average maximum values of WR showed a bimodal distribution. Values in the two simulations with only midlevel drying had an average value of 0.26 g kg^{-1}, and this value increased to 0.32 g kg^{-1} in the two simulations with deep-layer drying. The lowest value occurred when significant drying was applied at midlevels. Greatest average WR content occurred when moderate drying was applied at mid and upper levels. Significant drying at any level appears to be unfavorable for WR. Given the small droplets dominant in this type of rain distribution, this pattern is not surprising—any significantly dry layers should more readily evaporate the drizzle droplets required for WR formation.

Patterns seen when looking at WR time series were generally weak. In simulations with modest drying, four to five temporal maxima were seen in the WR mixing ratio field. When the deep layer was dried, five maxima were typically seen. More rapid cycling of the WR field with a deeper layer of drying may be related to a higher evaporation rate, though these simulations also produced the highest average WR values. In the two simulations with significant drying, WR content seemed to cycle together, and was generally higher than in the moderate-drying cases over first 900 s – 1200 s. Cases with only midlevel drying also seemed to cycle somewhat together, though magnitude of the maxima varied substantially. Thus, average WR content over time appeared most sensitive to depth of the layer over which drying occurred—storms with a dry environment at mid and upper levels may produce more WR than those with moister environments.

b. Mesocyclone Evolution with Environmental Drying

Variations to the environmental moisture profile were found to alter mode of mesocyclone cycling. It may be valuable to understand how moisture variations may affect mesocyclone behavior, as this understanding may lead to greater anticipation of how supercell behavior may change as a storm moves into an environment with different moisture characteristics. In this section are presented some of the noted changes in mesocyclone behavior for dried environments. Modes of cycling are defined as described above in Terminology and Methodology.

1) Variability in Mesocyclone Evolution with Drying

Time to the first significant RFD westerly surge, in the four ice-inclusive simulations, was closely tied to the vertical moisture profile. In simulations with significant moisture removed, the first meaningful RFD westerly surge occurred within the first 1 hr 5 min. When only moderate moisture was removed, this first surge was delayed an additional 5 – 15 min. This pattern is related to the amount of potential evaporative cooling. When the environment is dried, greater hydrometeor evaporation and associated cooling should lead to a cooler column, favoring stronger downdrafts. If stronger downdrafts arrive at the surface, mesocyclone evolution should proceed more quickly, including more rapid progression of the RFD westerly surge. In cases with drier environments and stronger downdrafts, then, an RFD surge and corresponding surface vertical vorticity maximum may be expected to develop more rapidly than if the environment were more moist. This expectation does not account for dynamical factors which may affect storm evolution.

The ice-inclusive simulations showed dominantly non-occluding cyclic mesocyclone evolution. This was clearly the preferred mode for both moister cases and for the case with substantial deep-layer drying. When midlevels were substantially dried, occluding cyclic and non-occluding cyclic behavior were each about equally dominant. It is possible that in some cases with significant drying, downdrafts are stronger and more likely to wrap all the way around the mesocyclone. Thus, in very dry environments, occluding cyclic mesocyclone behavior may be more frequent. These moisture variations would need to be applied across a broad spectrum of wind profiles before more certain conclusions could be drawn.

Mesocyclone evolution in the liquid-only simulations was more variable and generally dissimilar from that in ice-inclusive simulations. When the environment was significantly dried, non-occluding cyclic behavior was uncommon. When midlevels were significantly dried, the resultant liquid-only storm exhibited mostly steady non-cycling behavior, transitioning to a short-lived non-occluding cyclic mode prior to the entire system becoming a squall line. When the deep layer was significantly dried, the liquid-only storm was dominated by occluding cyclic behavior, though mesocyclone evolution was difficult to follow through the entire simulation. Tendencies toward occluding behavior and a transition to linearity may be expected in liquid-only simulations, since outflow tends to be colder and RFD westerly surges are stronger, as shown in prior chapters.

Comparisons were also made between the liquid and ice control simulations. The dried-profile simulations did not overall strongly resemble the control simulations for this hodograph. The control ice-inclusive simulation was dominated by occluding cyclic behavior, with one non-occluding cyclic event. When moisture was decreased, non-occluding cyclic behavior became dominant, though occluding cyclic behavior also occurred occasionally. None of the ice-inclusive simulations had non-cyclic mesocyclones. It is unknown why non-occluding cyclic behavior was more dominant when deep-layer moisture was decreased.

The control liquid-only simulation exhibited occluding cyclic behavior much of the time, but transitioned to non-occluding cyclic behavior toward the end of the simulation. When the environment was dried, mesocyclone evolution was more difficult to follow but tended toward more non-occluding cyclic behavior. Differences were most pronounced when significant drying was applied. With significant midlevel drying, a period of steady non-cyclic behavior was unusual, but even this simulation tended toward non-occluding cyclic behavior before ending. The resultant storm with significant deep-layer drying tended to have a mostly occluding cyclic mesocyclone. When moisture was only moderately reduced, non-occluding cyclic evolution was always observed.

2) Mesocyclone Evolution and Microphysical Distributions

In most ice-inclusive simulations, the mesocyclone cycled in a non-occluding cyclic manner. The exception occurred when significant drying was applied to midlevels, in which occluding and non-occluding cyclic behavior were observed. The goal of following analysis is to suggest a microphysical basis for this behavioral difference.

Average maximum near-surface vertical vorticity was lowest when midlevels were dried significantly, suggesting less-frequent RFD surges. Vertical vorticity in this simulation reached an initial weak maximum at 3900 s, dropped to a minimum at 5100 s, and began an increase between 5700 s and 6000 s which led to the simulation’s strongest vorticity maximum around 7200 s (Fig. 7.8). Neither frozen drop nor graupel content seemed related to mesocyclone evolution in this simulation, though average maximum graupel mixing ratio was the highest seen in any simulation. Hail variables likewise did not seem related to mesocyclone evolution. RS and WR both had lower average maximum values than the other three simulations. The decrease was 6% below the next-lowest value for RS and nearly 12% below the next-lowest value for WR. Possible associations between these rain variables and mesocyclone evolution were sought.

RS exhibited large peaks around 4200 s and 5700 s, with a deep minimum at 4800 s (Fig. 7.8). The minimum occurred just prior to the pronounced vertical vorticity minimum, while the peak at 5700 s occurred a few minutes prior to the storm’s most significant increase in vertical vorticity. The drop size distribution of RS is likely dominated by fairly small drops, which would evaporate relatively quickly and possibly cause a burst of cooler air to reach the surface, a pattern associated with RFD intensification. It is possible that microphysical effects become more important as a supercell becomes more microphysically mature, since early in its life dynamics may be a relatively more important influence on storm structure and evolution.

Maximum WR content was very cyclic in this simulated supercell, with five distinct peaks. Thus, little relationship with vertical vorticity was discernible. WR was not especially prevalent once vertical vorticity began to increase, nor was there a lack of WR when vertical vorticity was weak. From these observations, it appears that WR may not be as important to mesocyclone evolution as RS. This may be because RS typically has a much greater mixing ratio than WR, so the greater liquid content of the RS may overwhelm effects of WR evaporation, though both are dominated by small drops.

The final conclusion of this analysis may be that microphysical effects are unclear in determining mesocyclone evolution, and that microphysical controls are of varying importance under varying circumstances. This study would also need to be carried out using many more wind profiles before a strong conclusion could be reached. RS showed some value in determining mesocyclone behavior once the simulated storm had become microphysically mature. It is suggested from this very small sample of simulations that storms with greater graupel content and lesser content of WR and RS at 1000 m may tend toward occluding cyclic behavior.

c. Microphysical Controls on Near-Surface Vertical Vorticity

Time series including vertical vorticity and the microphysical variables were created for each simulation. Patterns were sought, such as simultaneous changes in the variables, or lagged but possibly related changes.

Maximum mixing ratio of frozen drops was not found to be related to vertical vorticity evolution. In several simulations, peaks in graupel content were followed 5 – 10 min later by substantial increases in near-surface vertical vorticity, though a definite relationship was not clear. The repeatability of this pattern across a few simulations, however, makes it possible that a burst of graupel could aid a westerly RFD surge, and thus indirectly increase vertical vorticity near the surface.

Though HG did not appear related to mesocyclone evolution, HFD showed a promising pattern. In the simulation with moderate midlevel drying, maximum mixing ratio of hail from frozen drops varied cyclically, with four distinct peaks (Fig. 7.9). In each case, a maximum in hail content was followed 5 – 10 min later by an increase in near-surface vertical vorticity. Thus, maxima in the vorticity field typically occurred between maxima in hailfall. It is likely that hailfall produced an intensification of the

RFD westerly surge, leading to surface vorticity intensification. This pattern closely matches a pattern observed in real supercells (e.g. Browning 1965, Van Den Broeke et al. 2008). When midlevels were significantly dried, HFD content was dominated by a large burst from 4200 s – 5100 s, which was followed by a significant intensification of the vertical vorticity field 10 – 15 min later. Little pattern was clear when a deeper layer was moderately dried, as HFD content showed less cyclicality though vorticity underwent multiple sharp maxima. When a deep layer was substantially dried, the hailfall pattern was similar, though the largest hailfall burst preceded by 5 – 10 min the most rapid increase of vertical vorticity. To a large extent in several simulations, bursts of HFD seemed to precede significant vertical vorticity increases by 5 – 10 min. This pattern seemed most established when only midlevels were dried. Perhaps when a deep layer is dried, evaporative cooling becomes of greater importance relative to hailfall. When the column is moister and evaporation is lessened, hailfall should be more important via the relatively more important role of cooling due to melting.

RM was not well-associated with mesocyclone behavior. RS exhibited more cyclic behavior, but still did not appear to be strongly related to vertical vorticity. WR was the most variable rain type, allowing a more robust comparison with the low-level vertical vorticity field. When midlevels were moderately dried, large bursts of WR were observed at 4800 s and 6300 s. These were followed 5 – 10 min later by significant increases in vertical vorticity (Fig. 7.10). With significant midlevel drying, WR was much more rapidly cyclic, and any relationship with vertical vorticity was less clear. Two of the WR maxima, however, preceded vorticity maxima. Little or no relationship seemed to exist when a deep layer was moderately dried. When the deep layer was significantly dried, however, all three WR maxima were associated with increasing vertical vorticity. An association would make sense—the drop distribution in WR is biased toward small drops, so a greater WR content may lead to more evaporative cooling and thus to a stronger RFD westerly surge. This mechanism appears to be of varying importance from storm to storm, with the mechanism possibly more important when the environment is drier and thus when evaporation can occur more readily. The effectiveness of this mechanism is also likely to vary depending on where the WR is occurring with respect to the RFD formation region, and possibly depending on specific dynamical and other microphysical influences from nearby storms.

Beyond the relationships between near-surface vertical vorticity and the microphysical variables conjectured above, dynamical effects are also likely playing an important role. It is possible in some cases that broader processes related to the dynamics of the storm may be causing both the observed precipitation fallout and vorticity increase. For instance, updraft collapse has been observed around the time of tornadogenesis. This collapse could cause a fall of hail in the minutes prior to tornadogenesis. Then, it is unclear how much of the subsequent vorticity intensification is related to this microphysical change, and how much is tied to the larger-scale supercell dynamics which caused the updraft collapse. Testing this will be difficult, but is a necessary next step. Perhaps a vorticity budget analysis on a small temporal scale would help determine the source of vorticity for the tornado cyclone and tornado.

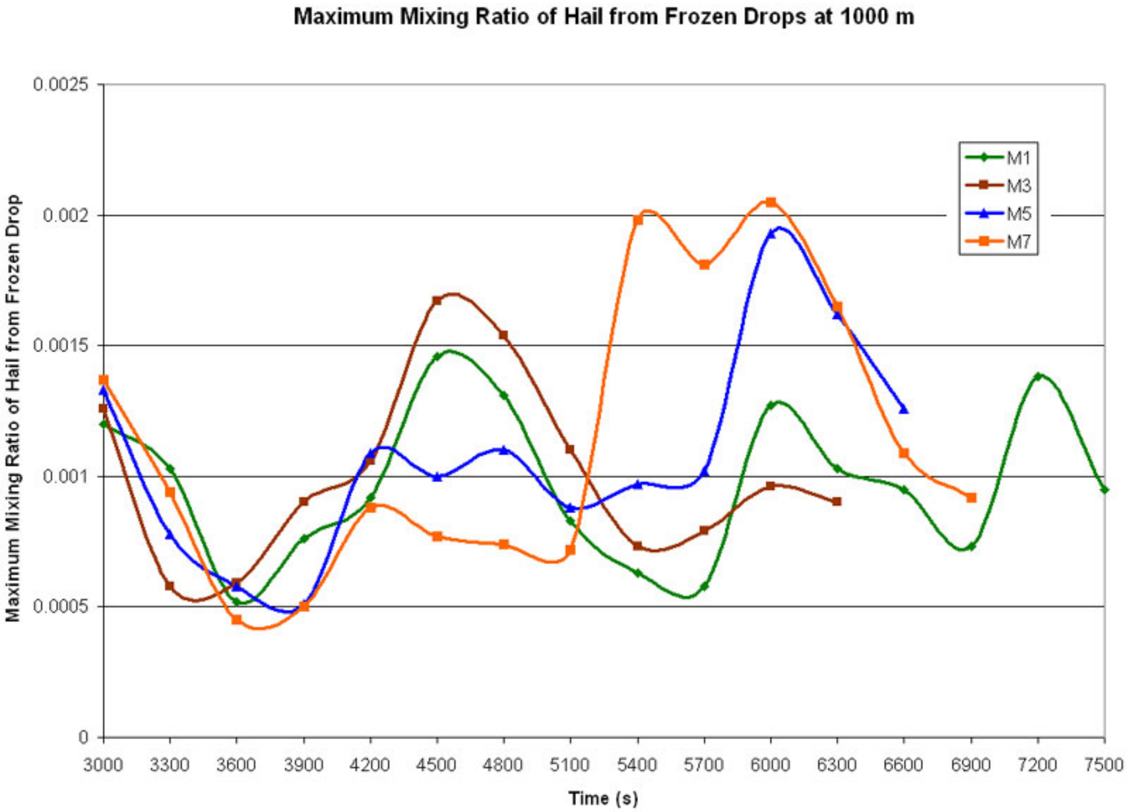

Figure 7.1: Time series of maximum mixing ratio of hail from frozen drops for simulation 1 (moderate midlevel drying, green diamonds), simulation 3 (significant midlevel drying, brown squares), simulation 5 (moderate deep-layer drying, blue triangles), and simulation 7 (significant deep-layer drying, orange squares). Time series run from 3000 s – 7500 s past model initialization. Values of maximum hail from frozen drop mixing ratio are in kg kg^{-1}.

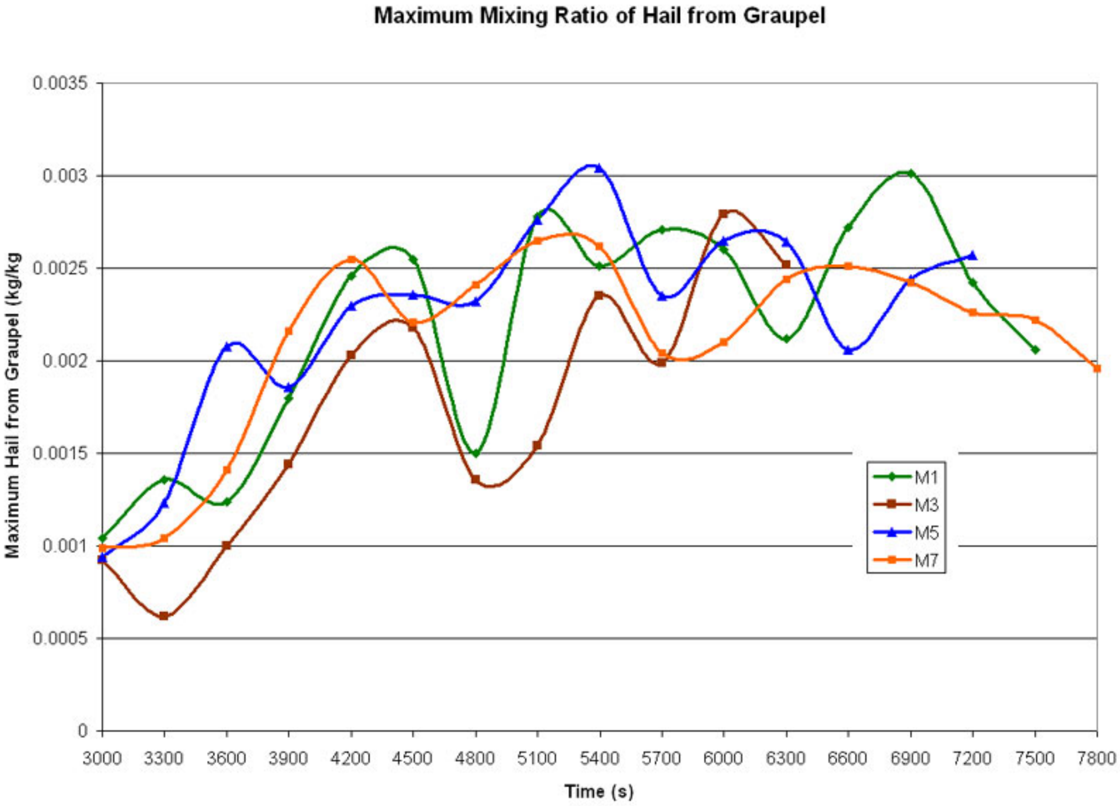

Figure 7.2: Time series of maximum mixing ratio of hail from graupel for the four ice-inclusive simulations, with colors and symbols as described in Figure 7.1. Time series run from 3000 s – 7800 s past model initialization. Values of maximum hail from graupel mixing ratio are in kg kg^{-1}.

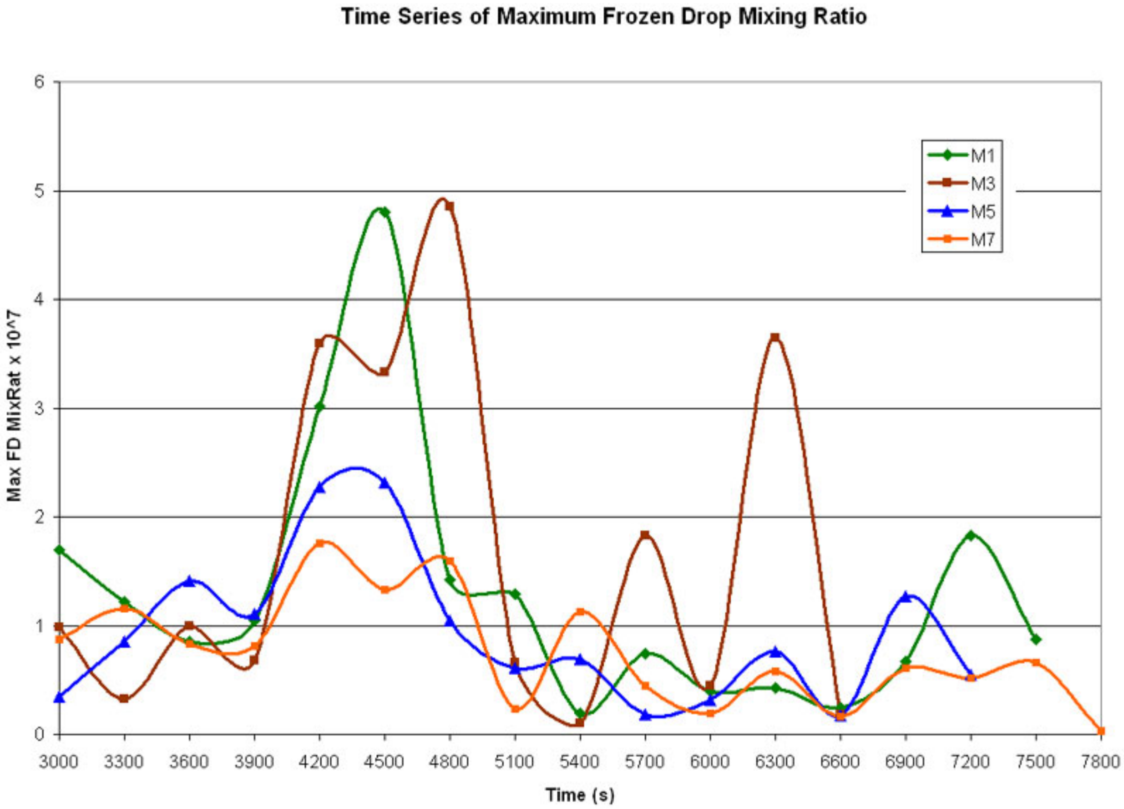

Figure 7.3: Time series of maximum mixing ratio of frozen drops for the four ice-inclusive simulations, with colors and symbols as described in Figure 7.1. Time series run from 3000 s – 7800 s past model initialization. Values of maximum frozen drop mixing ratio are multiplied by 10^7 for scaling.

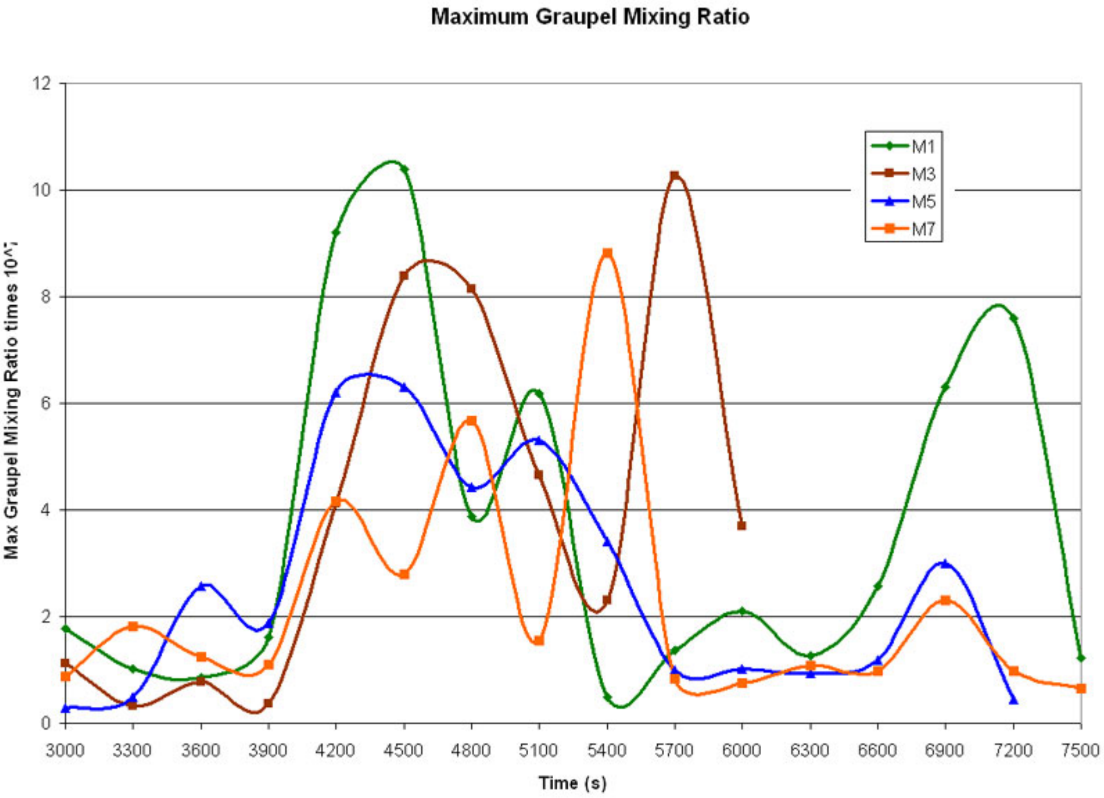

Figure 7.4: Time series of maximum mixing ratio of graupel for the four ice-inclusive simulations, with colors and symbols as described in Figure 7.1. Time series run from 3000 s – 7500 s past model initialization. Values of maximum graupel mixing ratio are multiplied by 10^7 for scaling.

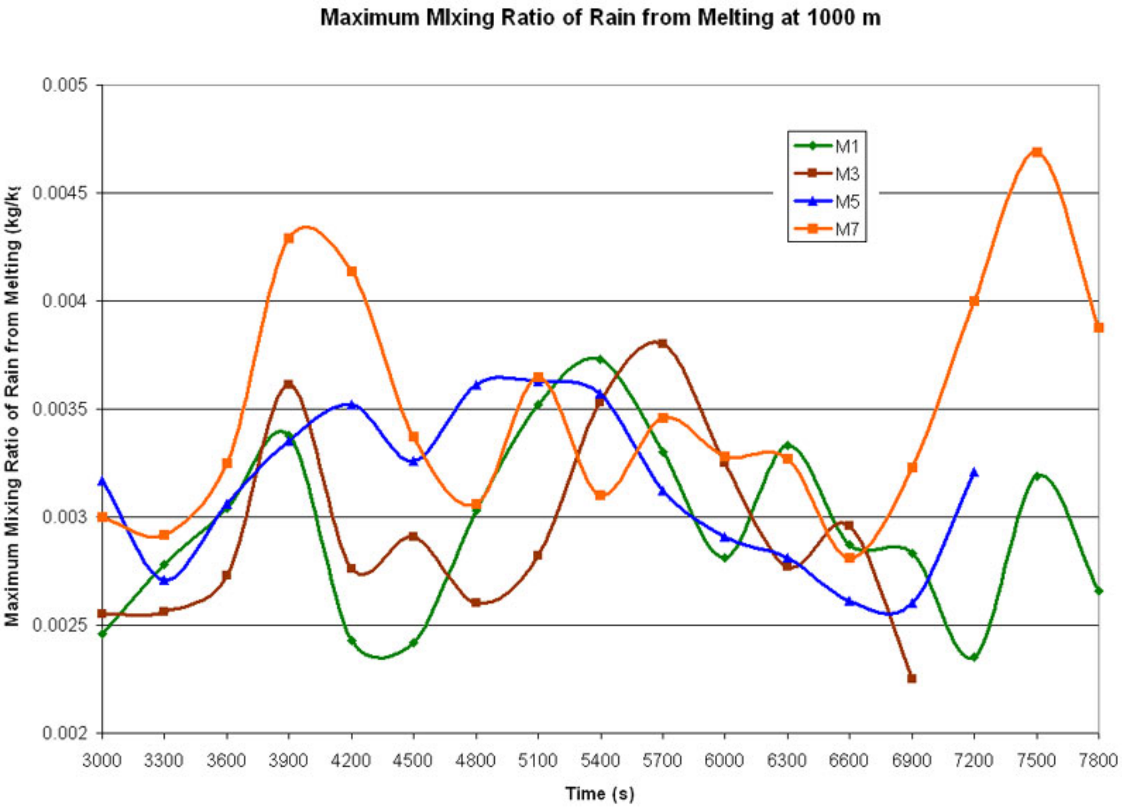

Figure 7.5: Time series of maximum mixing ratio of rain from melting for the four ice-inclusive simulations, with colors and symbols as described in Figure 7.1. Time series run from 3000 s – 7800 s past model initialization. Values of maximum rain from melting mixing ratio are in kg kg^{-1}.

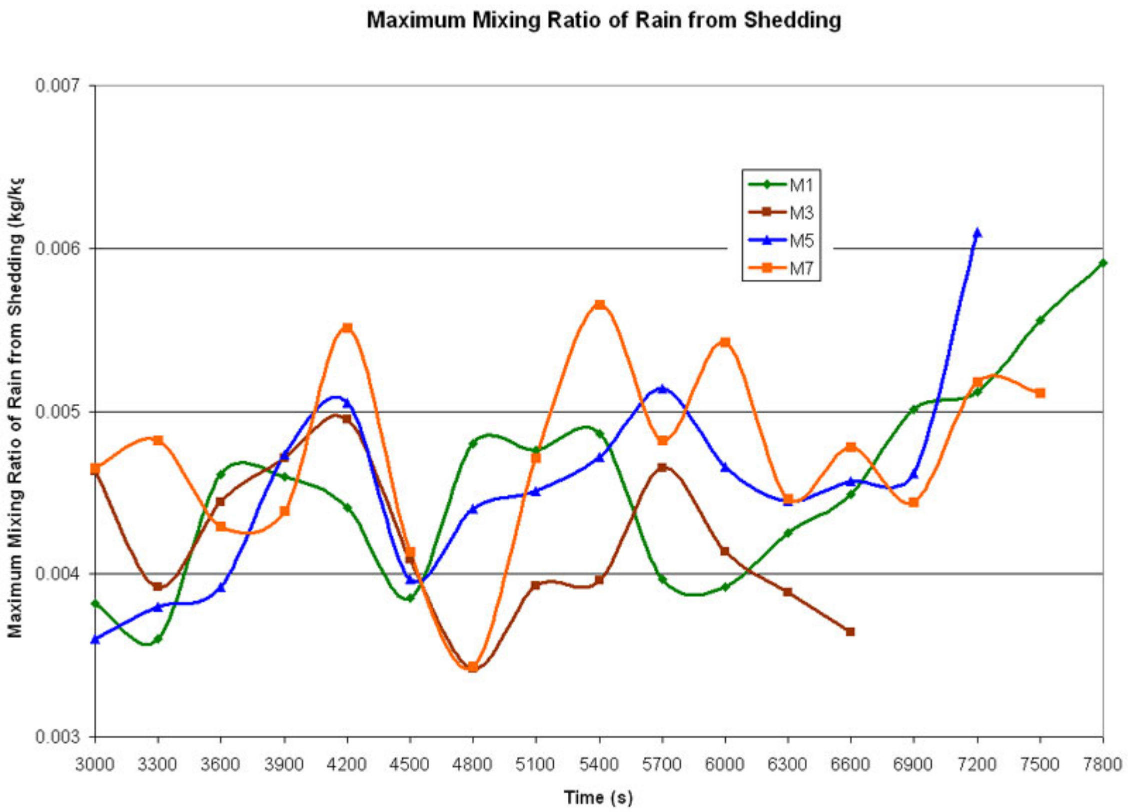

Figure 7.6: Time series of maximum mixing ratio of rain from shedding for the four ice-inclusive simulations, with colors and symbols as described in Figure 7.1. Time series run from 3000 s – 7800 s past model initialization. Values of maximum rain from shedding mixing ratio are in kg kg^{-1}.

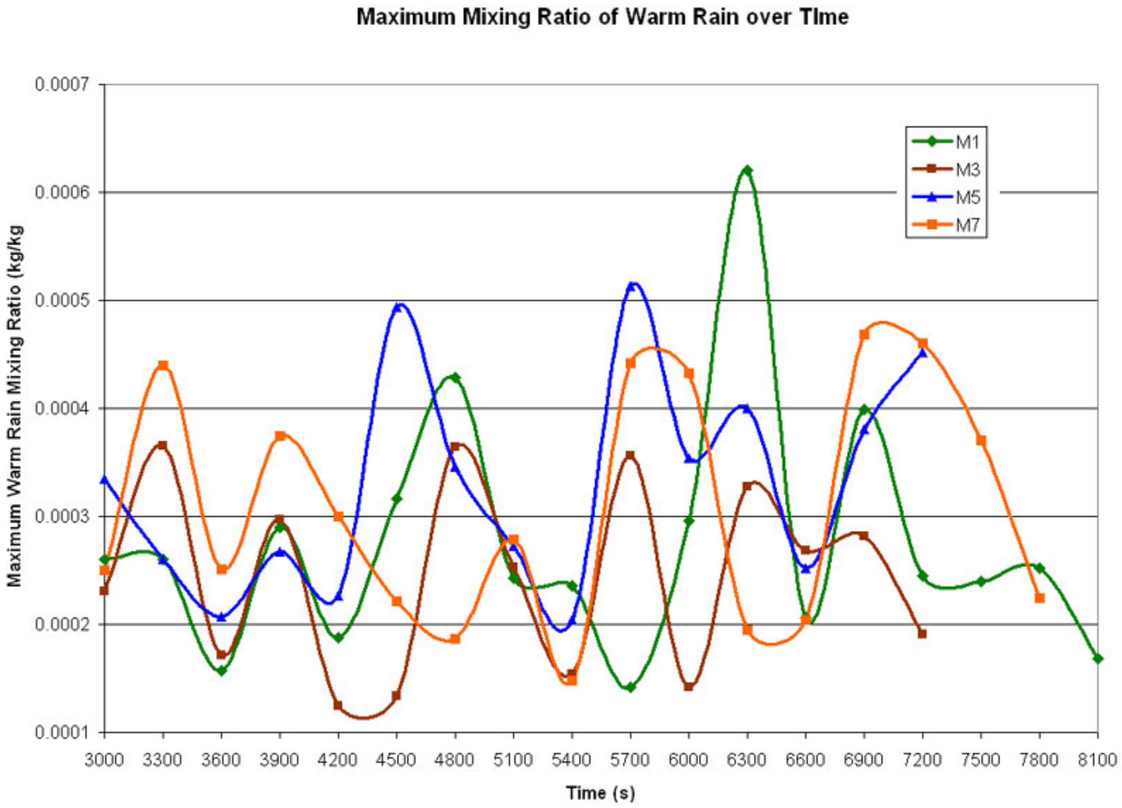

Figure 7.7: Time series of maximum mixing ratio of warm rain for the four ice-inclusive simulations, with colors and symbols as described in Figure 7.1. Time series run from 3000 s – 8100 s past model initialization. Values of maximum warm rain mixing ratio are in kg kg^{-1}.

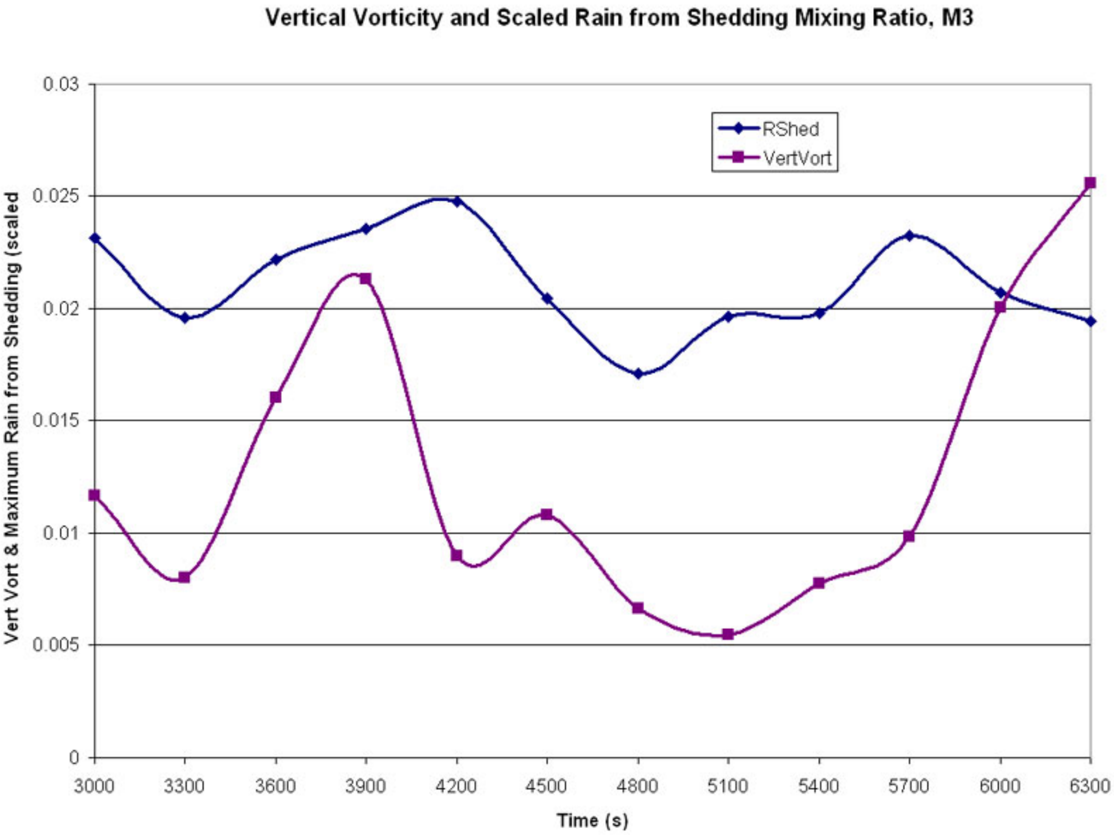

Figure 7.8: Time series of maximum vertical vorticity (units s^{-1}) at the lowest model level (75 m) for simulation 3 (significant drying at midlevels) and scaled rain from shedding at 1000 m. Vertical vorticity is denoted as purple squares, and rain from shedding is denoted as blue diamonds. Time runs from 3000 s to 6300 s past model initialization.

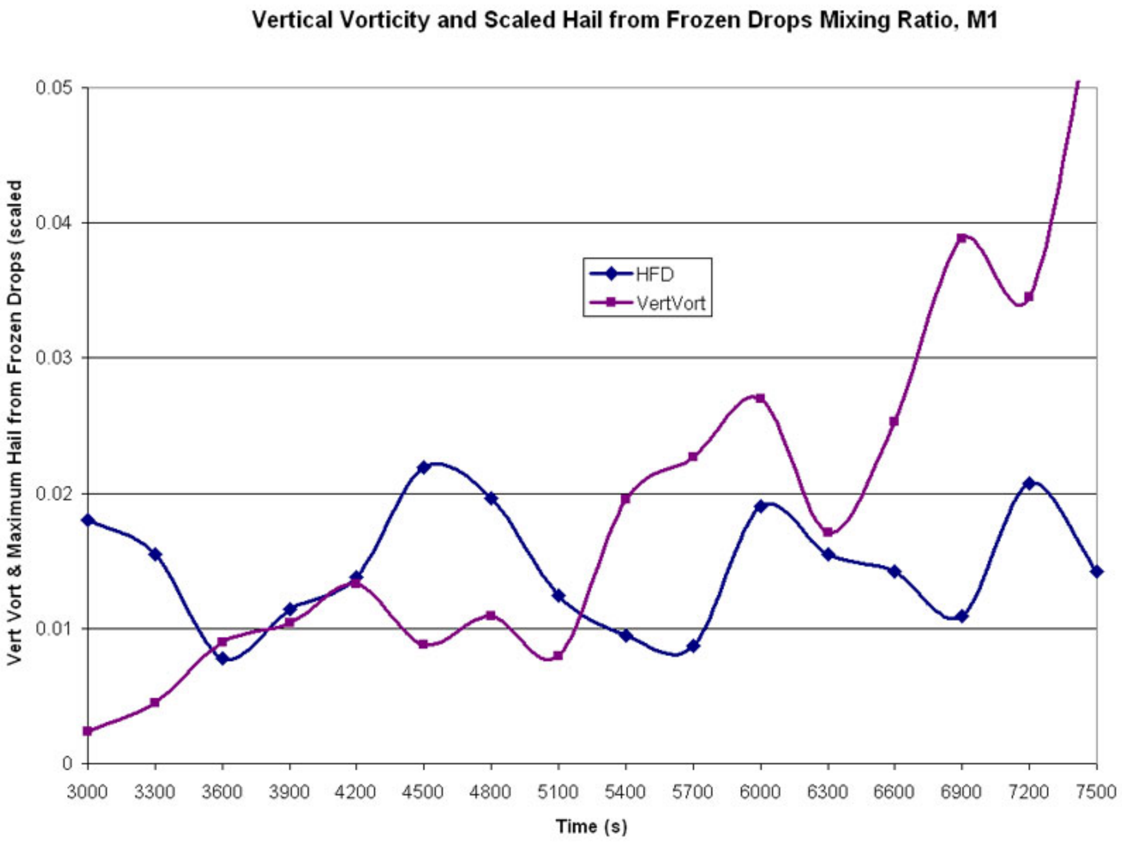

Figure 7.9: Time series of maximum vertical vorticity (units s^{-1}) at the lowest model level (75 m) for simulation 1 (moderate drying at midlevels) and scaled hail from frozen drops at 1000 m. Vertical vorticity is denoted as purple squares, and hail from frozen drops is denoted as blue diamonds. Time runs from 3000 s to 7500 s past model initialization.

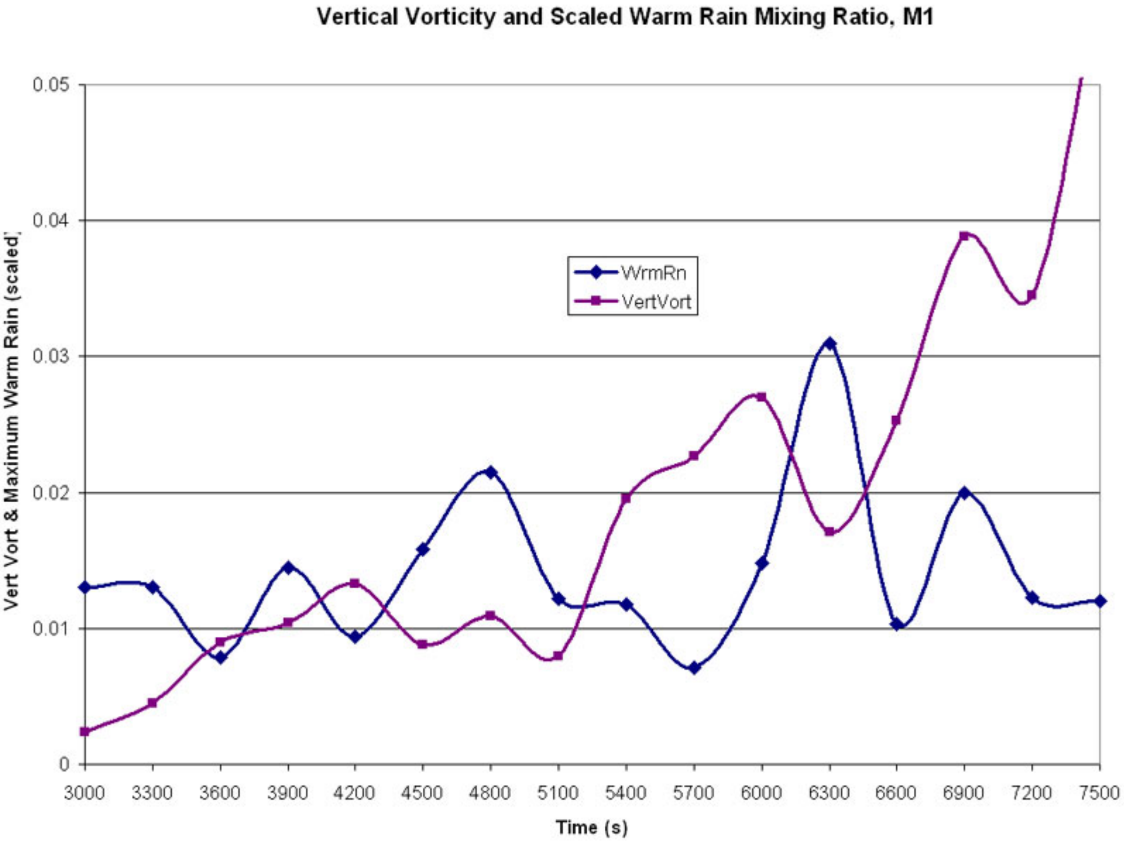

Figure 7.10: Time series of maximum vertical vorticity (units s^{-1}) at the lowest model level (75 m) for simulation 1 (moderate drying at midlevels) and scaled warm rain at 1000 m. Vertical vorticity is denoted as purple squares, and warm rain is denoted as blue diamonds. Time runs from 3000 s to 7500 s past model initialization.

8. Key Conclusions

Numerous useful conclusions can be drawn from this research. To a large extent, much of the microphysical work presented herein represents new ground in understanding supercells. The next significant advance in supercell understanding may well be learning about their microphysics and learning to what extent hydrometeor distributions and dynamical effects control storm evolution. This work has been an attempt to get started along these lines. Below, the primary conclusions of this work will be presented, along with their potential importance and weaknesses.

A. The SAM produced similar cycling behavior as seen in a prior study with liquid-only microphysics, but ice-inclusive microphysics produced a very different parameter space dominated by non-occluding cyclic storms. Non-occluding storms were favored because of weaker RFD westerly surges, and non-cyclic storms were not seen.

Repercussions: Obtaining similar results to past work lends credence to these results. Very different results with liquid vs. ice microphysics suggests modeled storms are very sensitive to microphysics; the modeling community should be very careful to draw conclusions about supercell evolution, since we do not yet have a strong understanding of microphysical processes in supercells and behavior of modeled storms appears very sensitive to choice of microphysics. Caution should be especially great with liquid-only simulated storms, since these are known to produce cold pools which are too strong. Cold pool intensity was seen to significantly affect mesocyclone evolution, so conclusions drawn from liquid-only simulations may be invalid.

Weaknesses: This choice of CAPE was not equivalent to that used in the original study of Adlerman and Droegemeier. A few storms showed different mesocyclone behavior compared to the original study, and these differences were fewer when a more comparable CAPE was chosen. To get the most comparable result, however, the input sounding should be identical to that used in the original study.

B. Liquid-only microphysics tended to produce storms that became linear, while ice-inclusive microphysics tended to produce more persistent supercells. This difference is attributed to greater cold pool strength in liquid-only storms.

Repercussions: Models using liquid-only microphysics may tend to overproduce storms with a linear tendency and produce too few storms which remain as distinct supercells. Cold pool behavior and dangers produced by these two modes of convection are quite different, so an incorrect forecast of mode may initially cause the primary severe weather threat to be stated incorrectly.

Weaknesses: A useful step would be to compare simulated storms with reality for as many of these wind profiles as possible, which is difficult given the rarity of relatively idealized wind profiles in the atmosphere. Such a comparison with real storms has not been made. Thus, although it is known that cold pools are too strong when using liquid-only microphysics, it is difficult to say for sure that the ice-inclusive storms truly behave more realistically.

C. Liquid-only storms contained an average cross-RFD theta gradient twice as strong as in the ice-inclusive simulations. This produced stronger RFD westerly surges, greater upward motion in updrafts, and a tendency toward linearity.

Repercussions: Significant repercussions exist when the cold pool of a simulated storm is too strong. The resulting stronger RFD surges were seen to erroneously increase the chance of mesocyclone occlusion, increase updraft intensity with implications on hydrometeor production and distribution, and ultimately cause supercells to “gust out” too soon. Evolution of the storm as a whole is surprisingly dependent on cold pool strength, so getting the cold pool strength correct is vital for useful simulations.

Weaknesses: Again, good comparisons have not been made to real storms. Many real supercells, however, are observed to remain distinct for many hours, an event which occurred infrequently with liquid-only microphysics.

D. Ice-inclusive storms seemed better-able to utilize increasing environmental shear in processes producing and maintaining near- surface vortices, and were able to produce stronger near-surface vortices than their liquid-only counterparts as shear increased. This was attributed to the typically better-defined and more persistent nature of the mesocyclone in ice-inclusive simulations.

Repercussions: Ice-inclusive simulations handled the near-surface vorticity field much differently than their liquid-only counterparts. Most importantly, under strong environmental shear, ice-inclusive storms still seem able to produce strong near-surface vortices, while liquid-only storms are not as efficient. Real storms are observed to often produce strong vortices under extreme shear. This difference again relates back to cold pool strength, and highlights the necessity of getting cold pool strength correct.

Weaknesses: The parameter space examined to reach this conclusion was woefully inadequate. Only a subset of idealized wind profiles were examined, and these only with one choice of CAPE. Infinitely more factors can vary simultaneously in the real atmosphere, so the results presented here may not remain true if other environmental factors were varied, or if a different subset of wind profiles was chosen.

E. More hail wrapped around the west side of the mesocyclone as hodograph curvature increased, allowing melting of hail to more readily influence the RFD. Bursts of hailfall in this region may aid in the development of RFD westerly surges. Greater hodograph curvature also allows more seeding in the updraft region, producing greater overall quantities of frozen particles.

Repercussions: Shape of the wind profile may produce differing storm evolution partially via changes in the spatial distributions of hydrometeors. Hodograph curvature likely partially determines where hail ends up in a storm, which in turn may influence which downdraft is cooled most by melting. Hodograph curvature also seems to affect the quantity of smaller ice particles produced (graupel, frozen drops) as seeding increases.

Weaknesses: An actual seeding process has not been identified in the model, just inferred from the final particle distributions. Though the altered distributions of hail seem to match observations of real storms, observations at the 1000-m level (where the model was examined) have not yet been inferred. This should become possible with polarimetric radar.

F. Smaller ice-phase particles (graupel and frozen drops), for the wind profiles tested, typically fell out relatively far from the updraft region and were weakly-correlated at best with characteristics of mesocyclone evolution. They may be more influential in determining characteristics of the FFD outflow and cross-FFD theta gradient, which still has significant effects on the storm's lifecycle.

Repercussions: Large ice particles may affect RFD evolution most directly, while small ice particles, being transported farther from the updraft when the hodograph is not significantly curved, may mostly affect FFD strength. Both effects, however, are of vital importance to storm evolution and maintenance. Thus, it is important to represent both large and small ice particles when simulating supercell storms.

Weaknesses: This is another finding which will be virtually impossible to test, short of a significant aircraft measuring campaign. Polarimetric radar observations should be able to assess its plausibility. Ultimately, the exact role of cross-FFD baroclinicity in storm evolution is only somewhat understood, so it may be a long time before the real role of small ice particles in supercell storms is understood.

G. Rain from shedding accounted for about twice as much of the total rain water content compared to rain from melting. Warm rain accounted for much less of the total water content but was extremely variable, and was always located on the southwest and west sides of the echo appendage.

Repercussions: The variability, typical location, and unique DSD of warm rain suggest it may be especially likely to play a role in determining RFD characteristics. Modelers and forecasters should think more deeply about the possible role of different types of rain in controlling supercell evolution.

Weaknesses: So little warm rain often exists relative to other types of rain that this effect may often be inconsequential. Also, it would be very difficult to assess quantity and distribution of the different types of rain in real storms, especially in real time, with the possible exception of warm rain.

H. Warm rain content decreases as hodograph curvature increases due to increased updraft seeding. A moderate amount of shear appears conducive for warm rain, as too little shear leads to unfavorable seeding and too much shear may introduce ice particles from upshear storms. Warm rain is thus favored in moderately- to strongly-sheared environments containing straight hodograph segments, but this effect strongly depends on surrounding convection.

Repercussions: Given the wind profile for a particular day, a forecaster may be able to estimate potential for warm rain production. Once supercells developed, the forecaster could then look for a warm rain signature in polarimetric radar data. Given a preferred type of supercell behavior for the particular day, the forecaster could then anticipate behavioral differences in storms with greater warm rain content.

Weaknesses: This relationship was not universal across the parameter space, and there are likely other factors contributing to warm rain quantity and spatial distribution. Also, just because warm rain is present does not necessarily mean it will have a significant effect on the developing RFD. Quantifying this effect, especially in real time, would be a great challenge given current technology and visualization methods.

I. Warm rain, dominated by small drops, should evaporate more quickly. Storms with higher amounts of warm rain were found to have colder and stronger RFD westerly surges. Greater mixing ratio of hail from frozen drops was also associated with stronger RFD westerly surges, likely aided by melting and sublimation. Stronger RFD westerly surges were observed to produce stronger near-surface vortices to their north, and to increase the likelihood of mesocyclone occlusion.

Repercussions: Bursts of hailfall and warm rain, readily inferred from polarimetric variables, may be used to anticipate storm behavior in the next 5 – 15 min via effects on the RFD. These signatures could potentially be used in real time.

Weaknesses: There is a lack of comparisons to real storms, especially with regard to warm rain. Signatures are not universal across the parameter space and could be expected to be less consistent in the real atmosphere, where many additional factors simultaneously affect the storm.

J. Absolute maximum vertical vorticity in a simulated storm was most closely associated with maximum mixing ratios of hail, likely because melting and sublimation contribute to the intensity of the RFD westerly surge. The sum of maximum vorticity values across a simulation, however, was most related to warm rain content—more warm rain seemed conducive for a storm to consistently produce a strong RFD westerly surge, maintaining higher values of vertical vorticity near the surface.

Repercussions: Observations of significant hailfall in a cyclic storm might lead a forecaster to be concerned about the potential for damaging rotation or RFD winds near the surface. If large quantities of warm rain were inferred or measured, concern may be reasonable that a storm may maintain strong vorticity near the surface for a longer time.

Weaknesses: This is not, at least given current technology, a very operationally-helpful result. Also, since it is based on maximum hydrometeor mixing ratios and maximum near-surface vertical vorticity only, it does not account for volumetrically-integrated sums of these quantities. The two are closely related, but an exact relationship is unknown. Gathering quantities such as mixing ratios and actual vertical vorticity values in real-time may also, for now, be virtually impossible. A gap still needs to be bridged between research and operational application.

K. The role of microphysics seemed most pronounced when the wind shear was not strong. Under stronger shear, dynamical effects would likely dominate, while with weaker shear microphysical effects may be able to have significant influence.

Repercussions: Forecasters can cautiously downplay the effects of microphysics on strongly-sheared days, but should be much more aware of possible microphysical effects on days with weaker shear. This would allow the forecaster to focus on the most important contributions to storm evolution and vorticity concentration for a given day.

Weaknesses: Statements like this are always dangerous, because there are always exceptions. Especially given the very thermodynamically-limited parameter space of this study (e.g. one choice of CAPE), it is unwise to make such a general statement. For instance, on 10 May 2010, a day with extreme dynamic forcing, polarimetric evidence showed warm rain possibly having an important effect on RFD evolution in some storms.

L. The depth and magnitude of drying in a supercell environment can significantly affect the quantity of hydrometeors present, especially graupel and frozen drops. Of the rain variables, warm rain was most sensitive to drying, likely because it tends to have the smallest median drop diameter. Average near-surface vertical vorticity also varied significantly when a deep layer was dried substantially.

Repercussions: Microphysics are sensitive to the vertical moisture profile, as expected. The most sensitive variables were ice-phase, highlighting the need for ice microphysics, and warm rain, which has not been extensively studied in past work. Changes to a supercell’s environment, for example by a storm moving into a drier or moister column, may have important microphysical effects, which in turn may change the storm’s vorticity evolution.

Weaknesses: Only four changes were made to the moisture profile, along with the original moist profile. Thus, very few simulations were used to obtain these results. Also, in the real atmosphere, very rarely are environmental changes so idealized.

M. When midlevels were dried, liquid-only storms produced significant vertical vorticity maxima more quickly than their ice-inclusive counterparts. When a deep layer was dried, however, the ice-inclusive simulations produced higher vertical vorticity values earlier near the surface than the liquid-only storms. Vorticity evolution was dissimilar between ice-inclusive and liquid-only storms. This is attributed to the excessive cold *pool strength in liquid-only storms, and the longer time required for liquid-only storms to develop strong mesocyclones under deep-layer drying.*

Repercussions: Ice-inclusive vs. liquid-only microphysics produce significantly different solutions in terms of the vertical vorticity field. In future modeling, it is imperative to make sure vorticity is being produced and sustained for physically-consistent reasons.

Weaknesses: Again, few simulations were used. Other factors besides microphysics undoubtedly contribute to the differences between storms.

N. When only midlevels were dried, storms produced a significant low-level vorticity maximum much earlier, and typically went on to produce a second, larger maximum toward the end of each simulation. When a deep layer was dried, this initial maximum was reduced, though the secondary maximum was as large.

Repercussions: In tornado families, the relative strength of each tornado may be at least somewhat related to the moisture profile. In moister environments, storms may be able to produce significant concentrations of vorticity earlier in their lives, followed by successive even larger vortices. Under a dry environment, forecasters may see greater signs of mesocyclone maturity before significant vortices are produced, but this will not always be true.

Weaknesses: Again, such guidelines are dangerous because there are exceptions—though tornadoes follow from a predictable sequence of events, nowcasters need to be situationally aware rather than relying on guidelines. Also, mesocyclone maturity may be very difficult to ascertain—for example, on 10 May 2010, the lack of hydrometeors in the updraft of the Norman storm hid its maturity until after the first significant tornado was ongoing. The length of time over which these simulations were run also precludes a detailed analysis of a full supercell lifetime, which would be useful to assess how realistic storm evolution is in the model.

O. Mesocyclones with a dried profile substantially differed from those with the original, moist profile, even exhibiting different modes of mesocyclone cycling. Differences were greatest in ice-inclusive simulations, an expected result since cold pool strength is more sensitive to microphysics in these simulations, which in turn is sensitive to the moisture variations. Column moisture content and distribution seem to provide a significant control on the evolution of the low-level vertical vorticity field, likely via differences in timing of mesocyclone maturity, microphysical evolution, and the degree of evaporative cooling.

Repercussions: A mesocyclone may begin to exhibit different behavior as the parent storm moves into an area with different moisture characteristics. This may be a symptom of microphysical changes leading to RFD surges of altered strength and timing. Forecasters may anticipate changing storm behavior if the storm is moving into a region where the moisture characteristics are known to be different.

Weaknesses: This conclusion seems obvious, though a clear reason for the specific mesocyclone changes was not found in this small sample of storms. Much more research would be needed, including analyses of storms which moved between distinct environments, to say whether the findings here have any operational significance.

P. Occluding cyclic mesocyclone behavior may be favored in storms with high graupel content and low content of warm rain and rain from shedding.

Repercussions: Given polarimetric signatures, it should be possible to determine relative quantities of graupel and warm rain (though not operationally, at least not yet). With this knowledge, it may be possible to anticipate mesocyclone behavior, and thus to anticipate the most likely track of the most dangerous region of a supercell.

Weaknesses: This result came from a small sample, so caution is required in broader application. Also, for now, operational application is very difficult at best and would require advanced training in polarimetric interpretation and application. Also, a physical reason for the association between low warm rain content and occluding cyclic behavior was not found, and seems contradictory.

Q. Bursts of hail from frozen drops were, in several simulations, followed 5 – 10 min later by significant increases in near-surface vertical vorticity. This pattern was most consistent when only midlevels were dried, perhaps because in a moister environment, melting of hail is a more important source of cooling relative to evaporation of liquid.

Repercussions: In moister environments, bursts of hailfall near the storm core or wrapping around the west side of the mesocyclone may be helpful in anticipating increases in low-level vertical vorticity, as seen in several observational studies.

Weaknesses: Few simulations were used to reach this conclusion. The validity of such a relationship would likely differ depending on the storm's level of microphysical maturity. This relationship would be less robust in drier environments, and would likely vary between days.

R. In several simulations, bursts of warm rain preceded by 5 – 10 min increases in near-surface vertical vorticity. The strength of this association varied significantly between storms, however, and is most likely to be present in very dry environments when the warm rain occurs in a location favorable for affecting the developing RFD westerly surge.

Repercussions: In drier environments, bursts of warm rain may be helpful in anticipating increases in low-level vertical vorticity. The polarimetric warm rain signature could possibly be used operationally.

Weaknesses: As above in (Q). This relationship appears to be less robust in moist environments when evaporative cooling is less important, and may be impossible to use unless supercells are relatively isolated.

References

Adlerman, E. J., K. K. Droegemeier, and R. P. Davies-Jones, 1999: A numerical simulation of cyclic mesocyclogenesis. *J. Atmos. Sci.*, **56**, 2045 – 2069.

Adlerman, E. J., and K. K. Droegemeier, 2002: The sensitivity of numerically simulated cyclic mesocyclogenesis to variations in model physical and computational parameters. *Mon. Wea. Rev.*, **130**, 2671 – 2691.

Adlerman, E. J., and K. K. Droegemeier, 2005: The dependence of numerically simulated mesocyclogenesis upon environmental vertical wind shear. *Mon. Wea. Rev.*, **133**, 3595 – 3623.

Bluestein, H. B., and C. R. Parks, 1983: A synoptic and photographic climatology of low-precipitation severe thunderstorms in the Southern Plains. *Mon. Wea. Rev.*, **111**, 2034 – 2046.

Brandes, E. A., J. Vivekanandan, J. D. Tuttle, and C. J. Kessinger, 1995: A study of thunderstorm microphysics with multiparameter radar and aircraft observations. *Mon. Wea. Rev.*, **123**, 3129 – 3143.

Bringi, V. N., D. A. Burrows, and S. M. Menon, 1991: Multiparameter radar and aircraft study of raindrop spectral evolution in warm-based clouds. *J. Appl. Meteor.*, **30**, 853 – 880.

Brooks, H. E., and R. B. Wilhelmson, 1993: Hodograph curvature and updraft intensity in numerically modeled supercells. *J. Atmos. Sci.*, **50**, 1824 – 1833.

Brooks, H. E., C. A. Doswell, and R. B. Wilhelmson, 1994: The role of midtropospheric winds in the evolution and maintenance of low-level mesocyclones. *Mon. Wea. Rev.*, **122**, 126 – 136.

Browning, Keith A., 1965a: Some inferences about the updraft within a severe local storm. *J. Atmos. Sci.*, **22**, 669 – 677.

Browning, Keith A., 1965b: The evolution of tornadic storms. *J. Atmos. Sci.*, **22**, 664-668.

Bunkers, M. J., J. S. Johnson, L. J. Czepyha, J. M. Grzywacz, B. A. Klimowski, and M. R. Hjelmfelt, 2006: An observational examination of long-lived supercells. Part II: environmental conditions and forecasting. *Wea. Forecasting*, **21**, 689 – 714.

Conway, J. W., and D. S. Zrnić, 1993: A study of embryo production and hail growth using dual-Doppler and multiparameter radars. *Mon. Wea. Rev.*, **121**, 2511 – 2528.

Doviak, R. J., V. N. Bringi, A. V. Ryzhkov, A. Zahari, and D.S. Zrnić, 2002: Considerations for polarimetric upgrades to operational WSR-88D radars. *J. Atmos. Oceanic Techno.*, **17**, 257 – 278.

Dowell, D. C., and H. B. Bluestein, 2002a: The 8 June 1995 McLean, Texas, storm. Part I: Observations of cyclic tornadogenesis. *Mon. Wea. Rev.*, **130**, 2626 – 2648.

Dowell, D. C., and H. B. Bluestein, 2002b: The 8 June 1995 McLean, Texas, storm. Part II: Cyclic tornado formation, maintenance, and dissipation. *Mon. Wea. Rev.*, **130**, 2649 – 2670.

Droegemeier, K. K., S. M. Lazarus, and R. Davies-Jones, 1993: The influence of helicity on numerically simulated convective storms. *Mon. Wea. Rev.*, **121**, 2005 – 2029.

Frame, J., P. Markowski, Y. Richardson, J. Straka, and J. Wurman, 2009: Polarimetric and dual-Doppler radar observations of the Lipscomb County, Texas, supercell thunderstorm on 23 May 2002. *Mon. Wea. Rev.*, **137**, 544 – 561.

Gilmore, M. S., and L. J. Wicker, 1998: The influence of midtropospheric dryness on supercell morphology and evolution. *Mon. Wea. Rev.*, **126**, 943 – 958.

Gilmore, M. S., J. M. Straka, and E. N. Rasmussen, 2004a: Precipitation and evolution sensitivity in simulated deep convective storms: comparisons between liquid-only and simple ice and liquid phase microphysics. *Mon. Wea. Rev.*, **132**, 1897 – 1916.

Gilmore, M. S., J. M. Straka, and E. N. Rasmussen, 2004b: Precipitation uncertainty due to variations in precipitation particle parameters within a simple microphysics scheme. *Mon. Wea. Rev.*, **132**, 2610 – 2627.

Hubbert, J., V. N. Bringi, L. D. Carey and S. Bolen, 1998: CSU-CHILL polarimetric radar measurements from a severe hail storm in eastern Colorado. *J. Appl. Meteor.*, **37**, 749-775.

Johnson, D. E., P. K. Wang, and J. M. Straka, 1993: Numerical simulations of the 2 August 1981 CCOPE supercell storm with and without ice microphysics. *J. Appl. Meteor.*, **32**, 745 – 759.

Johnson, K. W., P. S. Ray, B. C. Johnson, and R. P. Davies-Jones, 1987: Observations related to the rotational dynamics of the 20 May 1977 tornadic storms. *Mon. Wea. Rev.*, **115**, 2463 – 2478.

Kamburova, P. L., and F. H. Ludlam, 1966: Rainfall evaporation in thunderstorm downdraughts. *Quart. J. Roy. Meteor. Soc.*, **92**, 510 – 518.

Kennedy, A., J. M. Straka, and E. N. Rasmussen, 2007: A statistical study of the association of DRCs with supercells and tornadoes. *Wea. Forecasting*, **22**, 1191 – 1199.

Kessler, E., III, 1969: On the Distribution and Continuity of Water Substance in Atmospheric Circulation. *Meteor. Monogr.*, No. 32, Amer. Meteor. Soc., 84 pp.

Klemp, J. B., and R. B. Wilhelmson, 1978: The simulation of three-dimensional convective storm dynamics. *J. Atmos. Sci.*, **35**, 1070 – 1096.

Klemp, J. B., R. B. Wilhelmson, and P. S. Ray, 1981: Observed and numerically simulated structure of a mature supercell thunderstorm. *J. Atmos. Sci.*, **38**, 1558 – 1580.

Knupp, K. R., 1988: Downdrafts within High Plains cumulonimbi. Part II: dynamics and thermodynamics. *J. Atmos. Sci.*, **45**, 3965 – 3982.

Kumjian, M. R., and A. V. Ryzhkov, 2008: Polarimetric signatures in supercell thunderstorms. *J. Appl. Meteor. and Climatology*, **47**, 1940 – 1961.

Loney, M. L., D. S. Zrnić, J. M. Straka, and A. V. Ryzhkov: Enhanced polarimetric radar signatures above the melting level in a supercell storm. *J. Appl. Meteor.*, **41**, 1179-1194.

Markowski, P., J. M. Straka, E. N. Rasmussen, 2002: Direct surface thermodynamic observations within the rear-flank downdrafts of nontornadic and tornadic supercells. *Mon. Wea. Rev.*, **130**, 1692-1721.

McCaul, E. W., and C. Cohen, 2002: The impact on simulated storm structure and intensity of variations in the mixed layer and moist layer depths. *Mon. Wea. Rev.*, **130**, 1722 – 1748.

Moller, A. R., C. A. Doswell III, M. P. Foster, and G. R. Woodall, 1994: The operational recognition of supercell thunderstorm environments and storm structures. *Wea. Forecasting*, **9**, 327 – 347.

Rasmussen, E. N., and D. O. Blanchard, 1998: A baseline climatology of sounding-derived supercell and tornado forecast parameters. *Wea. Forecasting*, **13**, 1148 – 1164.

Rasmussen, E. N., J. M. Straka, M. S. Gilmore, and R. Davies-Jones, 2006: A preliminary survey of rear-flank descending reflectivity cores in supercell storms. *Wea. Forecasting*, **21**, 923 – 938.

Ridout, J. A., 2002: Sensitivity of tropical Pacific convection to dry layers at mid- to upper levels: simulation and parameterization tests. *J. Atmos. Sci.*, **59**, 3362 – 3381.

Ryzhkov, A. V., T. J. Schuur, D. W. Burgess, P. L. Heinselman, S. E. Giangrande, and D. S. Zrnić, 2005: Polarimetric tornado detection. *J. Appl. Meteor.*, **44**, 557 – 570.

Schlesinger, R. E., 1973: A numerical model of deep moist convection: Part I. Comparative experiments for variable ambient moisture and wind shear. *J. Atmos. Sci.*, **30**, 835 – 856.

Shabbott, C. J., and P. M. Markowski, 2006: Surface in situ observations within the outflow of forward-flank downdrafts of supercell thunderstorms. *Mon. Wea. Rev.*, **134**, 1422 – 1441.

Srivastava, R. C., 1985: A simple model of evaporatively driven downdraft: application to microburst downdraft. *J. Atmos. Sci.*, **42**, 1004 – 1023.

Srivastava, R. C., 1987: A model of intense downdrafts driven by the melting and evaporation of precipitation. J. *Atmos. Sci.*, **44**, 1752 – 1774.

Soong, S., and Y. Ogura, 1973: A comparison between axisymmetric and slab-symmetric cumulus cloud models. *J. Atmos. Sci.*, **30**, 879 – 893.

Straka, J. M., and J. R. Anderson, 1993: Numerical simulations of microburst-producing storms: some results from storms observed during COHMEX. *J. Atmos. Sci.*, **50**, 1329 – 1348.

Straka, J. M., D. S. Zrnic, and A. V. Ryzhkov, 2000: Bulk hydrometeor classification and quantification using polarimetric radar data: synthesis of relations. *J. Appl. Meteor.*, **39**, 1341 – 1372.

Straka, J. M., and E. R. Mansell, 2005: A bulk microphysics parameterization with multiple ice precipitation categories. *J. Appl. Meteor.*, **44**, 445 – 466.

Thompson, R. L., R. Edwards, J. A. Hart, K. L. Elmore, and P. Markowski, 2003: Close proximity soundings within supercell environments obtained from the rapid update cycle. *Wea. Forecasting*, **18**, 1243 – 1261.

Van Den Broeke, Matthew S., J. M. Straka, and E. N. Rasmussen, 2008: Polarimetric radar observations at low levels during tornado life cycles in a small sample of classic Southern Plains supercells. *J. Appl. Meteor. and Climatology*, **47**, 1232 – 1247.

van den Heever, S. C., and W. R. Cotton, 2004: The impact of hail size on simulated supercell storms. *J. Atmos. Sci.*, **61**, 1596 – 1609.

Weckwerth, T. M., 2000: The effect of small-scale moisture variability on thunderstorm initiation. *Mon. Wea. Rev.*, **128**, 4017 – 4030.

Weisman, M. L., and J. B. Klemp, 1982: The dependence of numerically simulated convective storms on vertical wind shear and buoyancy. *Mon. Wea. Rev.*, **110**, 504 – 520.

Weisman, M. L., and J. B. Klemp, 1984: The structure and classification of numerically simulated convective storms in directionally varying wind shears. *Mon. Wea. Rev.*, **112**, 2479 – 2498.

Zrnić, D. S., and A. V. Ryzhkov, 1999: Polarimetry for weather surveillance radars. *Bull. Amer. Meteor. Soc.*, **80**, 389 – 406.